Université d'Ottawa · University of Ottawa

Université d'Ottawa · University of Ottawa

FACULTÉ DES ÉTUDES SUPÉRIEURES ET POSTDOCTORALES

FACULTY OF GRADUATE AND POSTDOCTORAL STUDIES

Julie MONDOUX

AUTEUR DE LA THÈSE - AUTHOR OF THESIS

M. A. Sc. (Mechanical Engineering)

GRADE - DEGREE

Department of Mechanical Engineering

FACULTÉ, ÉCOLE, DÉPARTEMENT - FACULTY, SCHOOL, DEPARTMENT

TITRE DE LA THÈSE - TITLE OF THE THESIS

Development of Cold-gas Dynamic Spraying System for Parameter Study of Aluminium Coatings

B. Jobin

DIRECTEUR DE LA THÈSE - THESIS SUPERVISOR

CO-DIRECTEUR DE LA THÈSE - THESIS CO-SUPERVISOR

EXAMINATEURS DE LA THÈSE - THESIS EXAMINERS

X. Huang

H. Naguib

J.-M. De Koninck, Ph.D.

LE DOYEN DE LA FACULTÉ DES ÉTUDES SUPÉRIEURES ET POSTDOCTORALES

DEAN OF THE FACULTY OF GRADUATE AND POSTDOCTORAL STUDIES

Development of a Cold-Gas Dynamic Spraying System for Parameter Study of Aluminium Coatings

By
Julie Mondoux

Thesis submitted to the
Faculty of Graduate and Postdoctoral Studies
in partial fulfillment for the requirements to the degree of

Master's of Applied Sciences

Ottawa-Carleton Institute for Mechanical and Aerospace Engineering

Department of Mechanical Engineering
University of Ottawa

Your file Votre référence
ISBN: 0-494-01554-3
Our file Notre référence
ISBN: 0-494-01554-3

SUMMARY

Component corrosion prevention is a fundamental part of machine design; caustic embrittlement and corrosion fatigue are leading causes of part failure. This can have a detrimental financial impact and cause safety concerns in many industries which perform tasks in various environments, such as the aerospace, automotive, naval or civil industries, for example. The costs associated with corrosion protection and repairs are exorbitant. One method used to reduce the impact of corrosion is through the deposition of a thin aluminium coating. The aluminium coating acts as a sacrificial anode and corrodes while protecting the underlying material. There are numerous processes to deposit aluminium coatings on manufactured components; one of the most recently developed is Cold Gas Dynamic Spraying (CGDS). Further development of the CGDS process will be the focus of this work.

Cold Gas Dynamic Spraying is a thermal spraying process in which a flow of gas is accelerated to a supersonic velocity using a converging-diverging nozzle. Powder feedstock is injected in the nozzle and subsequently accelerated with the gas. Once the two-phase flow impacts a substrate outside the nozzle, the particles adhere if their kinetic energy is high enough. There exists a critical velocity below which very little particle adhesion occurs. There are a number of materials that have been successfully sprayed; mostly ductile metallic materials.

The objectives of this work were to develop a cold gas dynamic spraying set-up which sprayed aluminium powders with different microstructures, mainly conventional and nanocrystalline particles, and to determine which of the powders is most suitable for spraying. The development of the CGDS set-up included the numerical modeling of the supersonic gas flow; this lead to the design of the converging-diverging nozzle. Two sets of experiments were conducted to validate the model and design. The preliminary experiments were conducted using both conventional and nanocrystalline powders and the initial results showed that the nanocrystalline powders had a higher Vickers hardness. The nanocrystalline coatings were denser and adhered more evenly with the substrate. The second set of experimental work was conducted only with conventionally structured particles to determine the influence of three spraying parameters on the performance of the coating. The parameter characterization was done following a k-factorial testing scheme in which the three spraying parameters were varied and a response parameter was measured for all the trials. The stand-off distance, the pressure difference at the injection site and the spraying time were the modified parameters while the Vickers hardness was the selected response parameter. Preliminary conclusions were drawn from the parameter testing. It showed that the most important spraying variable for these experiments was the stand off distance. It also showed that the pressure difference at the inlet was the parameter with the least impact on the hardness of the sample. The micrographs associated with the k-factorial testing were also compared to the ones obtained for the preliminary testing. The porosity in the conventional coatings was higher than in the nanocrystalline coatings, even if there had been improvements made to the experimental set-up.

In this work, an experimental CGDS set-up, capable of successfully spraying conventional and nanocrystalline powders was designed. It was found that nanocrystalline coatings provide a higher hardness, a lower porosity and a more uniform substrate-particle interface than the conventionally structured coatings. The preliminary conclusions drawn were that the most influential spraying parameter was the stand off distance while the least influential was the pressure difference at the injection site.

ACKOWNLEDGEMENTS

I would first like to thank my supervisor, Dr.Bertand Jodoin. We have come a long way since you first brought up the idea of building a cold spray system; it's great to see it finally work! Thank you for the experience, I learned a lot and know that I am better prepared than I can even fathom for whatever I decide to do next.

I also wish to thank the outside contributors: Dr. Leonardo Ajdelsztajn of the University of California at Davis for providing the nanocrystalline powders and performing the coating characterization and the NRC's Industrial Materials Institute in Boucherville for manufacturing the nozzle.

Thanks to all the support staff at the department and the technicians at the machine shop. Many many thanks to Eric and Patrick for helping me with the experiments and for making the initial design even better... I still owe you guys a beer! Thanks to all the other grad students in our group: Stéphanie, Alexandre, Karen and Devin... you made work a lot more fun!

Merci à mes parents, mes frères et mes amis pour leur support et leurs encouragements.

Et finalement, merci à Jason... pour tout...

TABLE OF CONTENT

LIST OF FIGURES

LIST OF TABLES

GLOSSARY

- **Adiabatic Shear Instability:** Phenomenon that occurs when a material undergoes a high level of plastic deformation, strain energy is released as heat by increasing the temperature of the material.
- **Chemical Vapour Deposition:** Formation of a film on a surface from a gaseous substance.
- **Chemisorptional Bond:** Chemical bond involving a substantial re-arrangement of electrons between the feedstock and the substrate.
- **Cold Gas Dynamic Spraying (CGDS):** Thermal spraying process in which particles are injected into a supersonic gas jet and accelerated to elevated velocities before impacting and adhering to a substrate.
- **Compressed Layer:** Layer found at surface of substrate due to the formation of a bow shock.
- **Computational Fluid Dynamics (CFD):** Computer based study of fluid flow based on known parameters.
- **Critical Velocity:** Velocity above which adequate adhesion will occur.
- **Crystalline Structure:** Atom or ion arrangement in space. Defined in terms of the unit cell geometry and the atom positions within the unit cell.
- **Detonation Gun (D-Gun^{TM}) Spraying:** Thermal spraying process.
- **Driving Gas:** For a thermal spraying application, gas in which feedstock particles are injected and which accelerates them.

- **Ductility:** A measure of the ability of a material to undergo deformation before fracture.
- **Electro-plating:** deposition of a metallic coating onto an object by negatively charging the object and immersing it into a solution which contains a salt of the metal to be deposited.
- **Expansion and Compression Wave:** A simple wave or progressive disturbance in the isentropic flow of a compressible fluid, such that the pressure and density of a fluid particle decreases on crossing the wave in the direction of its motion.
- **Feedstock:** Material which will form the coating.
- **Grain:** Individual crystal in a polycrystalline material.
- **Grain Size:** The average grain diameter as determined from a random cross section.
- **Hardness:** Measure of the resistance of a material to deformation by surface indentation or abrasion.
- **High Velocity Oxy-Fuel (HVOF) Spraying:** Thermal spraying process, see Section 2.1.3.
- **Hydroxyapatite:** Ceramic used to coat implants.
- **K-factorial Testing Scheme:** Random testing scheme to determine influence of a parameter on process response.
- **Lattice Parameter:** The combination of unit cell edge lengths and interaxial angles that defines the unit cell geometry.
- **Metal Matrix Composite:** A composite material which has a metal or metal alloy as the matrix phase.
- **Microstructure:** Structural features of a material.

- **Nanocrystalline:** Property of a material with structure at the nanometer (10^{-9} m) scale.
- **Nozzle:** Device responsible for accelerating driving gas in thermal spraying systems.
- **Particle Image Velocimetry:** Characterization method that uses images to calculate flow velocity.
- **Physical Vapour Deposition:** Formation of a film on a surface from a solid substance.
- **Shock Wave:** Abrupt change in flow properties to adapt to disturbance in flow.
- **Solid-state Deformation Process:** Deformation occurring without any phase change.
- **Stagnation Temperature:** Temperature if the flow is decelerated to zero velocity; in this work, also taken as the temperature at the inlet of the nozzle.
- **Substrate:** Base material where feedstock material will adhere to form coating.
- **Thermal Spraying:** Group of processes in which finely divided material are deposited in a molten or semi-molten state on a substrate to form a thick deposit.
- **Two-dimensional Axisymmetrical Model:** For a cylindrical cross-section, the radial profile for the centerline to the outer diameter is assumed to be constant for a 2π revolution around the centerline.
- **Two-phased Flow:** Flow with two distinct phases.

NOMENCLATURE

The following is the nomenclature used in this thesis.

Geometric Variables

α	Diverging angle
γ	Converging angle
A	Area
CS	Control surface
CV	Control volume
d	Diameter
dA	Infinitesimal area
dr	Infinitesimal radius
$d\forall$	Infinitesimal volume
L_{div}	Length of diverging section
$\hat{n}$	Normal unit vector
$\vec{N}$	Normal vector to control surface
z	Height

Fluid, Thermodynamic and CFD Variables

δ	Boundary layer thickness
δ^*	Displacement thickness
ε	Turbulent kinetic energy dissipation rate
ϕ	Dependent variable
γ	Specific heat ratio
Γ	Diffusion coefficient
ρ	Density
$\rho(r)$	Radial density profile
σ_ε	Turbulent Prandtl number for the turbulent kinetic energy dissipation

σ_k	Turbulent Prandtl number for the turbulent kinetic energy
Y_M	Contribution of the fluctuating dilation in compressible turbulence to the overall dissipation rate
a_i	Coefficient
a_p^0	Coefficient due to unsteady nature of flow
c	Speed of sound
C_p	Constant pressure specific heat
C_v	Constant volume specific heat
$C_{i\varepsilon}$	Empirical constants
e	Specific internal energy
F_{ext}	External forces
g	Gravitational acceleration
G_b	Generation of turbulent kinetic energy due to buoyancy
G_k	Generation of turbulent kinetic energy due to the mean velocity gradients
h	Specific enthalpy
k	Turbulent kinetic energy
m	Mass
M	Mach number
P	Pressure
Q	Heat transfer
$\dot{Q}$	Heat transfer rate
R	Gas constant
s	Specific entropy
S	Source term
S	Entropy
$\dot{S}_{gen}$	Entropy generation rate
T	Temperature
u	axial velocity
u(r)	Radial velocity profile

V	Velocity
$\vec{V}$	Overall flow velocity
W	Work

Solid Mechanics Variables

ε	Strain
σ	Stress
d	Diagonal of indentation
E	Elastic Modulus
P	Imposed load
V	Vickers hardness

Subscripts and Superscripts

o	Stagnation conditions
*	Throat of nozzle
a	Property on the centerline
b	Property related to back conditions
CS	Property related to the control surface
CV	Property related to the control volume
e	Property related to the exit of the nozzle
r	Property associated with actual geometry
s	Isentropic process
sys	Property related to the system
x	Property prior to the shock wave
y	Property after the shock wave

1. INTRODUCTION

Engineers play an important role in assuring the safety of the population. As such, their work often involves making minor or major design changes to current technology to improve the reliability and performance of every day tools, and sometimes, at a lower cost. One of the methods used to improve the current technology is to apply a coating. Coatings can be used for many purposes and in many areas. For example, they have been used to repair parts by being applied to areas worn down by wear, to protect against corrosion or to provide specific properties that the core material could not provide at an efficient cost. Coatings are found in a wide range of fields such as the automotive, aerospace, biomedical, and civil, nautical industries.

Component corrosion prevention is a fundamental part of machine design; caustic embrittlement and corrosion fatigue are leading causes of part failure. This can have a detrimental financial impact and cause safety concerns in many industries which perform tasks in various environments, such as the aerospace, automotive, naval or civil industries, for example. The costs associated with corrosion protection and repairs are exorbitant. For example, the civilian aircraft industry in the United States spends $US13 billion per year to prevent and repair corrosion damage [1]. The consumer costs in the automotive industry are approximately $US23.4 billion a year [1]. These costs include the increased manufacturing costs, repairs, maintenance and depreciation due to corrosion. The use of aluminium coatings is one of the many ways used to prevent corrosion. The aluminium coating is used as a sacrificial anode, corroding while the

underlying material is protected from the environment. There are numerous methods by which the aluminium coatings are deposited, such as the various thermal spraying processes, such as plasma spraying, High-Velocity Oxy-Fuel Spraying and detonation gun spraying as well as chemical vapour deposition, physical vapour deposition, electro-plating and electro-less plating, to name a few. Much of the improvement efforts are concentrated in reducing the costs and simplifying the deposition processes. The selected process for this study is cold gas dynamic spraying, an emerging thermal spray process. Cold gas dynamic spraying is a new process which can be easily developed, at relatively low cost, due to the simplicity of the equipment as compared to some of the other processes used in the industry.

The purpose of this study was to develop an experimental set-up to deposit an aluminium coating using CGDS for the purpose of corrosion resistance using both conventional and nanocrystalline aluminium powders. Subsequently, a parameter study to determine the optimal spraying conditions and the influence of specific parameters was performed. Finally, the two coating types were compared to determine if the use of nanocrystalline material is advantageous.

It was hypothesised that nanocrystalline coatings would possess a greater hardness and that they would be sprayed less successfully due to their higher inherent hardness. It was further hypothesized that the most important parameter between the ones selected would be the stand off distance between the nozzle and the substrate. These hypotheses were verified by performing a hardness test on the samples produced using a

k-factorial testing scheme that provided an indication of the most important spraying parameter.

1.1 Thesis Outline

This thesis will describe the step by step development of a cold gas dynamic spraying set-up, from the numerical modeling to the production of aluminium coatings and the optimization of the spraying parameters. In Chapter 2, an outline of the main thermal spraying processes, a description of the cold gas dynamic spraying process as well as a comparison between all the processes is presented. The theory of cold gas dynamic spraying is summarized in Chapter 3. The numerical model used to simulate the process, and design the set-up as well as the important results that lead to the preliminary design, are found in Chapter 4. In Chapter 5, the equipment used in the experimental set-up is described. The experimental results are shown and discussed in Chapter 6. Finally, in Chapter 7, a synopsis of the major results as well as recommendations to improve the experimental set-up and future areas that could be interesting to study, are presented.

2. CURRENT STATE OF THE ART IN THERMAL SPRAYING

In this chapter the major contributions in the development of the Cold Gas Dynamic Spraying (CGDS) process as well as various aspects of spraying and depositing conventional and nanocrystalline materials are reviewed. To provide the reader with a comprehensive understanding of the background information related with the CGDS process, this chapter is subdivided into the following sections: thermal spraying, cold gas dynamic spraying, and aluminium coatings and characterization. A comparison between all the processes focusing on the advantages and disadvantages of all the thermal spraying processes described in the chapter will be included at the end of the chapter to provide a summary of the current state of the art in thermal spraying.

2.1 Thermal Spraying

Thermally sprayed coatings are produced by processes in which finely divided metallic or nonmetallic materials are deposited in a molten or semimolten condition on a substrate to form a deposit [2]. The process of applying a thermally sprayed coating involves the heating of feedstock, from either a powder, rod or wire form, to a molten or semi-molten state. The feedstock is then accelerated to a process-dependent velocity, before it impacts a substrate, upon which it will adhere and solidify, forming a coating.

The main advantages of thermal spraying over other coating processes such as chemical vapour deposition and electro-plating are the low-to-moderate equipment and operating costs for a majority of thermal spraying set-ups, the good mechanical bonding at the substrate and feedstock interface, the thick coatings produced as well as the variety

of materials that can be deposited [3]. The following section will examine some common applications of thermally sprayed coatings along with some of the most common processes, namely, plasma spraying, high-velocity oxy-fuel spraying (HVOF) and detonation gun spraying.

2.1.1 Thermally sprayed coating applications

Industrial applications for thermal spraying processes are numerous. The produced coatings are used for biomedical, automotive, and aerospace applications to name a few.

One example of a biomedical application is the plasma spraying of hydroxyapatite (HA) on implants, such as dental implants or hip implants. HA has been shown to interact positively with the human body by actively joining bone tissue and promoting bone re-growth [4]. This is due to the release of calcium and phosphate by the HA coating which are the ions from which the mineral phase of the bone are built. The ions can re-precipitate as natural carbonated apatite onto the bone, preventing any adverse reaction by the human body [5].

There are a number of automotive applications. One early application of thermal spraying in the automotive industry was in 1992 when an alternative to laser-cladding was used to produce integral valve seat regions in aluminium engine heads [6]. Currently, there are many efforts to use thermal spraying technologies for cylinder-bore coating since it is a high temperature and high wear part in the engine [7].

Coatings are also used in the aerospace industry to coat exhaust valves and seats with cobalt alloys [8], which are exposed to very high temperatures, and to produce oil free bearings in turbochargers [9]. Ceramic thermal barrier coatings are also used in the hot sections in the engine such as the exhaust nozzle [10]. Thermal barrier coatings provide a layer of heat resistance material, such as ceramic, to isolate other important components.

All the different industrial applications make thermally sprayed coatings very versatile and the sales associated with thermal spray are increasing at a rate of nearly 10% per year since 1990 [11]. The more mainstream processes, which will be discussed in the following sections, are plasma, high-velocity oxy-fuel and detonation gun spraying.

2.1.2 Plasma Spraying Process

The plasma spraying process, illustrated in Figure 2-1, is the most versatile of the processes and is used for the widest range of applications [12]. Plasma spraying uses a plasma gas, typically argon in combination with helium [12], generated by different energy sources such as microwaves, electromagnetic RF or induction-coupled fields and either alternate or direct current arcs [3]. The gas is accelerated using a nozzle to entrain the powder injected outside the nozzle. The powder is melted due to the high temperature of the plasma (between 10 000 and > 25 000K [3]). As the molten feedstock impinges on the substrate, it adheres and re-solidifies, thus forming a coating.

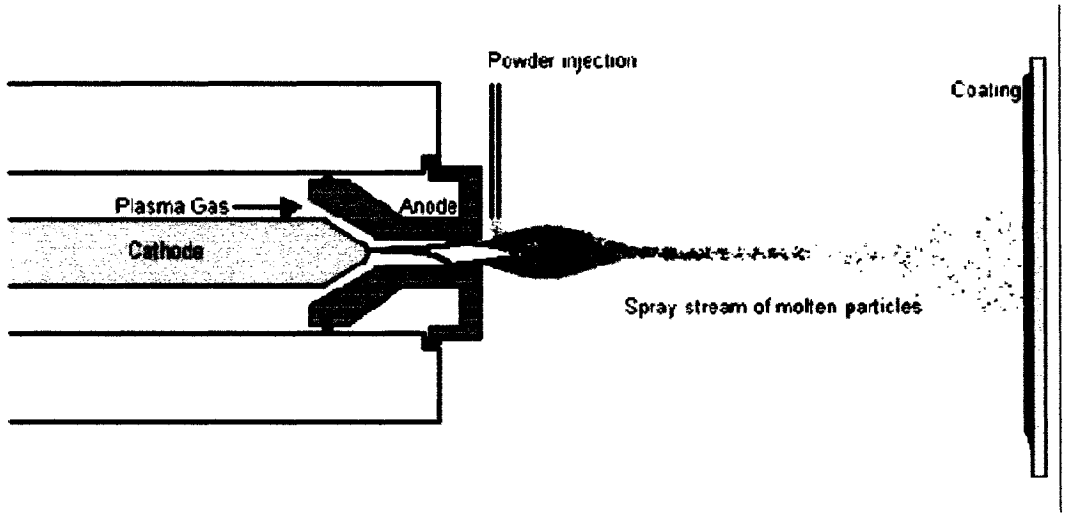

Figure 2-1: Plasma spraying set-up [12]

Plasma spraying is a versatile process since it can use metallic, ceramic and composite material feedstock. It has widespread applications in aerospace, automotive and biomedical industries. Significant disadvantages of plasma spraying are the possible non-uniform melting of the particles caused by the different trajectories the particles will have inside the plasma jet as well as the elevated equipment cost and the complexity of the process [12].

2.1.3 High-Velocity Oxy-Fuel Spraying

Plasma spray is the precursor to High-Velocity Oxy-Fuel Spraying (HVOF). The process, illustrated in Figure 2-2, was first developed in 1958 by Union Carbide [12] (now Praxair) and was available commercially in 1974. Due to the proprietary nature of the process, independent research on this process was not conducted until a few years ago.

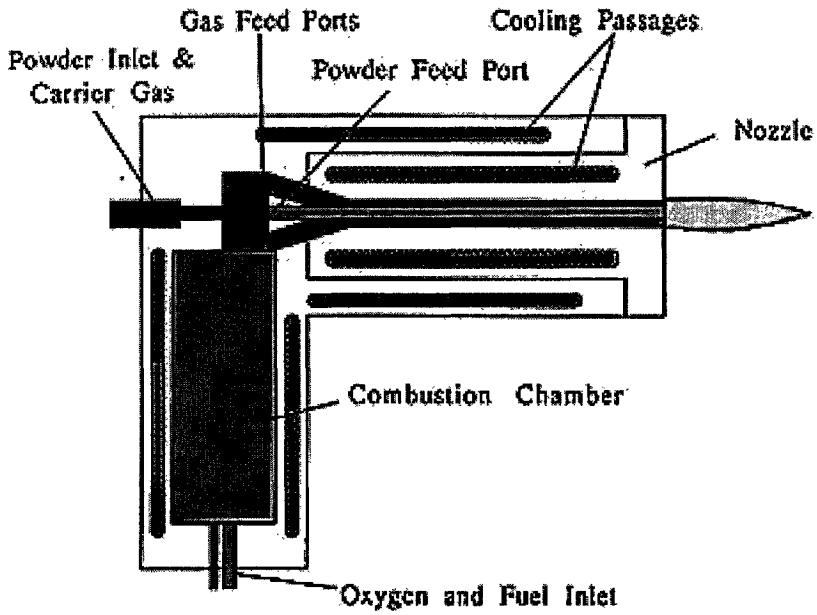

Figure 2-2: HVOF set-up [12]

In the HVOF process [13], liquid fuel such as acetone and oxygen are fed to, and burnt, in a combustion chamber to produce a high pressure and high temperature gas jet. Subsequently, the gas jet is accelerated through a nozzle. The feedstock particles can either be injected in the nozzle simultaneously with the fuel-oxygen mixture or at the exit of the nozzle once the fuel-oxygen mixture has been accelerated. In the high temperature gas jet, the particles will soften or melt prior to impacting the substrate.

The process is currently used in the aerospace industry [14], principally for chrome coating replacement on hydraulic actuators, landing gear, propeller hubs and helicopter dynamic components.

2.1.4 Detonation Gun

The detonation gun process, or D-Gun™, was also developed by Union Carbide. Similar to the HVOF process, the detonation gun process uses confined combustion; however, during this process the fuel is fed into a barrel and spark ignited producing a high velocity jet [15]. The jet entrains the particles that are also fed into the barrel. A schematic of the D-Gun™ set-up is found in Figure 2-3.

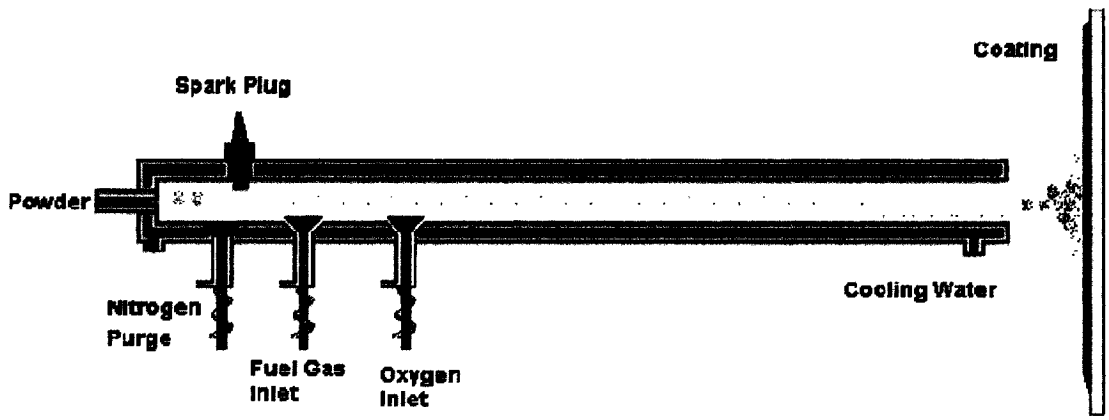

Figure 2-3: Detonation gun schematic [15]

The three processes described previously are commonly used thermal spraying processes. The following section will detail cold gas dynamic spraying, a new and emerging thermal process which combines many characteristics of the processes detailed previously. Subsequently, a detailed comparison between the processes will conclude the chapter.

2.2 Cold Gas Dynamic Spraying

The most recent advance in the area of thermal spraying is cold gas dynamic spraying (CGDS) or cold spray process. In the following section, the published works dealing with the history and process overview of CGDS, the fluid mechanics and materials aspects as well as the bonding mechanism involved in CGDS are reviewed.

2.2.1 History and Process Overview

CGDS was discovered accidentally while studying a completely different phenomenon. In the mid-1980s [16], the group lead by Anatolii Papyrin at the Institute of Theoretical Mechanics of the Siberian Division of the Russian Academy of Science in Norvosibirsk was conducting experiments on the re-entry of high-speed vehicles. They observed that some of the metal tracing particles adhered to the targets and initially believed that the high velocity the particles possessed sufficient kinetic energy to adhere to the substrate during impact. A series of experiments, in which particles were injected in a flow, were performed to verify this hypothesis. The high gas and particle velocity was obtained using a converging-diverging nozzle[1], which accelerated a flow to supersonic velocities. The two-phased flow impacted on a substrate to form a coating. To determine if the deposition of these coatings could be controlled and reproduced, a pilot plant was built to spray steel pipes with aluminium and zinc. The first results were published in 1990 [17]. This first publication reported that coatings were formed of either aluminium, copper, zinc, iron and nickel particles. The particles were injected in a

[1] The converging-diverging nozzle is also known as a De Laval nozzle.

mixture of air and helium at pressures between 0.5 to 2 MPa and accelerated to a nozzle exit velocity of Mach 2.6.

Contrary to their initial hypothesis, Papyrin et al [17] found that there were two possible ways in which particles would adhere to the substrate. They termed the first adhesion process as "non-independent" attachment. This occurs when a single particle does not have the kinetic energy required to adhere independently to the substrate. Rather, it becomes attached following a double impact. The double impact will occur when a particle impacts the substrate and another particle prevents it from rebounding, trapping it on the substrate. The force applied to the first particle by the second one can bond it to the substrate. The second adhesion process, termed the "independent" attachment of particles, occurs when the particle velocity at impact exceeds the velocity required for independent adhesion. In that case the adhesive forces due to the plastic deformation are larger than the elastic rebound repulsive forces, resulting in plastic deformation of both the particle and the substrate, and thus adhesion of the particles to the substrate. The determining factor for the type of adhesion process that will occur is the kinetic energy of the particles. The velocity required for the second adhesion process was defined as the critical velocity. This definition was selected based on the result of plotting the deposition efficiency, which was defined as the ratio between the mass of the powder sprayed and the increase in mass on the substrate as a function of velocity (Figure 2-4). From the figure, it is observed that there exists a material specific minimum velocity that the particles must attain in order for a significant portion of them to adhere to the substrate.

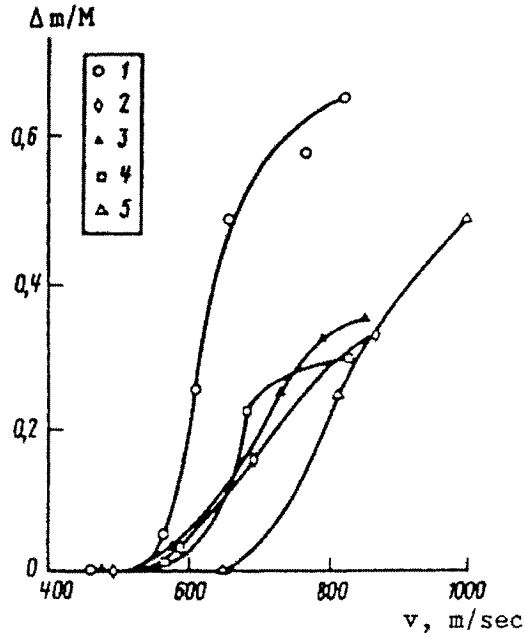

Figure 2-4: Deposition coefficient as a function of velocity for particles with d =10 μm for copper (1), zinc (2), iron (3), nickel (4) and aluminium (5) powders [17]

Following the publication of this first study, research on CGDS was pursued in the United States where the first patent for the process was issued to Alkhimov et al in 1994 [18]. Dykhuizen et al [19] published a paper outlining the gas dynamics principles used in the CGDS process. Their analysis resulted in an optimal design for the CGDS nozzle which accounted for the interactions between the geometric parameters and the material properties of the particles. They concluded that the particle velocity was a function of the gas properties as well as the density and size of the sprayed particles. They also showed that the nozzle length has an effect on the performance while the nozzle shape has none. Finally, they were able to spray a number of different powders for a number of conditions. Similar to the work by Papyrin [18], they plotted the deposition

efficiency as a function of particle velocity (Figure 2-5). Their results also showed the presence of a material-specific critical velocity.

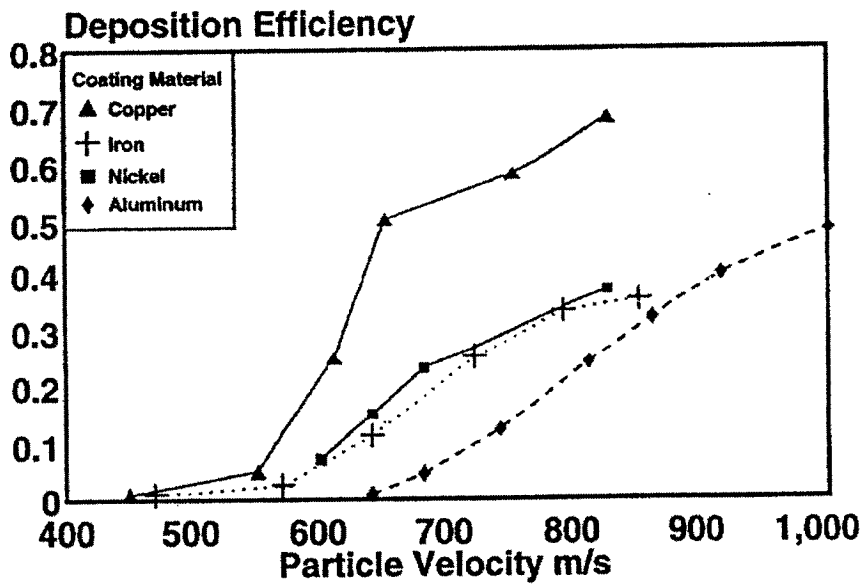

Figure 2-5: Deposition efficiency versus particle velocity [19]

Subsequent work was performed to optimize the deposition efficiency using copper particles [20]. The deposition efficiency was improved up to 95% as shown in Figure 2-6.

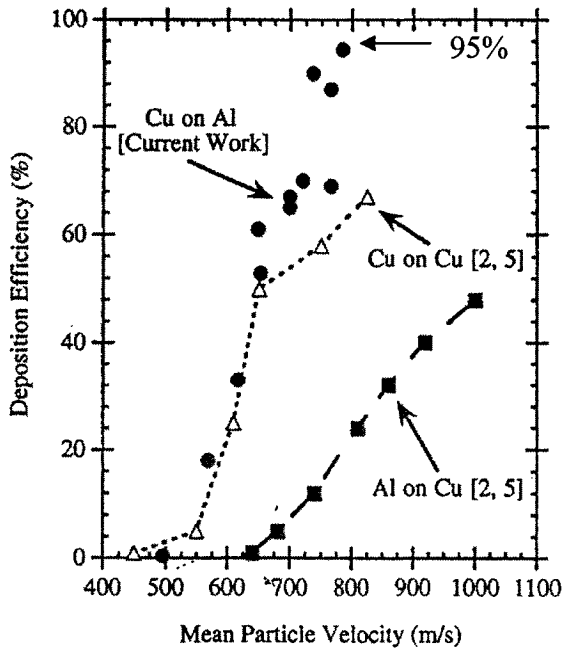

Figure 2-6: Deposition efficiency versus mean particle velocity (x=0, y=0, z=25mm in Cartesian coordinate system) for 19 μm mean diameter copper powder, helium driving gas, varying pressure and temperature [20]

The effect of the angle between the impacting supersonic jet and the substrate, termed the impact angle was also studied. It was found that the optimal impact angle was zero (Figure 2-7). Therefore, the nozzle exit must be perpendicular to the substrate to provide the best adhesion. This configuration is optimal since it results in the highest perpendicular momentum.

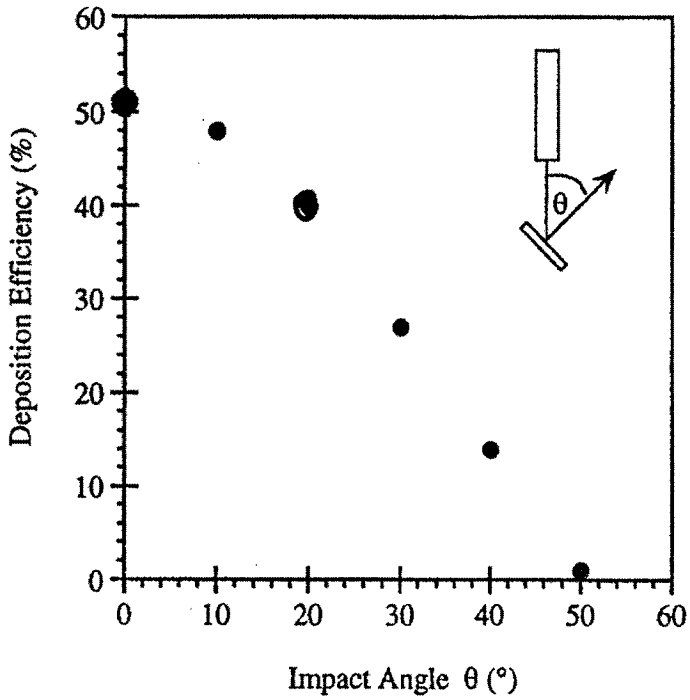

Figure 2-7: Deposition efficiency versus impact angle for the same conditions as Figure 2-6 [20]

The work by these two research groups paved the way for more thorough and diversified works. The concepts at the base of the current work are discussed in the following section. The work previously done on CGDS can be divided into three general areas: the fluid mechanics of the process, the materials used in CGDS and finally the deformation process and bonding mechanism. Each of these areas will be treated independently in the following sections.

2.2.2 CGDS Fluid Mechanics

The research performed on the fluid mechanics of CGDS is mostly concerned with defining a numerical model that will explain and optimize the process. There are a number of published works in this field. Alkhimov et al have published a number of

papers [21, 22, 23] outlining their work, following the submission of their patent [18]. In one of their published works, the driving gas kinematics was modeled to determine the effect of the boundary layer development inside the nozzle on the nozzle exit diameter [21]. This was critical since the nozzle exit diameter is one of the parameters responsible for the gas and particle acceleration. Using the boundary layer theory, the Von Karman equation and empirical results, they were able to determine the boundary layer thickness and compare it with experimental results. They showed that the boundary layer thickness had an adverse effect on smaller particles. They also studied the jet impingement and the thickness of the compressed layer that forms on the substrate surface and how the Mach number varies inside the compressed layer. By determining how the Mach number varies inside the compressed layer, it was found that the particles velocity decreases, thus decreasing the deposition efficiency. Finally, a particle kinematics model using the single particle motion model, which assumes that the particles have no influence on the gas flow, was devised. Predictions were validated experimentally; the model was shown to be adequate. Therefore, it was possible to optimize particle motion parameters.

Work by Jodoin [24] concentrated on the computational fluid dynamics models of CGDS. Using a classical one-dimensional approach along with a two-dimensional axisymmetrical numerical model, it was shown that there are two factors, stagnation temperature and particle shock interaction, which limit the Mach number during the CGDS process. The stagnation temperature can be defined as the temperature of the flow if it is decelerated to zero velocity. The shock-particle interaction is defined as the effect the shock wave has on the particle properties, such as velocity and temperature. Since

coating adhesion is a function of particle kinetic energy; it would be naturally expected that continuously increasing particle velocity would be favourable for the production of coatings. However, Jodoin showed that the Mach number at the exit of the nozzle should be between Mach 1.5 and 3 to minimize the adverse effects caused by high stagnation temperature and loss of kinetic energy due to the shock particle interactions.

By calculating the stagnation temperature at different Mach numbers, the profile in Figure 2-8 is obtained. The Figure shows that a minimum exit Mach number of approximately 1.5 must be reached in order to have a stagnation temperature that will not melt the particles as they impact. The absence of particle melting is desired to produce a coating with the same mechanical and chemical properties as the feedstock, which is one of the advantages of CGDS[2].

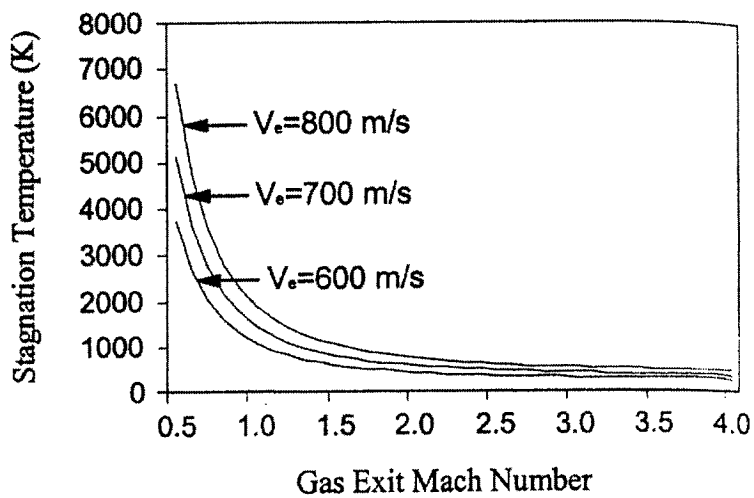

Figure 2-8: Required gas stagnation temperature as a function of the gas exit Mach number for three exit velocities: 600, 700 and 800 m/s [24].

[2] A synthesis of all the advantages of CGDS will be presented in Section 2.4.

The second limiting factor is the particle-shock interaction. Since the flow is supersonic when it impinges on the substrate, a shock wave occurs. The classical one-dimensional approach does not take shock waves into account since it assumes isentropic flow. Therefore, a two-dimensional axisymmetrical flow model is used. The shock wave will produce an increase in gas density and a decrease in gas velocity which will in turn decrease the particle velocity. As the Mach number increases, the opposing drag force acting on the particle after the shock wave will increase. Therefore, a maximum Mach number can be determined. Combining the particle kinematics theory with the drag force equation, Jodoin determined that the maximum Mach number for CGDS process is 3. The two limiting factors provide an interval for the optimal exit Mach number between 1.5 and 3.

2.2.3 Materials used in CGDS

The driving gas, the feedstock particles and the substrate are the important material components of the CGDS process. The following section will detail how the variation of these materials will influence the performance of the CGDS process.

First and foremost, the choices for a suitable driving gas are limited. In early published works [17], helium was used in a mixture with air since it provides a much higher driving gas velocity, and consequently particle velocity, for the same Mach number (560 m/s versus 1400 m/s for Mach 2.6) if compared to air alone. The higher velocity with helium is a result of its higher gas constant with respect to the one for air due to the lower molecular weight of helium, which affects the speed of sound.

Therefore, the driving gas is usually limited to either air, helium, nitrogen or a mixture between two of them [17].

Early studies also evaluated which materials could be sprayed with CGDS as well as the optimal particle diameter. The first successfully cold sprayed materials were ductile metals, namely copper, aluminium, iron, nickel and zinc by Alkhimov et al [17]. That study first showed that different materials will each have a specific critical velocity, which must be attained or surpassed, if significant deposition is to occur. Table 2-1 reports the critical velocity for some of the most commonly sprayed materials.

Table 2-1: Critical velocity for different metal feedstock materials with an average diameter of 20 μm [25]

Material	Density [26] (g/cm^3)	Critical Velocity (m/s)
Copper	8.94	560-580
Iron	7.87	620-640
Nickel	8.90	620-640
Aluminium	2.71	680-700

Interestingly, the material with the lowest density, aluminium, has the highest critical velocity requirement for significant deposition. Vlcek et al [25] proposed that the higher aluminium critical velocity (Table 2-1) is due to a very low force created by the particle during the impact as compared to the other materials. There are conflicting opinions about this theory. It has also been proposed that the higher critical velocity is due to the presence of oxides on the surface of the aluminium particles. These oxides occur when aluminium is in contact with the oxygen present in the air. The oxides coatings on the particles are very hard; therefore, for intimate contact and adhesion to occur between substrate and aluminium particles, the oxide coating must first be broken.

In the area of material development, Vlcek et al [25] have attempted to classify the materials according to their crystalline structure. They proposed that the crystalline structure plays an important role in the adhesion process. Different combinations were studied for both the coating and substrate materials. Their initial conclusion was that the crystalline structure of the material influences the adhesion behaviour of the powder particles since the deformability of the material is function of its crystal structure. It was further found that particles with a higher ductility than the substrate are less successful in adhering, which could imply that substrate deformation is more critical to the adhesion process. Figure 2-9 illustrates the influence of the substrate in the adhesion process by showing three different substrates, an aluminium alloy (AlMgSi), St37 and martensite ($FeCrMo_4$), in Figure 2-9, (a), (b) and (c) respectively. The particle deformation is substrate dependent. The greatest particle deformation occurs with the martensitic substrate where it is observed that the particles are lemon-shaped; while, the particles are still mostly circular or elliptical shaped after impact on the aluminium alloy substrate. Martensite has a body centered tetragonal crystal structure and possesses the same longitudinal and compression elastic modulii as the St37 substrate. It was observed that aluminium, which has a face centered cubic crystalline structure and is more ductile material, had better adhesion characteristics than the other substrates.

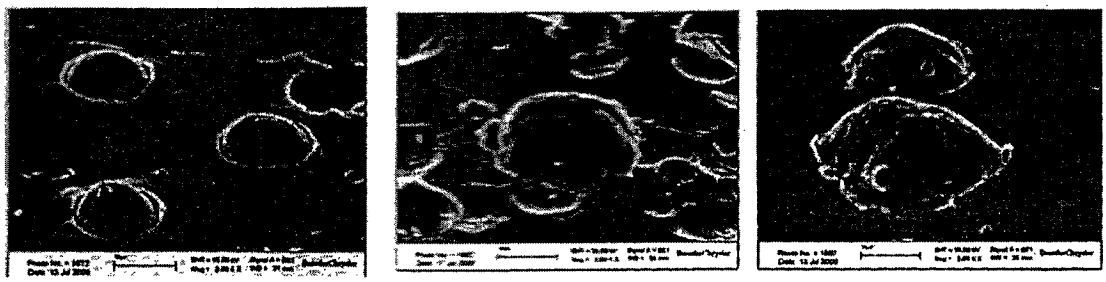

(a) (b) (c)

Figure 2-9: SEM micrographs of 316L particles impacting on different substrates (a) AlMgSi; (b) ST37; (c) $FeCrMo_4$ [25]

In addition to the work done to find the best combination of powder and substrate materials, there have been published works about substrate selection alone. To be a competitive process, it is critical that CGDS can be used to coat different types of surfaces. Zhang et al [27] sprayed 99.7wt% aluminium powder with particle sizes of 75±15μm on a number of metallic, polymeric and ceramic substrates that have significantly different hardnesses. The thickness of the coating after one spraying pass was used to evaluate the ease of coating initiation. The ease of coating initiation was assumed to be the important parameter since the subsequent adhesion will be between impacting and already impacted particles; which should not present an adhesion problem. The substrates used were tin, aluminium alloy, carbon steel, quenched steel, ABS (acrylonitril butadiene copolymer), brass, glass, alumina, copper, normalized steel and tempered steel. A conclusion drawn from their work was that the aluminium powder will require a substrate with a higher hardness in order to successfully initiate coating formation. Also, the presence of oxides on both the powder and the substrate material

when spraying aluminium on an aluminium substrate impedes the process. Particles were successfully sprayed on steel, brass, copper and alumina substrates, albeit with more difficulty on the latter. The coating formation on non-metallic materials was not successful, as shown in Figure 2-10. The glass surface (Figure 2-9 (a) and (b)) was damaged by the impacting particles and few particles adhered to it. The same results were obtained with the ABS substrate (Figure 2-9 (c)).

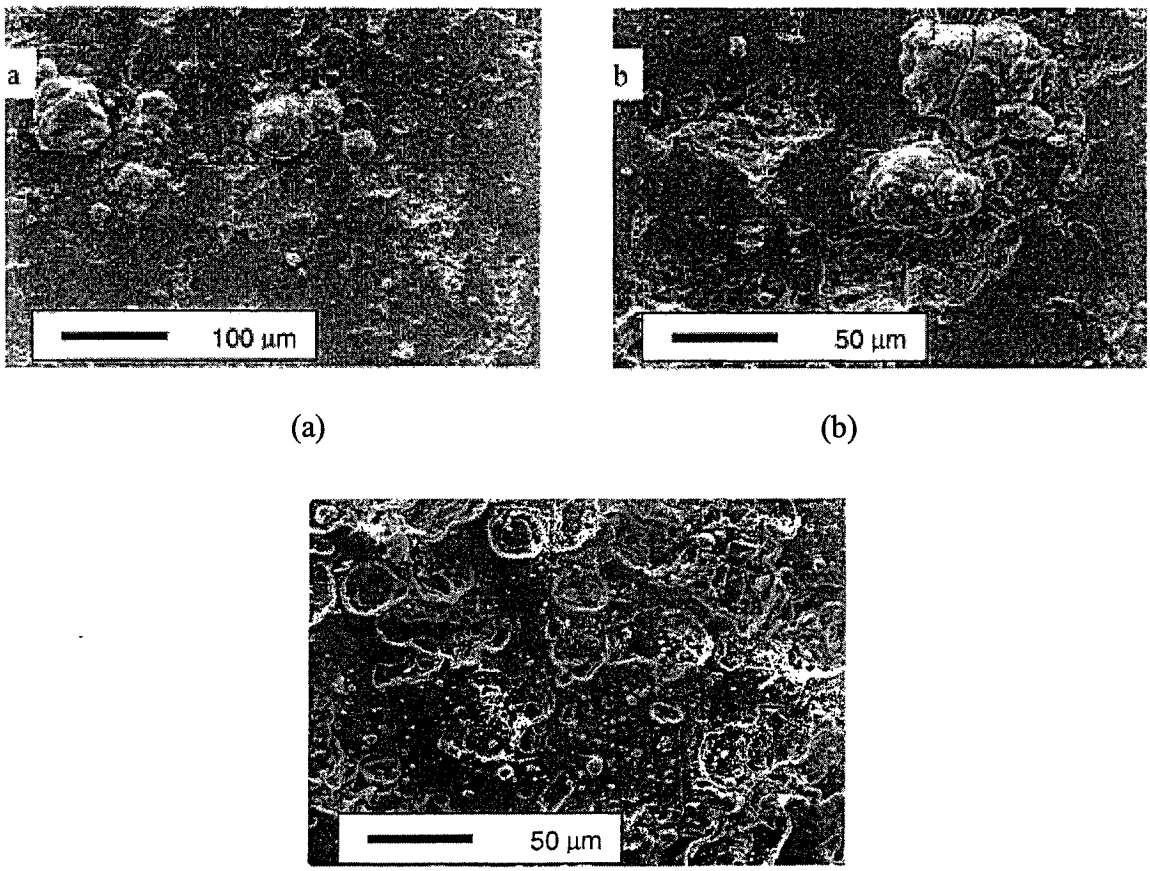

Figure 2-10: Substrate SEM following cold spraying with aluminium particles a) and b) are glass; c) ABS [27].

There have been other works which have sprayed nanocrystalline materials. Coatings formed by nanocrystalline materials are desirable since these can provide mechanical, electrical and thermal properties that are not inherent to conventional materials. CGDS is an ideal process to produce these coatings since it is a solid-state deformation process, therefore the nanocrystalline structure will not be lost; this can occur when there is particle melting during the coating process.

Different nanocrystalline materials have been successfully sprayed, namely, nano-WC/10% Co [28], WC-Co [29], titanium and a hydroxyapatite (HA) and titanium composite powder [30]. Shukla et al [28] have sprayed, with some success, both tungsten carbide particles, and a combination of titanium and HA particles. They also attempted to quantify particle velocities and jet impingement flow fields using particle image velocimetry (PIV). Lima et al [29] have sprayed nanocrystalline WC-Co to form a coating up to 10 μm in thickness. They showed that there was no degradation of the powder during the process and that the nanostructure was conserved. A typical nanocrystalline WC-Co particle (Figure 2-11) has two distinct regions. The light regions represent the nanocrystalline regions while the dark regions between the particles (arrows in Figure 2-11) are voids or porosity that can be found in the coatings produced by CGDS. Their densification theory suggests that those voids will disappear during the CGDS process due to the peening effect of the particles impacting on the substrate.

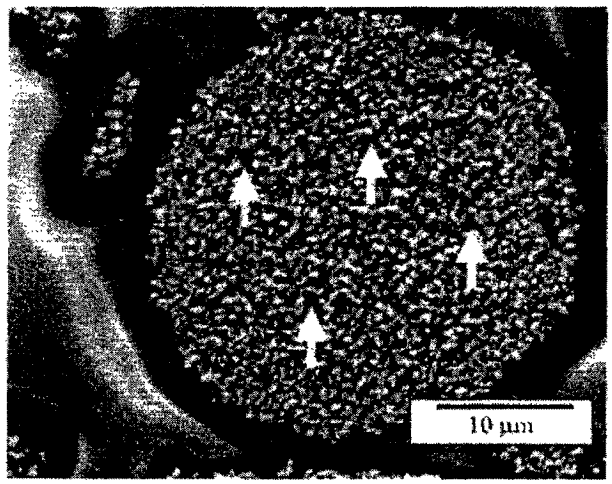

Figure 2-11: Typical nanocrystalline WC-Co particle [29]

A successfully coated substrate with a nanocrystalline powder entails that the coating should conserve the hardness of its previous powdered form. A hardness test will indicate if the powders have conserved their nanostructure. Interestingly, Lima et al [29] reported that the Knoop hardness increased, from 42 ± 7 kgf/mm^2 for the powder to 1225 ± 282 kgf/mm^2 for the coating, which supports their densification theory.

The previous work has focused on many different areas of CGDS. The most disputed area of CGDS, bonding mechanism and deformation, will be discussed in the following section.

2.2.4 Deformation and Bonding Mechanisms

Since CGDS is a relatively new process, not all phenomena involved in the process have been described and quantified. The deformation and bonding mechanisms are the most contentious areas, as there are two different mechanisms proposed in the current literature. In the available body of work, all agree that significant plastic deformation occurs during the CGDS process for the substrate and the particles; however, there have been studies first supporting a theory in which the impact on the substrate will create enough energy to melt the particles and there are other studies supporting a solid adhesion process in which there is severe plastic deformation but no melting. Both of these will be discussed in the following section.

The first argument presented is from a proponent of the localized particle melting theory; a study which has provided experimental validation to support their claim. Bolesta et al [31] sprayed aluminium particles onto a nickel substrate. Following the spraying, the interface created during the process was studied using X-ray grazing diffraction. The resulting diffraction pattern is shown in Figure 2-12. Distinct peaks are visible, showing the presence of the Ni_3Al inter-metallic compound. They hypothesised that the compound can be formed if a chemisorptional bond occurs during the cold spraying process. A chemisorptional bond can be defined as a chemical bond in which the electron density will change and form a bond between the substrate and the particle, which can range from a completely ionic or completely covalent bond [32]. Since a change in the chemical composition has been observed, Bolesta et al assumed that melting had occurred.

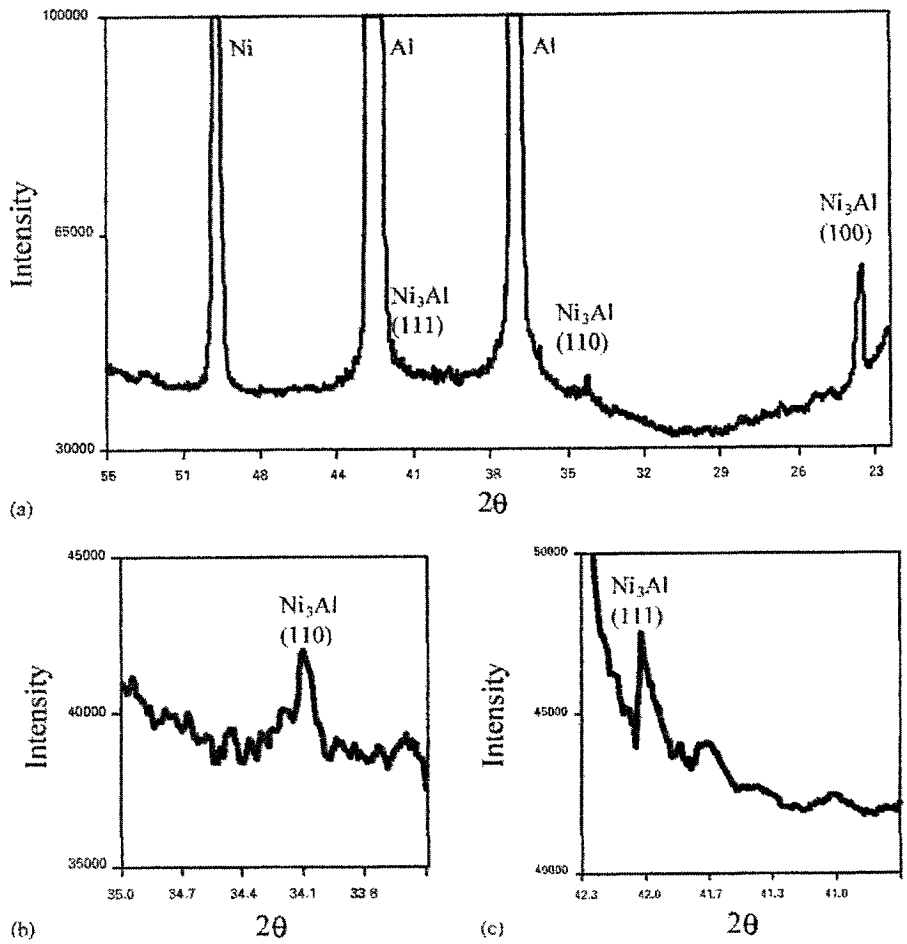

Figure 2-12: Diffraction pattern of the sample obtained by a cold gas-dynamic spraying of aluminium particles on a nickel substrate [31].

In contradiction to the work by Bolesta et al [31], numerous works have been published studying the bonding mechanism of CDGS in which plastic deformation is the principal bonding mechanism and excludes particle melting. Dykhuizen et al [33] stated that the intense plastic deformation occurring at the impact site may disrupt thin surface films, such as oxides, and provide an intimate conformal contact under a high localized pressure. This situation would lead to bonding since it would provide the necessary energy to re-arrange the electrons in the metallic material. The fact that ductile materials

are much easier to spray than non-ductile materials supports this hypothesis. Their experimental results compare favourably with their numerical model which shows that significant plastic deformation of both particle and substrate occurs, as Figure 2-13 demonstrates.

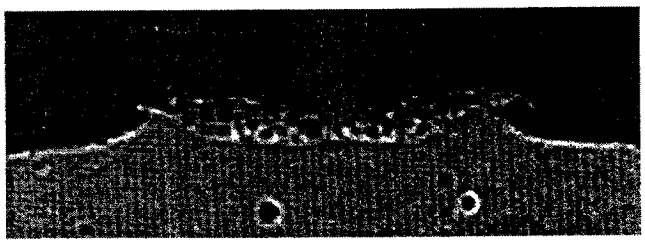

Figure 2-13: Cross section of a splat created by the impact of a 700 m/s copper particle onto a steel substrate [33].

Similarly, the Dykhuizen numerical model (CTH, a computer code generated by Sandia National Laboratories) shows that particle splatter does form as the particle impact velocity increases (Figure 2-14). When the predicted and experimental impacts at 700m/s are compared, their morphology is very similar. Figure 2-14 also shows the increase in temperature at the interface between the particle and the substrate.

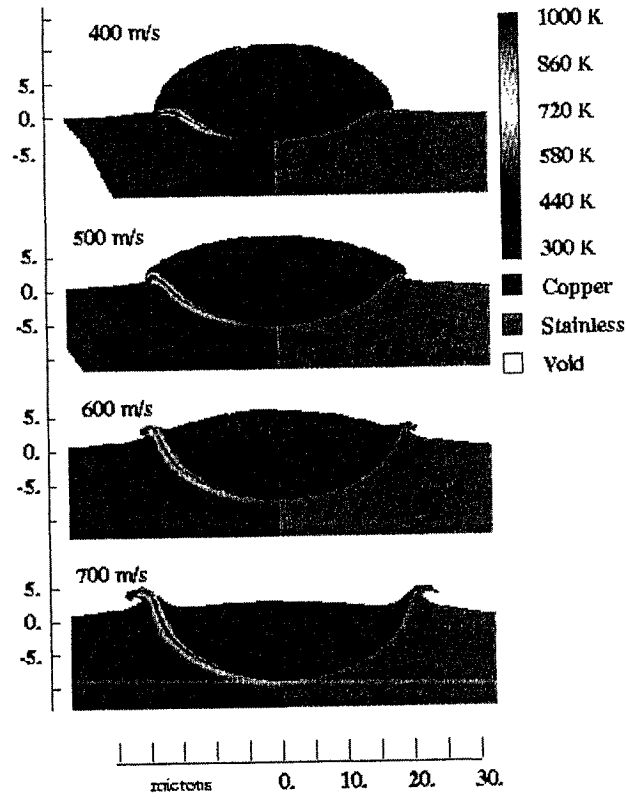

Figure 2-14: Diameter splat shapes created by CTH [33]

Assadi et al [34] also published work on the bonding mechanism in CGDS. The work makes use of a numerical model to simulate particle deformation during impact. A comparison of numerical results with experimental velocity values and impact morphologies was performed. They compared the bonding mechanism in CGDS to the bonding mechanism in explosive cladding or shock wave powder compaction. Experimental work was conducted using copper particles impacting on a copper substrate (Figure 2-15). Their experimental results showed that both the particle and the substrate undergo plastic deformation during impact. Figure 2-15b shows how a jet of material forms around the impact crater. This compared favourably to the impact generated by a computer model illustrated in Figure 2-16.

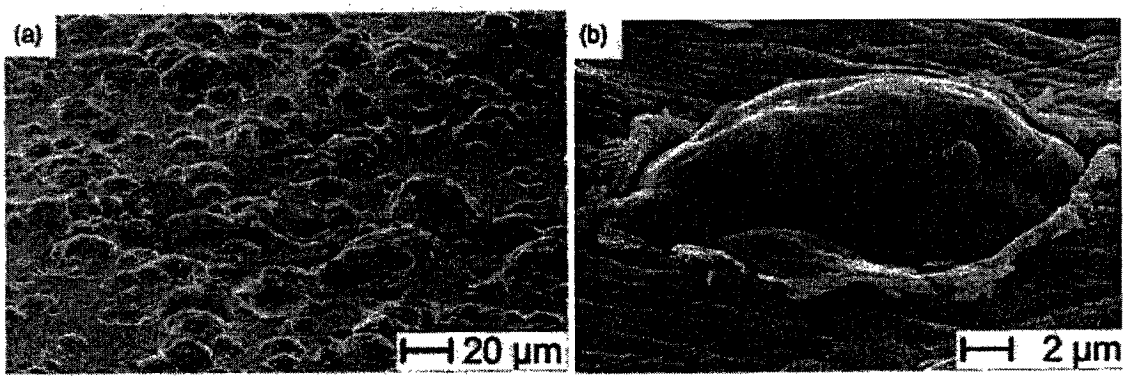

Figure 2-15: Scanning electron micrographs of wipe test samples of copper particles on a copper substrate a) low magnification; b) high magnification [34]

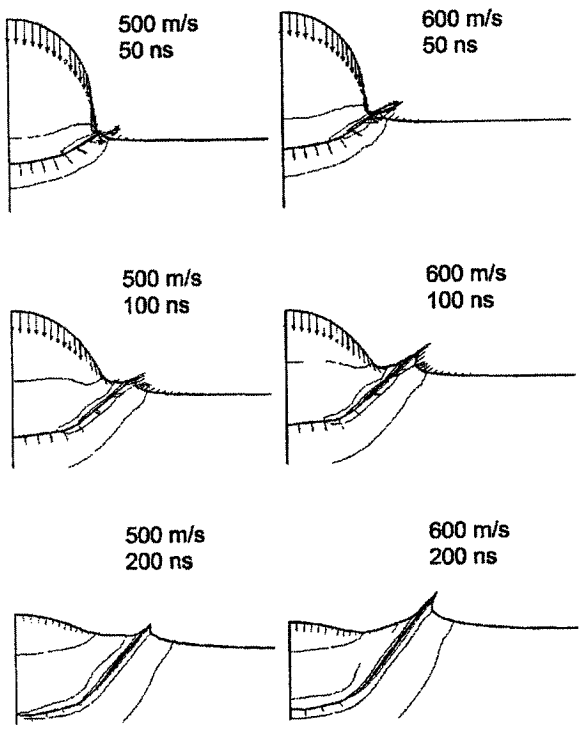

Figure 2-16: Simulated impact of a copper particle on a copper substrate for initial velocities of 500 m/s and 600 m/s at different time intervals (in nanoseconds, ns) [34].

Using those results, Assadi et al [34] proposed that the bonding mechanism in CGDS is the result of the adiabatic shear instabilities occurring at the particle/substrate or particle/particle interfaces. Adiabatic shear instability, which is a phenomenon occurring when a material undergoes a plastic deformation [35], manifests itself by the increase of temperature near the melting point; therefore, their model does not involve particle melting.

Papyrin et al [36] have also studied the deformation of the substrate and the particles and the bonding mechanisms during the CGDS process. Their numerical modeling showed that a high velocity flow of metal in the radial direction can take place near a wall. This resulted in a metal jet forming around the impinging particles, as demonstrated by the arrows in Figure 2-17.

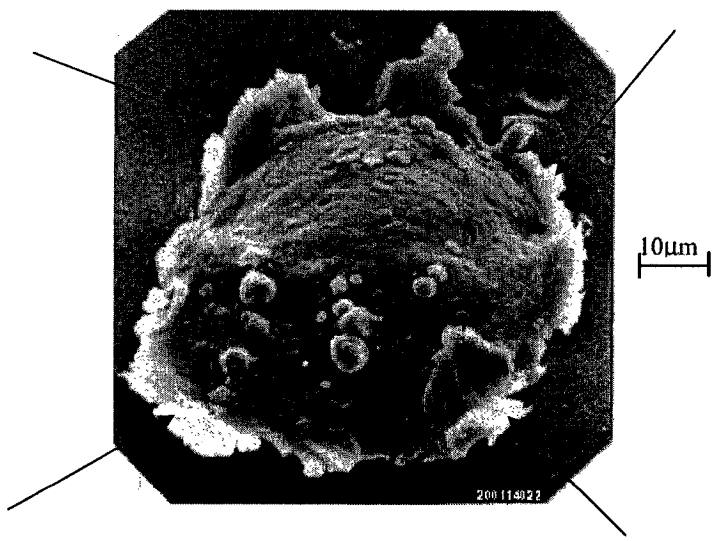

Figure 2-17: Aluminium particle adhered to the surface, d=30μm, V=850 m/s where the arrows indicate the jet formed by the impact of the particle [36].

The outlined results detail the most prevalent theories and findings with respect to CGDS bonding mechanisms. There has also been some works published that describe the coating formation process. Van Steenkiste [16] proposed that there are four regions in a cold sprayed coating which occur at different time stages. These are represented in Figure 2-18.

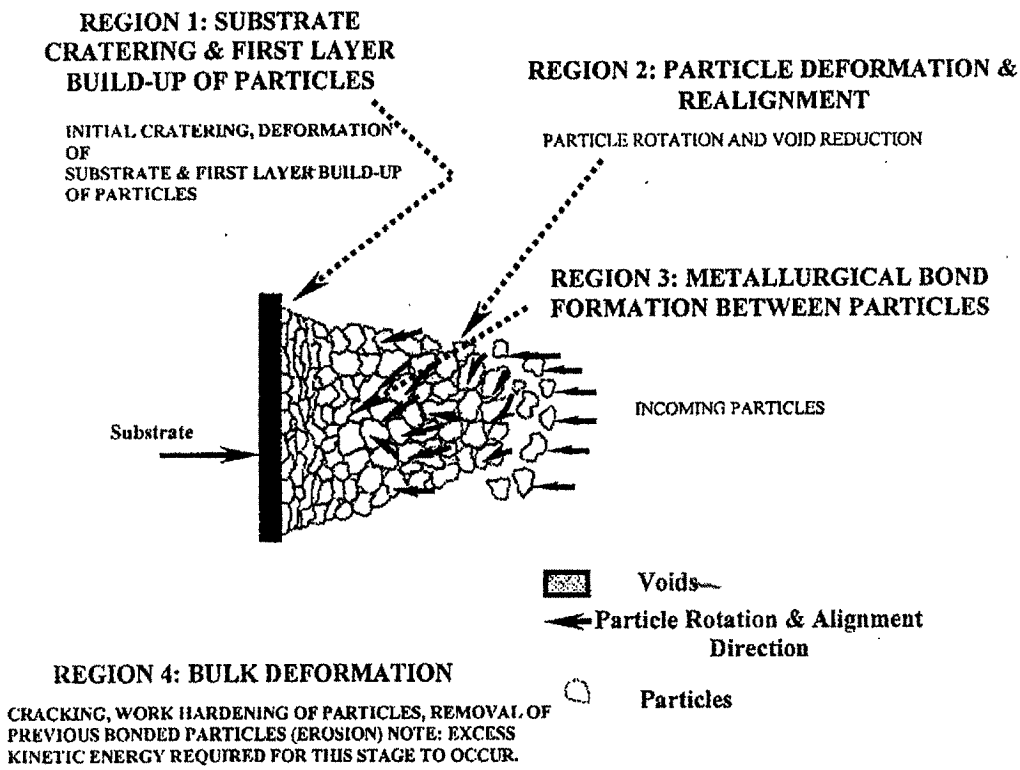

Figure 2-18: Stages involved with the formation of coatings using the kinetic spray process. Region 1: Substrate cratering and first layer build-up; Region 2: Particle deformation and realignment; Region 3: Metallurgical bond formation between particles; Region 4: Bulk deformation occurs if excess kinetic energy is available to particles [16].

The first stage, which is represented by Region 1 in Figure 2-18, occurs when the first particles impinge the substrate and produce craters through plastic deformation before any deposition occurs. Once the first layer is deposited, the second stage begins.

As seen in Region 2 (Figure 2-18), the particles will re-align and plastically deform to reduce the number of, and fill, existing voids. It is assumed that there is little or no bonding occurring in this region. Transition between the second and third stage, to form what is illustrated as Region 3, will occur when the impact kinetic energy of the system increases because of the increase in the mass involved in the collisions. The increase in kinetic energy results in the formation of metallic bonds between the particles. These will be formed when the particles with oxide-less outer surfaces come in contact with each other under high localized pressures. As in region 2, the particles will deform plastically to fill the voids. If the kinetic energy of the system continues to increase as a result of additional impacting particles, the fourth stage will be initiated and there will be bulk deformation of the existing coating. The fourth region is detrimental to the coating formation and should be avoided since the incoming particles will crack and cold work the existing coating. It may even eventually remove some of the already bonded particles.

The studies about CGDS relevant to the current work have been summarized in this section. The following section will discuss the work that has previously been done using aluminium feedstock powders.

2.3 Aluminium Coatings and Characterization in CGDS

Aluminium coatings are widely used for many purposes. The following section will detail the literature available on the cold spraying of aluminium powders. Aluminium has been successfully sprayed in many different particle sizes [31,37] and in metal matrix composites [40]. The goal of this work is to add to the current body of knowledge about cold sprayed conventional and nanocrystalline aluminium coatings. The principal characterization methods used will also be outlined in this section.

Conventional particle diameters used during CGDS are between 1 and 50 μm [17]. Van Steenkiste, Smith and Teets [45] were able to spray much larger aluminium particles, with diameters between 63 and 106 μm using a new nozzle configuration designed by Van Steenkiste et al [38]. Their modified nozzle has a conical converging section and a rectangular diverging section. Using this new design, larger particles were successfully sprayed with a critical velocity lower than that of particles of a smaller diameter (440 m/s for a 65μm particle compared to the 680-700 m/s value reported by Vlcek et al [18]). The lower critical velocity may be explained by the higher energy available to break the oxide layers with the larger particles. The drag force acting on the particle is also dependent on its diameter; therefore, the larger particles might have an advantage due to their greater inertia, which can facilitate the smooth transition into the driving gas flow.

There have been many studies dealing with the spraying of aluminium particles since they are ductile and possess a low density. This made aluminium an ideal candidate for CGDS. Alkimov et al [17] used aluminium in their initial trials to coat a steel pipe [16]. Morgan et al [39] also worked to spray aluminium particles. They focused on the splatter morphology and the metallurgical bonding occurring within the microstructure. The effect of the impact on the grain structure is shown in Figure 2-19. It is possible to see that the particle deformation is not uniform throughout the coating. The impact direction can be deduced using the non-uniform deformation, with the larger deformation located at the front of the impact while the limited deformation occurring at the tail-end of the impacting particle.

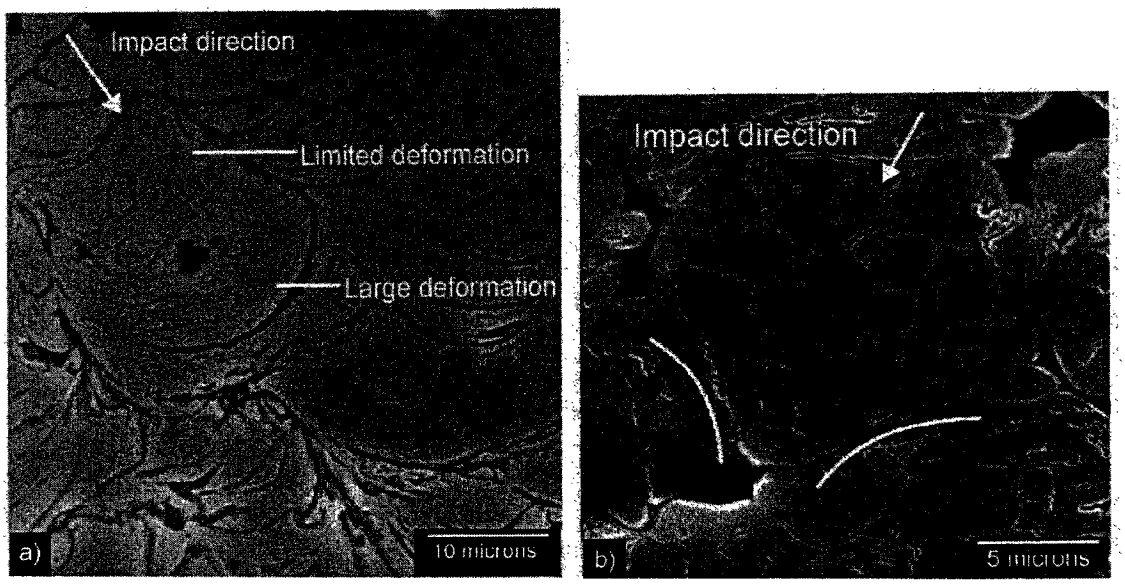

Figure 2-19: Impact of particle has caused deformation of grain structure to impact direction as leading edge [39].

Another interesting result published by Morgan et al [39] is the visualization of the shock waves involved in the CGDS process (Figure 2-20). The expansion waves (oblique shocks) are seen at the exit of the nozzle due to the difference between the nozzle exit and back pressures. A bow shock is clearly visible in front of the substrate. The bow shock is important since it can significantly reduce the particle impact velocity and affect particle-to-substrate adhesion.

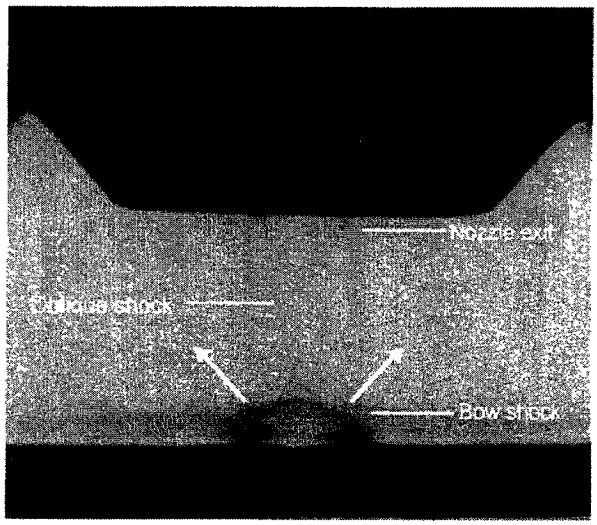

Figure 2-20: Shock waves in CGDS [39]

Aluminium particles were also successfully sprayed as part of a metal matrix composite by Eesley et al [40] with the intent to use this type of coating in electronic packaging applications. Their analysis focused on the thermal conductivity and the thermal expansion coefficient for various compositions of Al-SiC metal-matrix composites. The thermal conductivity is reduced in the Al matrix when compared to pure aluminium. Both thermal properties can be predicted with the known composition. As seen in Figure 2-21, the cross-hatched region indicates how the cold sprayed Al-SiC metal-matrix composites compared with other materials used in electronic packaging.

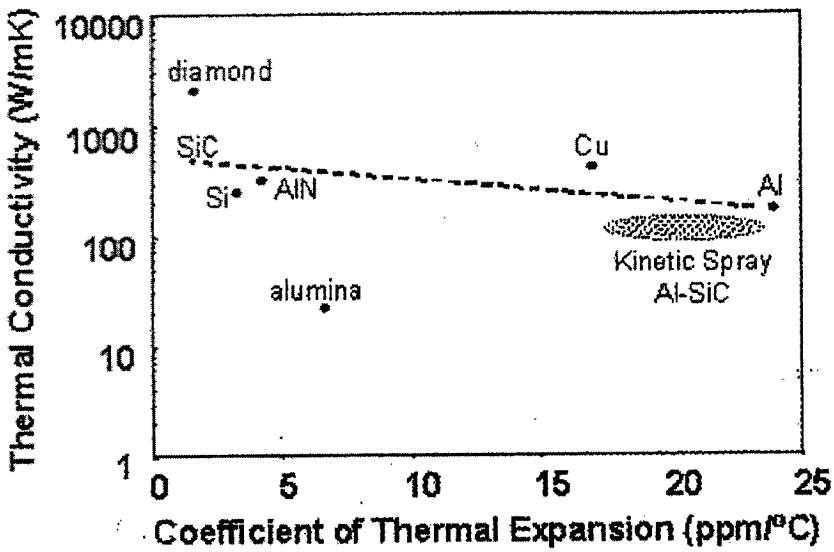

Figure 2-21: Thermal conduction and expansion of selected materials [40]

There are numerous methods for characterizing aluminium coatings. The most common method is the use of scanning electron microscopy (SEM) and transmission electron microscopy (TEM). Another popular method is the use of X-ray diffraction [31, 41, 42, 43]. The hardness test of choice for coatings is the Vickers micro-hardness test. In addition to hardness testing, porosity calculations are used to characterize the coatings [44]. Roughness, bond strength and deposition efficiency [56] have been used as characterization methods as well as residual stress computation [54] and adhesion energy [53].

The current work will use a characterization method similar to Stoltenhoff et al [45]. They evaluated the effect of stagnation pressure and temperature on the deposition efficiency. This was done by keeping either stagnation pressure or stagnation temperature constant for a series of tests. Their results, found in Figure 2-22, showed that a more

elevated stagnation temperature or pressure produced greater deposition efficiency. The goal of such work is to isolate the effect of specific parameters to determine the one most influential on the performance of the coating.

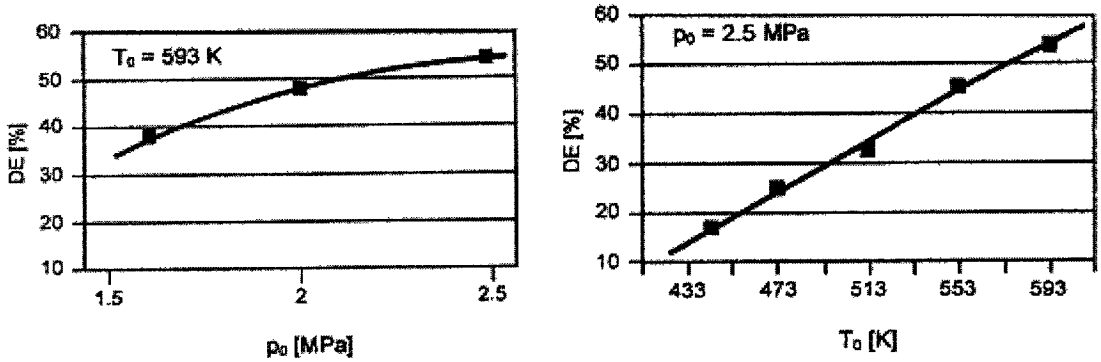

Figure 2-22: Influence of (a) gas pressure and (b) gas temperature on the deposition efficiency. Copper powders from 5-25 μm, spray distance 30 mm [45].

In the previous section, the different types of aluminium successfully sprayed as well as the characterization methods used for most CGDS coatings have been outlined. The details of CGDS have been discussed and it is now possible to compare this new process to the thermal spraying processes outlined earlier in this chapter.

2.4 Cold Gas Dynamic Spraying Process Comparison with Other Processes

Different thermal spraying processes all possess a number of advantages. Figure 2-23 illustrates the different operational regimes in terms of gas temperature and particle velocity for the different thermal spray processes. The four processes discussed in this critical literature review have different operational regimes. Cold Spray does not require the elevated temperatures used in the other thermal spraying processes, which is an advantage when temperature-sensitive materials must be deposited since there will be no significant change in microstructure and properties due to the melting of the particles.

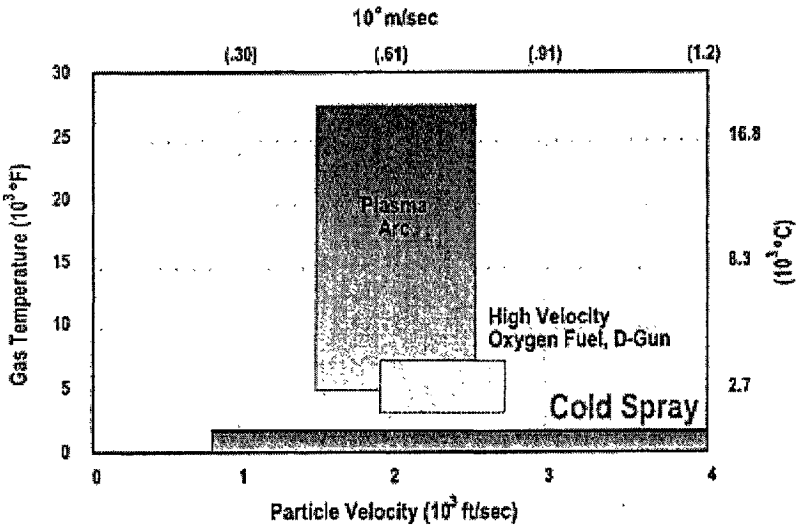

Figure 2-23: Operation regimes for the different thermal spray processes [46]

The main characteristics of the processes are listed in Table 2-2. It is possible to see that each process has very different operational parameters. CGDS has higher carrier gas and particle velocities than the other processes but it also has a much lower operating temperature. The particle feed rate is also higher in CGDS, which can result in a much faster process. Plasma spraying is used to spray a greater variety of particles but the costs

associated with the process as well as the operational security needed make this process less appealing than CGDS. HVOF and D-Gun™ both use lower temperatures and can spray a relatively large array of materials. However, the lower temperatures associated with CGDS do provide it with an advantage since it is believed to avoid chemical reactions which can be present in these other two processes.

Table 2-2: Comparison between thermal spray processes [4, 47]

Process	Typical Carrier Gases	Carrier Gas Speed (m/s)	Carrier Gas Temperature (K)	Operating Pressure (kPa)	Particles Sprayed	Particle Velocity (m/s)	Particle Temperature (K)	Feed Rate (g/min)
Plasma Spraying	Ar, He, H_2, N_2	300-1000	Up to 30000	depends on process	Any material with a stable liquid phase	200-800	Up to ~25000	50-150
High Velocity Oxy-Fuel Spraying	CH_4, C_3H_6, H_2, O_2	500-1200	5500	400-1350	Metallic materials and cermets	200-1000	3300	15-50
Detonation Gun Spraying	O_2, acetone	> 1000	5500	N/A (100 detonation cycles per minute)	Metallic materials and cermets	up to 800	N/A	N/A
Cold Gas Dynamic Spraying	air, He, N_2	400-1400	293-700	1600-3600	Relatively ductile materials and ceramics with ductile phases	450-1400	293	Up to 225

Some of the advantages of CGDS resulting from these operational differences are [47]:

- Particles retain their initial chemical properties in the absence of melting;
- Coatings have a highly wrought microstructure resulting in high hardnesses when compared to traditional thermal coatings;

- Process-long phase and compositional stability due to the lack of phase change during the process;
- Little oxide formation during the coating process as a result of the absence of chemical reactions;
- High deposit density due to the small particle diameter and the continued compaction as other particles impact the coating;
- High hardness since the impacting particles on the coating are analogous to cold working the material;
- It is possible to collect and reuse the particles that did not adhere to the substrate since there is phase and compositional stability in CGDS;
- Operational safety is good since there are no high temperatures involved in the process;
- Possible to obtain an elevated productivity since the powder feed rate can be increased up to 30 lb/hr; and,
- It is possible to obtain a good surface finish by closely following the surface of the substrate.

The aforementioned advantages make cold spray a good choice to deposit coatings since it can produce coatings properties that other processes cannot. CGDS can be used to deposit materials that would have chemically reacted with the plasma or the fuel in the other processes. It can also be used to spray agglomerated nanocrystalline materials knowing that the nanostructure will not be destroyed due to particle melting. It can also spray expensive powders and collect the non-adhered ones and re-use them,

which is impossible to do if they have undergone a phase change. CGDS does provide industrial sectors and researchers with an alternative technique that can solve problems that have been encountered in the past.

The objective of this work is to design a CGDS nozzle through numerical modeling techniques, develop the CGDS system to produce conventional and nanocrystalline aluminium coatings and finally, determine which spraying parameter has the greatest influence on a dependent response variable.

3. THEORY OF COLD-GAS DYNAMIC SPRAYING

The theoretical models of Cold Gas Dynamic Spraying (CGDS) are based on the fundamental laws of gas dynamics as well as fundamental materials engineering principals. In the following section, basic concepts and theories, used to describe the CGDS process, are presented in order to provide the tools to understand the subsequent work and analysis.

3.1 Gas Dynamics

Gas dynamics is the study of high speed flows. It is mainly used in the study of propulsion, turbo-machinery, energy conversion and aerodynamics. The following section will detail the gas dynamics theory used in the CGDS process; as such, the terminology of high speed flows and the general fluid flow parameters will be detailed. The governing equations used, the converging-diverging nozzle analysis along with the shock wave formation and the pressure profiles in the converging-diverging nozzle will be detailed subsequently. Finally, the boundary layer development and its effect on the CGDS process will end the section.

3.1.1 General Fluid Flow Parameters

A general definition of a fluid will be first discussed in this section, followed by the definition of fluid flows and their compressibility under certain conditions The effect of fluid compressibility on the analysis will also be discussed.

3.1.1.1 Definition of a Fluid and Fluid Flow

A fluid is defined as a substance that deforms continuously under the influence of shear forces; this, for any force magnitude [48]. Liquids and gases are defined as fluids; the most appreciable difference between the two lies in the magnitude of the intermolecular bonding force. In the case of a gas, these forces are very small and as a result the gas molecules will occupy all the available volume in the control volume while the stronger intermolecular forces in liquids will be responsible for keeping the fluid volume constant even if there is a change in control volume.

3.1.1.2 Compressibility of Fluid Flows

A fluid flow can have either a compressible or incompressible behaviour when subjected to an external force. When the flow density is constant with respect to pressure, the flow is incompressible; conversely, a compressible flow has a variable density with respect to pressure. Compressibility can be described as the fractional change in volume of the fluid element per unit change in pressure. It is a property of the fluid. For a liquid such as water, a typical value of compressibility [49] is of the order of 5×10^{-10} m^2/N at 1 atm while it is of 10^{-5} m^2/N at 1 atm for air. For a flow to be considered compressible, it must undergo a significant change in density when it is subject to a large pressure gradient. For liquids, a large change in pressure will create a high velocity. Conversely, the same large change in pressure in a gas will create a high velocity as well as a significant variation in density.

3.1.1.3 Fluid flow analysis terminology

The analysis of fluid flow is performed on a control volume (Figure 3-1). In the figure, CV represents the control volume, whose infinitely small thickness, dz, is not represented, CS is the control surface, $\vec{V}$ corresponds to the overall flow velocity entering or leaving the control volume and $\vec{N}$ is the vector normal to the control surface of the system at any point on the surface.

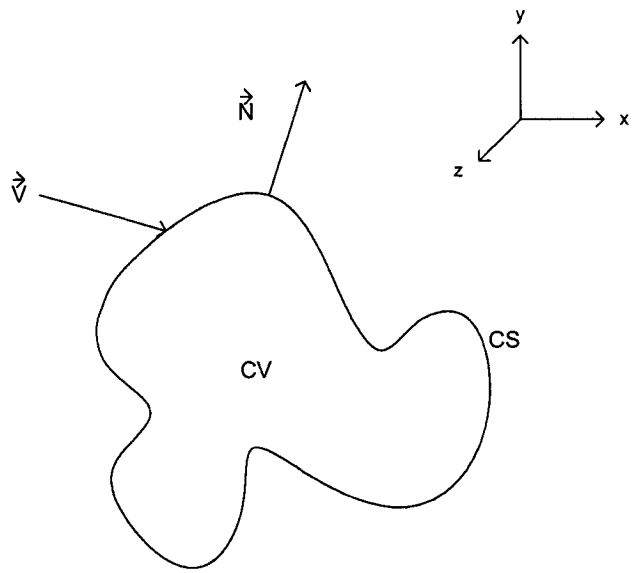

Figure 3-1: Control volume (with infinitesimally small thickness dz) and control surface

3.1.2 Governing Equations

The following section describes the four governing equations used to describe and analyse compressible fluid flow problems, namely, the continuity or mass conservation equation, the linear momentum equation, the energy conservation equation and the entropy equation.

3.1.2.1 Continuity Equation

The continuity equation relates the change of mass inside the control volume over time to the mass flux through the control surface. Since mass can not be created or destroyed during a process, there must be conservation of the mass at all times. Consequently, the continuity equation is as follows:

(3-1)
$$\frac{d}{dt}\int_{CV}\rho d\forall = -\oint_{CS}\rho\left(\vec{V}\cdot\vec{N}\right)dA$$

where $d\forall$ is the infinitesimal volume, dA the infinitesimal area and ρ, the density. The left side of equation (3-1) represents the change of mass inside the control volume over time while the right side of the equation represents the mass flux through the control surface.

3.1.2.2 Newton's Second Law

Newton's Second Law of motion, equation (3-2a), takes a different form when applied to a fluid. It states that the sum of all external forces acting on the system is equal to the time rate change of linear momentum of the system. The usual definition for a solid with a constant mass is:

(3-2a)
$$\sum\vec{F}_{ext} = \frac{d\left(m\vec{v}\right)}{dt}$$

Using Reynold's transport theorem:

(3-2b)
$$\frac{dB_{sys}}{dt} = \frac{d}{dt}\int_{CV}\rho b\, d\forall + \oint_{CS}\rho b\left(\vec{V}\cdot\hat{n}\right)dA$$

The second law is adapted for fluids to become:

(3-2c) $$\sum \vec{F}_{ext} = \frac{d}{dt}\int_{CV} \rho \vec{V}\, d\forall + \oint_{CS} \rho \vec{V}\left(\vec{V}\cdot\vec{N}\right)dA$$

The term on the left-hand side of the equality in equation (3-2c) encompasses all the possible external forces that can act on the control volume. For a fluid, these can be body forces (i.e. gravity), shear forces and pressure forces. The first term on the right hand side of the equality represents the time-based rate of change of the momentum of the fluid mass in the control volume. The second term on the right-hand side of the equality represents the momentum of the fluid entering or leaving the control volume over the control surface. Since this is a vector equation, it can be evaluated in the axis of the selected coordinates, i.e. x, y and z for the Cartesian system as seen Figure 3-1.

3.1.2.3 Energy Conservation Equation

The energy conservation equation is the rate of change with respect to time of the energy for the control volume. This equation is also known as the first law of thermodynamics and is expressed as follows:

(3-3) $$\frac{\partial}{\partial t}\iiint_{C.V.} e\rho\, d\forall + \iint_{S}\left(h + \frac{V^2}{2} + gz\right)\left(\rho\vec{V}\cdot d\vec{A}\right) = \frac{d}{dt}(Q - W)$$

where:

- $\frac{\partial}{\partial t}\iiint_{C.V.} e\rho\, d\forall$ is the time-dependent change in the total energy of the control volume, where e is the internal energy of the system and $d\forall$ is the infinitesimal volume;

- $\iint_S \left(h + \frac{V^2}{2} + gz\right)\left(\rho \vec{V} \cdot d\vec{A}\right)$ is the change of energy on the control surfaces where h is the enthalpy of the flow, V is its velocity, gz is the potential energy, ρ is the density, $\vec{V}$ is the velocity vector and $d\vec{A}$ is the infinitesimal area;

- $\frac{dQ}{dt}$ is the rate of heat transfer to the control volume, and finally;

- $\frac{dW}{dt}$ is the rate of work done to or by the control volume.

3.1.2.4 Entropy Equation

The entropy equation introduces a new state variable, the entropy of a system, S. The entropy of a system can be described as a state variable that indicates the proper direction of a process [49]. Equations (3-1) to (3-3) state that the energy of a system must be conserved; therefore, it would be acceptable that an ice cream cone on a hot summer day would become even colder and the surrounding air would become hotter. With the inclusion of entropy as a new state variable, that process becomes impossible. Mathematically, it is possible to relate entropy to the other state variables as follows:

(3-4)
$$\frac{\partial}{\partial t}\iiint_{CV} \rho s \, d\forall = \iint_{CS} \rho s \vec{V} \cdot d\vec{A} + \iint_{CS} \frac{\dot{Q}}{T} d\vec{A} + \iint_{CS} \dot{S}_{gen} \, d\forall$$

where:

- $\frac{\partial}{\partial t}\iiint_{CV}\rho s d\forall$ is the time dependent change of entropy inside the control volume, where s is the specific entropy of the system;
- $\iint_{CS}\rho s\vec{V}\cdot d\vec{A}$ represents the change in entropy over the control surface of the system;
- $\iint_{cs}\frac{\dot{Q}}{T}d\vec{A}$ represents the heat transfer over the control surface of the system; and,
- $\iint_{CS}\dot{S}_{gen}\, d\forall$ represents the entropy generated in the control volume during the process. The generated entropy can be a result of friction or other process irreversabilities.

Equation (3-4) states that the rate of change in total entropy inside the control volume is equal to the net sum of entropy fluxes across the control surface and the generation rate.

3.1.3 Velocity of a Flow, Speed of Sound and Mach Number

The velocity of a flow is dictated by the pressure gradient. The fluid will flow from the high to the low pressure region. The flow velocity is directly proportional to the pressure gradient. The flow velocity can be expressed as a function of the local speed of sound, c, and the Mach number. The Mach number is defined as:

(3-5) $$M = \frac{V}{c}$$

where V is the local flow speed and c is the local speed of sound. The local speed of sound is the measure of the propagation velocity of an infinitesimal pressure wave. The general expression for the local speed of sound is:

(3-6) $$c = \sqrt{\left(\frac{\partial P}{\partial \rho}\right)_s}$$

where $\partial P/\partial \rho$ represents the change of pressure with respect to the change in density, and the subscript s indicates an isentropic process, which occurs when the process is adiabatic and reversible. Since sound propagates in the form of an infinitesimal pressure wave, its thickness is infinitesimal and no heat transfer can occur over such a small area (thickness multiplied by the length), rendering the process adiabatic and reversible and by extension, isentropic.

If the process involves a perfect gas, the density of the system can be expressed as a function of the other state variables, as follows:

(3-7) $$\frac{P}{\rho} = RT$$

where P, ρ and T are the local pressure, density and temperature, respectively.

If the sound is propagating isentropically through a calorically perfect gas, which is a gas that, regardless of its state, has constant values of C_p and C_v, constant-pressure and constant-volume specific heats, respectively, combining equations (3-6) and (3-7) will result in the following equation for the speed of sound:

(3-8) $$c = \sqrt{\gamma RT}$$

where γ is the specific heat ratio (C_p/C_v) and R is the gas constant.

If a flow is traveling at a velocity less than the local speed of sound, it is defined as a subsonic flow. When the flow is traveling at the same velocity as the speed of sound, it is a sonic flow. Finally, a flow is supersonic when its velocity exceeds Mach 1.

When a point source travels through a medium, it creates a disturbance in the form of an infinitesimal pressure wave traveling at the local speed of sound. Figure 3-2 shows the difference between the propagations of subsonic and supersonic flows. If the flow is subsonic, the waves emitted by the point source will propagate according to Figure 3-2a. As the point source travels, the sound waves will propagate, spreading in the fluid. They will travel upstream of the point source. As the point source approaches the receiver, the pressure waves will be closer to one another. This is known as the Doppler Effect. For supersonic flow, the point source travels faster then the actual wave it emits. The resulting propagation pattern is illustrated in Figure 3-2b. The information about the

flow cannot be processed prior to the point source since it is traveling faster than the wave. This results in a zone of action, bound by the Mach cone (Figure 3-2b), where the information about the perturbation can be processed. A cone of silence exists outside the Mach cone. It can be seen for a supersonic flow that the waves emitted by the perturbation do not reach the flow before the flow reaches the perturbation. The information concerning the perturbation in front of the flow is not processed since the flow reaches the perturbation before the sound wave can make it back to the flow.

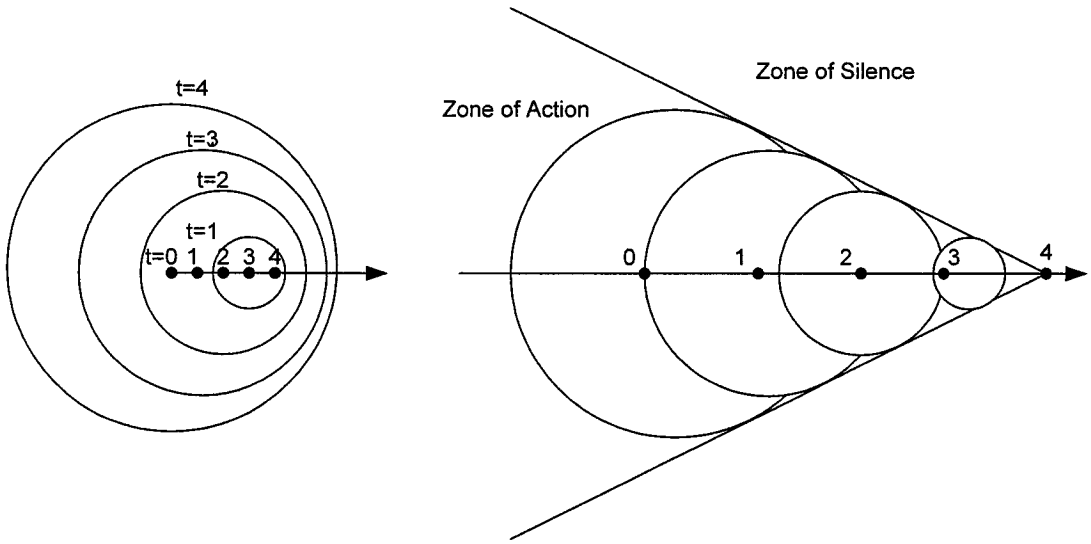

Figure 3-2: Flow propagation for (a) subsonic flow; (b) supersonic flow at 5 different times (t=0 to t=4). Position where the source emits the waves are represented by 0 to 4.

The equations discussed in this section are the basis for the theoretical analysis of the fluid flow during the cold spraying process. Using the equations described in this section, it is possible to develop equations that will enable the design of the converging-diverging nozzle used to accelerate the flow to supersonic velocities in the CGDS process.

3.1.4 Converging-Diverging Nozzle Analysis

A converging-diverging nozzle is used in the CGDS process to accelerate the driving gas to supersonic velocities. Figure 3-3 illustrates such a nozzle. The process by which the flow becomes supersonic will be discussed in more detail in the subsequent sections.

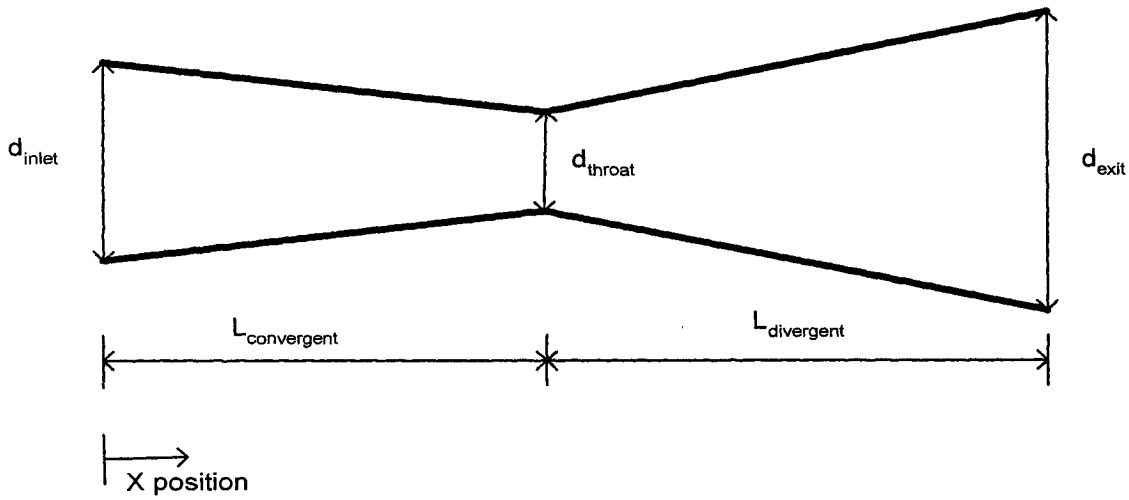

Figure 3-3: Geometry of a converging-diverging nozzle

3.1.4.1 Description of a Converging-Diverging Nozzle

The design of a converging-diverging nozzle is the first step in designing a CGDS set-up since it is used to accelerate the driving gas to supersonic velocities. Initially, the theoretical calculations for a compressible flow must be performed to determine the necessary physical and geometrical parameters of the nozzle. In order to simplify these calculations, the following assumptions are made:

- steady-state, steady-flow;
- reversible and adiabatic, thus isentropic process, and;

- flow calculations can be reduced to a one-dimensional problem because the changes in flow properties normal to the streamlines are negligible compared the rate of change along the streamlines. Figure 3-4 illustrates the difference between one-dimensional and a two-dimensional flow. Points 1 and 2 are located in the one-dimensional flow regime where the streamlines are constant in the vertical direction, only varying in the horizontal direction. Points 3 and 4 show that a two-dimensional flow will vary not only along the direction of the streamline, but also in the direction normal to it, resulting in profile that varies in two directions.

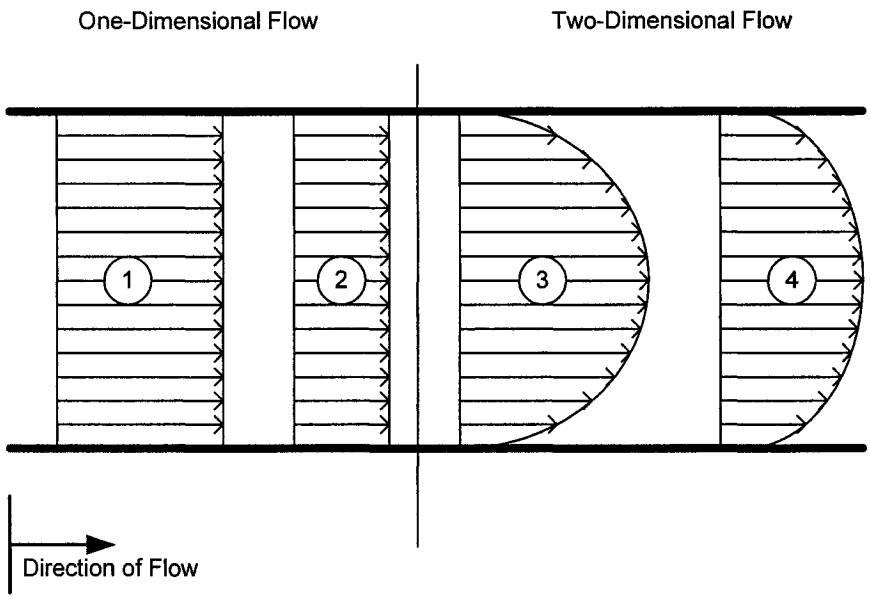

Figure 3-4: Comparison of one and two-dimensional flows in a constant area duct: 1-2: One-dimensional flow; 3-4: Two-dimensional flow.

With these assumptions, it is possible to obtain a relationship between the change of area and the change of pressure from the mass conservation equation and the linear momentum equation as follows [50]:

(3-9)
$$\frac{dA}{A} = \frac{dP}{\rho V^2}\left(1 - M^2\right)$$

where A is the local cross-sectional area of the nozzle, P is the local pressure, ρ is the density of the fluid traveling in the nozzle and M is the Mach number.

It is also possible to relate the effect of the pressure variation to the change in velocity by manipulating the momentum equation for fluids (3-2c) in the x-direction to obtain the following relationship:

(3-10)
$$dP = -\rho V\, dV$$

Equation (3-9) expresses the change in cross-sectional area as a function of the pressure change, the velocity, the density and the Mach number while equation (3-10) relates the pressure change to the change in velocity. If equations (3-9) and (3-10) are combined, it is possible to relate the change in area to the change in pressure and the change in velocity. For a subsonic flow, an increase in cross-sectional area will result in an increase of pressure and a decrease in velocity, since the term $(1\text{-}M^2)$ is positive. Similarly, a decrease in cross-sectional area for a subsonic flow will result in the opposite effect. When the flow is supersonic, the term $(1\text{-}M^2)$ is negative, which results in an increase in velocity and a decrease of pressure when the cross-sectional area increases.

For a decrease in cross-sectional area, the velocity will decrease and the pressure will increase.

To obtain a sonic flow, M=1, the change in cross-sectional area must be zero. This occurs at the minimum cross-sectional area, which is located at the throat of the nozzle. Therefore, sonic flow will only occur at the throat of a converging-diverging nozzle. Sonic flow at the throat of a converging-diverging nozzle is not inherent to every possible geometry and parameter combination. There are two flows regimes possible in the converging portion of the nozzle: choked and unchoked flows. A flow is considered choked when the back pressure, which is the pressure outside the nozzle, is lower than the critical pressure. The critical pressure value is the pressure required for the flow to be sonic. When the flow is choked, the sonic flow at the throat can accelerate in the diverging portion and the pressure waves from the exhaust region cannot propagate upstream if the flow in the diverging portion remains supersonic. Therefore, the flow does not adjust to the exhaust conditions prior to reaching them.

3.1.4.2 Stagnation Properties in a Converging-diverging Nozzle

Stagnation properties are important parameters used in the study of an isentropic compressible flow. They represent the properties of the flow at any given point in a flow field if it was decelerated from the local velocity to a zero velocity condition following a frictionless, adiabatic process [48]. The stagnation properties are often used as a reference state. When studying the flow through an isentropic converging-diverging nozzle, the properties of the gas at the entrance of the nozzle are often taken as the local stagnation

properties because inlet flow velocity is negligible as compared to exit flow velocity; therefore, it can be assumed to be equal to zero.

The four governing equations, equations (3-1) to (3-4), can be simplified for the study of the flow through a converging-diverging nozzle. The simplified form relates the stagnation properties to the local fluid properties at any point in the flow. The following ratios can be derived, if the assumptions used for the converging-diverging nozzle are valid [50]:

(3-11)
$$\frac{T_o}{T} = 1 + \frac{(\gamma - 1)}{2} M^2$$

(3-12)
$$\frac{P_o}{P} = \left[1 + \frac{(\gamma - 1)}{2} M^2\right]^{\frac{\gamma}{\gamma - 1}}$$

(3-13)
$$\frac{\rho_o}{\rho} = \left[1 + \frac{(\gamma - 1)}{2} M^2\right]^{\frac{1}{\gamma - 1}}$$

Equations (3-11) to (3-13) relate the local properties (T, P and ρ) to the stagnation properties (T_o, P_o and ρ_o) as a function of the local Mach number and the specific heat ratio (γ). It is also possible to use the above equations to determine the Mach number at a specific position in the nozzle if the magnitudes of the stagnation property and the local property are known. Similarly, it is possible to determine the magnitude of the local properties if the stagnation property and the local Mach number are known.

The ratio of throat (A^*) to exit area (A_e) along with the stagnation pressure (P_o) to exit pressure (P_e) ratio are used in the analysis of a supersonic problem. For a given pressure ratio and sonic flow at the throat, a ratio between the throat cross-sectional area and the cross-sectional area (A) at another point in the nozzle can be derived as a function of the Mach number at that point. Manipulating the continuity equation and the property ratios results in the following equation:

$$\frac{A}{A^*} = \frac{1}{M}\left[\left(\frac{2}{\gamma+1}\right)\cdot\left(1+\left(\frac{\gamma-1}{2}\right)M^2\right)\right]^{\frac{\gamma+1}{2(\gamma-1)}} \tag{3-14}$$

From equation (3-14), it is possible to determine what exit to throat ratio is needed to obtain a desired exit Mach number. The Mach term in this equation is squared; therefore, there are two Mach numbers associated with each area ratio: one subsonic and one supersonic. The pressure ratio will determine whether the exit flow is subsonic or supersonic. If the flow is assumed to be at sonic velocity at the throat (M=1), it is possible to obtain an equation for the maximum mass flow possible in the nozzle at the throat as follows:

$$\dot{m} = A^*\sqrt{\frac{\gamma}{R}\left(\frac{2}{\gamma-1}\right)^{\frac{\gamma+1}{\gamma-1}}}\cdot\frac{P_o}{\sqrt{T_o}} \tag{3-15}$$

where P_o and T_o are the stagnation pressure and temperature respectively.

3.1.5 Shock Waves

A nozzle design will produce an isentropic supersonic flow if suitable area and pressure ratios are selected. However, improper pressure ratios will produce the undesirable phenomenon of a shock wave (Figure 2-20). A shock wave produces a very abrupt and rapid change in the properties of a supersonic flow due to the lack of propagation of the downstream conditions. A shock wave is an irreversible process that will occur in extremely thin zones[3] in which the flow goes from a supersonic velocity to a subsonic velocity. The pressure in the flow will also increase after the shock wave. The decrease in velocity and increase in pressure make the shock wave an undesirable phenomenon since it will decrease the kinetic energy of the particle being sprayed which can, specifically in CGDS, decrease the deposition efficiency since it is dependent on the particle velocity.

A shock wave can be normal to the flow, curved or oblique to the flow. After a normal shock wave, the flow is subsonic. An oblique shock wave slows down the flow but will not necessarily render it subsonic since the magnitude of the velocity can remain supersonic after the shock. Normal and oblique shock waves are illustrated in Figure 3-5 and Figure 3-6 respectively.

---

[3] Typically, the thickness of a shock wave is in the order of a few mean free paths, around 10^{-5} cm for air at standard conditions [49].

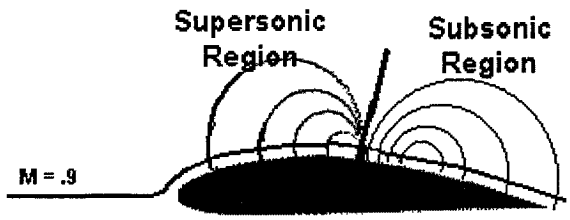

Figure 3-5: Normal shock wave [51]

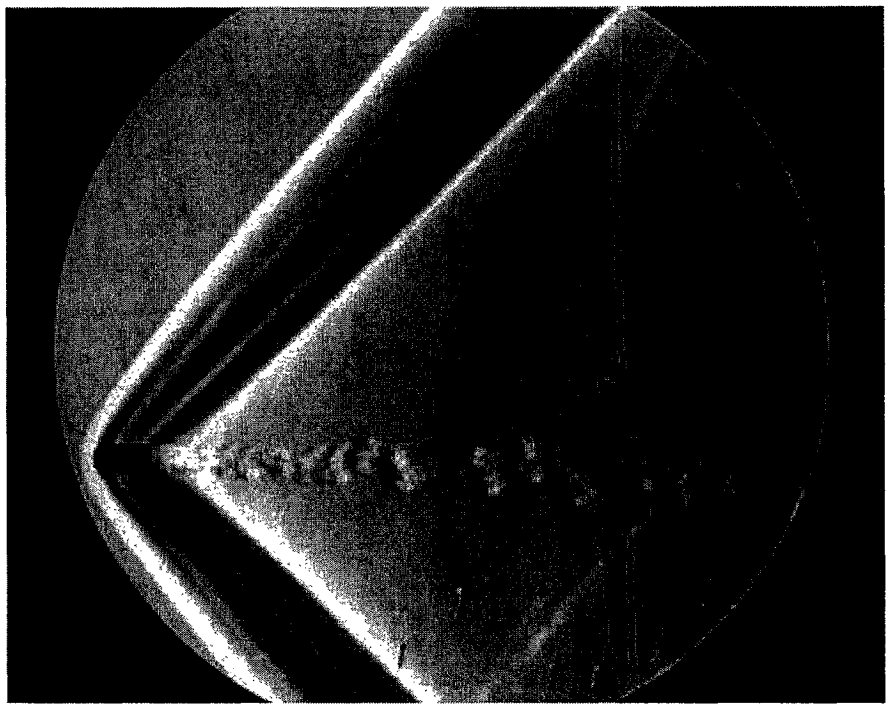

Figure 3-6: Oblique shock waves in front of supersonic bullet [52]

At the exit of the nozzle, the free boundary will produce wave reflection if the exit pressure is lower than the back pressure. Expansion and compression waves will modify the pressure of the flow in order for it to match the ambient pressure in which it is exiting. Figure 3-7 shows the expansion and reflected waves at the exit of a supersonic nozzle.

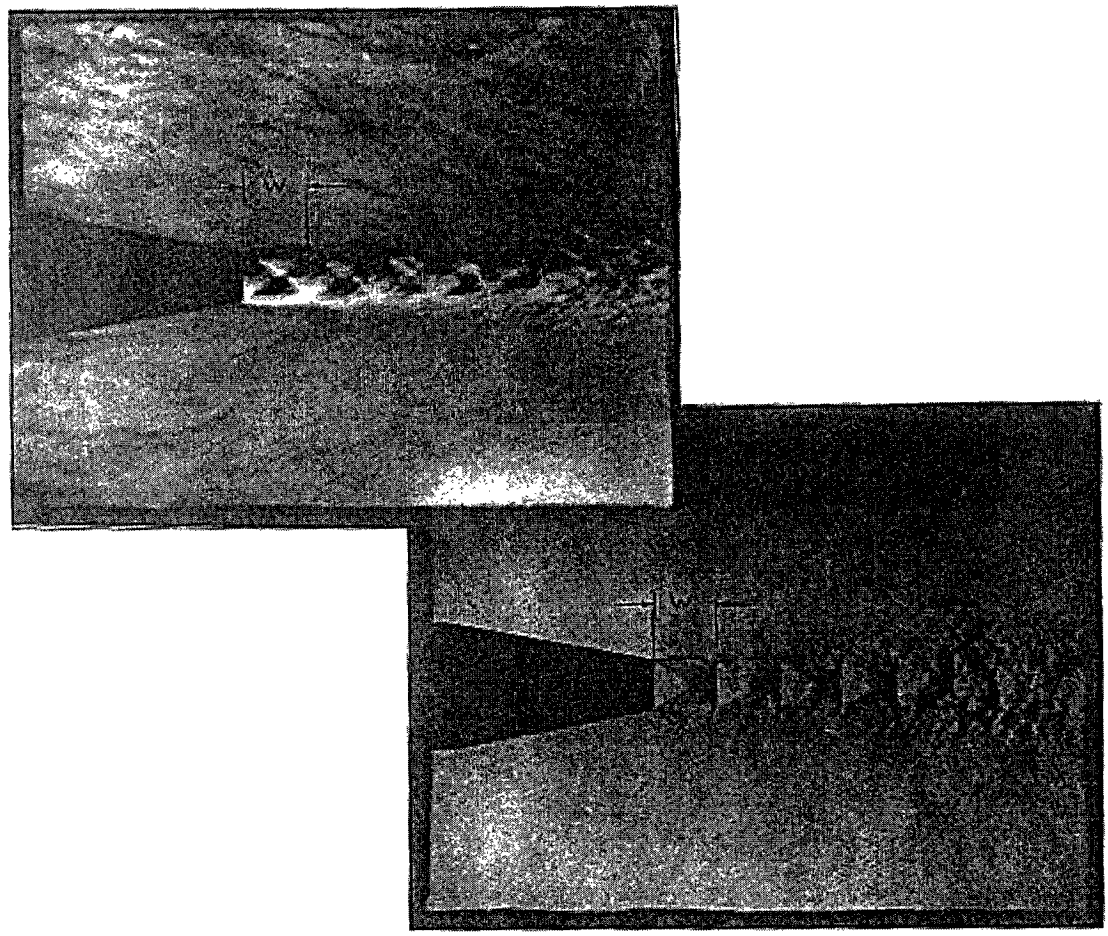

Figure 3-7: Expansion and reflected waves at the exit of a converging-diverging nozzle [49] (Photographs taken using a Schlieren Camera)

A relationship can be derived between the conditions prior to a normal shock and the conditions after it for a calorically perfect gas. Assuming that the Mach number and the conditions before the shock wave are known, the following equations, derived from the continuity, linear momentum and energy equations are used to evaluate the post-shock conditions [50]:

(3-16)

$$\frac{P_y}{P_x} = \frac{2\gamma}{\gamma+1} M_x^2 - \frac{\gamma-1}{\gamma+1}$$

(3-17)
$$\frac{T_y}{T_x} = \frac{\left(1+\frac{\gamma-1}{2}M_x^2\right)\left(\frac{2\gamma}{\gamma-1}M_x^2-1\right)}{\left(\frac{\gamma-1}{2(\gamma-1)}\right)M_x^2}$$

(3-18)
$$M_y^2 = \frac{M_x^2+\frac{2}{\gamma-1}}{\frac{2\gamma}{\gamma+1}M_x^2-1}$$

where, the conditions after the shock have the subscript y and the conditions prior to the shock have the subscript x. If the shock wave is not normal to the flow, the velocity component normal to the shock is the only one undergoing the deceleration.

Since the shock wave is an irreversible process, there is entropy generation. The stagnation pressure and the stagnation density will change due to the shock wave. Figure 3-8 shows the variation of property ratios with the initial Mach number. It shows how the stagnation pressure ratio varies, going from 1 at Mach 1 to approximately 0.12 at Mach 4. The greater the Mach number before the shock, the larger the loss of stagnation pressure.

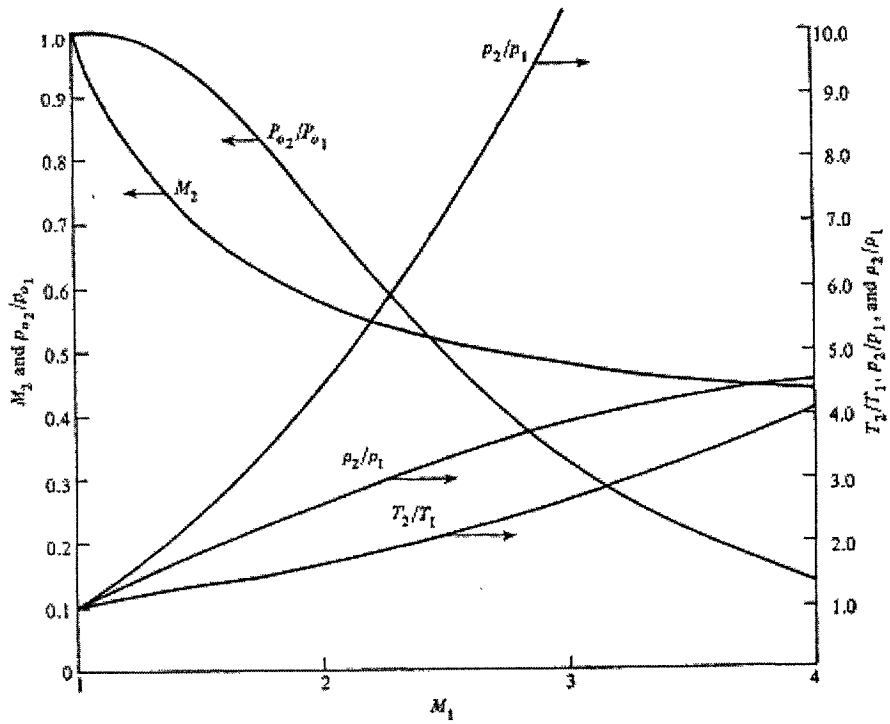

Figure 3-8: Change in properties before and after a shock wave as a function of the Mach number [49]

Stagnation properties are influenced by a shock wave. There is a loss of stagnation pressure when the process undergoes a shock wave ($P_{oy}<P_{ox}$) due to the increase in entropy which results from the irreversibility of the shock wave, but the stagnation temperature and stagnation enthalpy will remain the same because of the conservation of energy.

3.1.6 Pressure Profiles in a Converging-Diverging Nozzle

It is possible to predict whether or not shock waves will occur inside or outside a converging-diverging nozzle. The manner in which the flow develops depends on the stagnation pressure, P_o, and the back pressure, P_b. The back pressure can be defined as the pressure downstream of the nozzle exit, which is unaffected by the pressure changes

inside the nozzle. In Figure 3-9, seven different possible pressure profiles inside the converging-diverging nozzle are illustrated. The ratio between inlet pressure and back pressure dictates the shape of the pressure profiles.

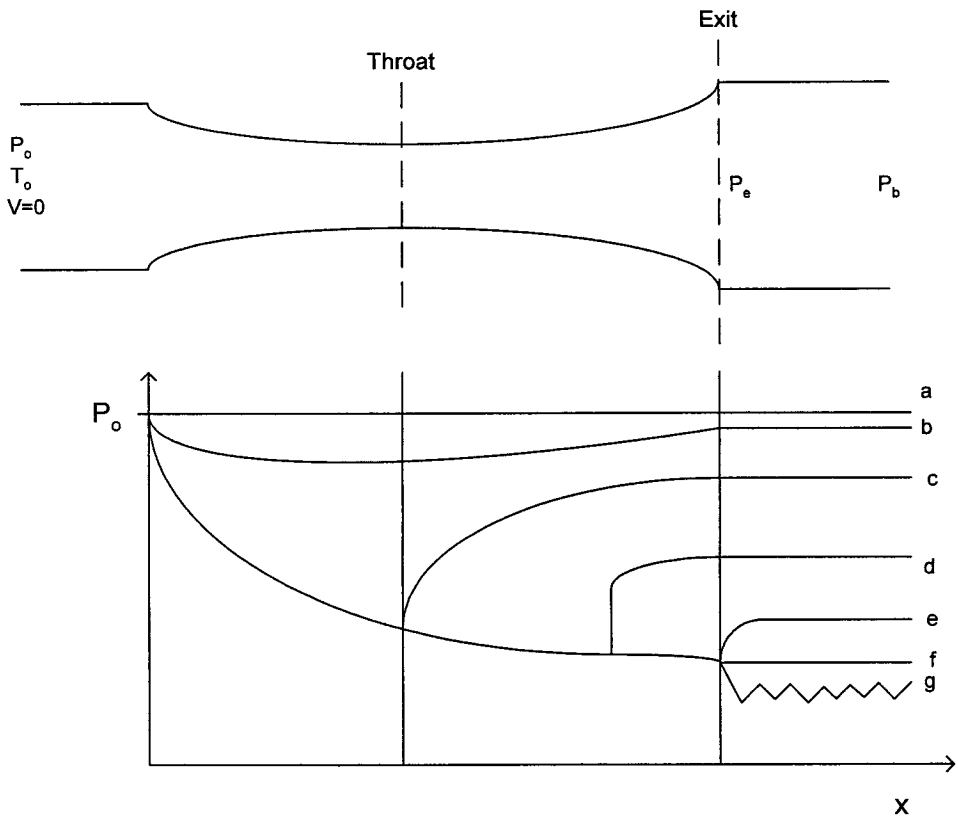

Figure 3-9: Pressure profiles as a function of back pressure

The first pressure profile, Figure 3-9 (a), represents the situation when the back pressure is equal to the stagnation pressure. The lack of pressure gradient will prevent the flow from traveling through the nozzle.

The second profile (b) illustrates the case when the back pressure is slightly lower than the stagnation pressure. Since the pressure at the throat is higher than the required pressure for choked flow, the flow will be subsonic in both the convergent and the

divergent sections of the nozzle and no shock waves will be produced. As the flow travels through the nozzle, its pressure will decrease until it reaches the throat. At the throat, the pressure will have its smallest magnitude but the flow will still be subsonic. In the divergent portion of the nozzle, the pressure will increase as shown by equation (3-9), and will reach the back pressure at the nozzle exit. The flow obtained in this case is isentropic.

Profile (c) represents the case when the velocity at the throat is sonic. The divergent section produces an increase in the pressure and a decrease in velocity, which brings the flow back to a subsonic speed because the pressure at the exit of the nozzle is too high. The flow obtained in this case is isentropic.

The following profile, (d), is a non-isentropic case, due to the presence of a shock wave inside the nozzle. The flow will reach sonic velocity at the throat but the exit pressure will be too elevated, resulting in a shock wave.

Profile (f) represents a pressure ratio that also results in an isentropic flow. The flow will reach a sonic speed at the throat, however, due to the appropriate pressure ratio it will continue to accelerate in the divergent portion because a supersonic flow accelerates in a divergent channel. The pressure of the flow will also keep decreasing before it reaches its minimal value at the exit of the nozzle.

It is impossible to have another isentropic flow between profiles (c) and (f). Therefore, any other pressure ratio between (c) and (f) will result in the presence of a shock wave, either inside the nozzle as in the case of profile (d) or outside the nozzle as in profiles (e). For profile (d), the back pressure is too high, which causes a shock wave to occur in the divergent portion of the nozzle thus increasing the pressure and consequently decreasing the velocity from sonic at the throat to a subsonic at the exit. From the shock wave on, the pressure will increase to reach the back pressure at the exit of the nozzle. The same situation occurs for profile (e) with the exception that the shock wave occurs at the exit of the nozzle. The back pressure is higher; therefore, there are compression waves at the exit of the nozzle to reduce the pressure of the flow. As for profile (g), the back pressure is lower than the pressure needed for an isentropic solution: therefore, the shock wave will occur at the exit of the nozzle. Since the back pressure is lower, there will be reflected and expansion waves to bring the flow to the back pressure. The flow inside the nozzle is isentropic for both profiles (e) and (g).

When designing a nozzle, isentropic solutions are sought since they do not include energy losses due to irreversible nature of shock waves. The stagnation to exit pressure ratio is ultimately responsible for the presence or lack of shock waves.

3.1.6.1 Shock Waves in the CGDS Process

A shock wave will be formed at the front of the substrate if the flow exiting the nozzle is still supersonic. When the high-velocity flow impinges the substrate, a shock wave will occur. Figure 3-10 shows the occurrence of a shock wave in front of the substrate during the CGDS process due to the supersonic nature of the flow. The incoming supersonic flow will not adapt gradually to the presence of the substrate, rather it will undergo an abrupt change to adapt, as illustrated by Figure 3-10. The shock wave in front of the substrate might reduce the velocity of the particles traveling in the flow.

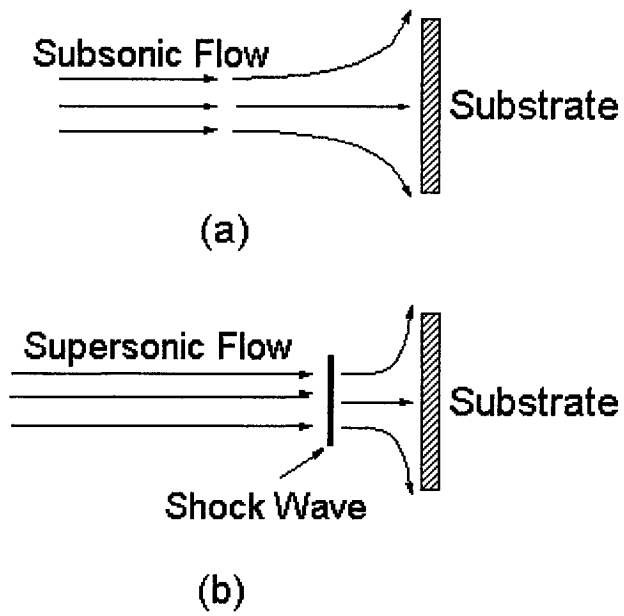

Figure 3-10: Flow over a substrate for (a) subsonic velocity and (b) supersonic velocity

3.1.7 Boundary Layer Development and Displacement Thickness

The flow inside the converging-diverging nozzle will be affected by the development of a boundary layer. The boundary layer is a very thin region of the flow near a wall where the viscous effects are not negligible. The thickness of the boundary layer will increase as the flow travels downstream. The boundary layer thickness is commonly approximated as the thickness in which the flow has a velocity below 99% of the free stream velocity, which is illustrated in Figure 3-11.

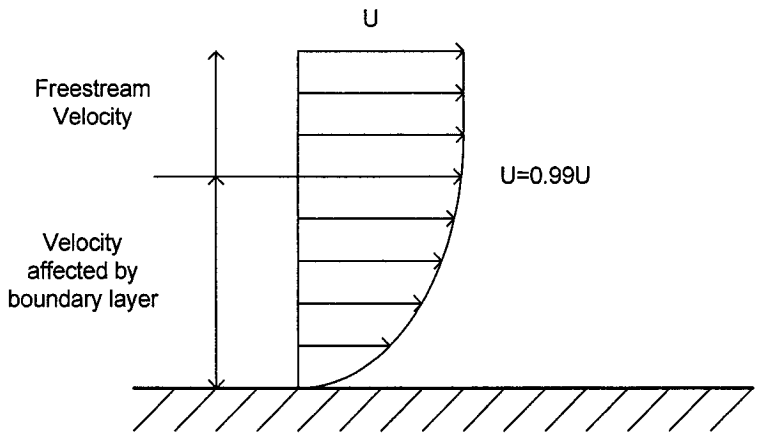

Figure 3-11: Velocity profile over a flat plate

The development of a boundary layer inside the nozzle will also influence the velocity of the fluid exiting the nozzle. The one-dimensional approximation, previously deemed appropriate, does not take into account the development of a boundary layer. In order to obtain a more accurate solution to the nozzle flow, the influence of the boundary layer must be considered. Again, assumptions are introduced to facilitate the boundary layer calculation. It was assumed, since the nozzle is circular, the flow was axisymmetrical, that the maximum value for each parameter, such as the axial velocity

and the density, is on the central axis of the nozzle and that the boundary layer was negligible at the throat of the nozzle due the discontinuity in the geometry and because the boundary layer in the converging portion of the nozzle will not affect the exit properties. The boundary layer in the converging portion of the nozzle is negligible due to the lower velocity of the flow in that portion of the nozzle. Since the flow is assumed to be one-dimensional, the radial velocity profiles in the nozzle can be used to calculate the boundary layer thickness at specific locations.

Another important parameter associated to the viscous effects near the walls is the displacement thickness. It is defined as the distance that the outer flow streamline are displaced due to the boundary layer; or, in a more practical sense, as the increased thickness of wall, δ^*, as illustrated in Figure 3-12, due to the boundary layer.

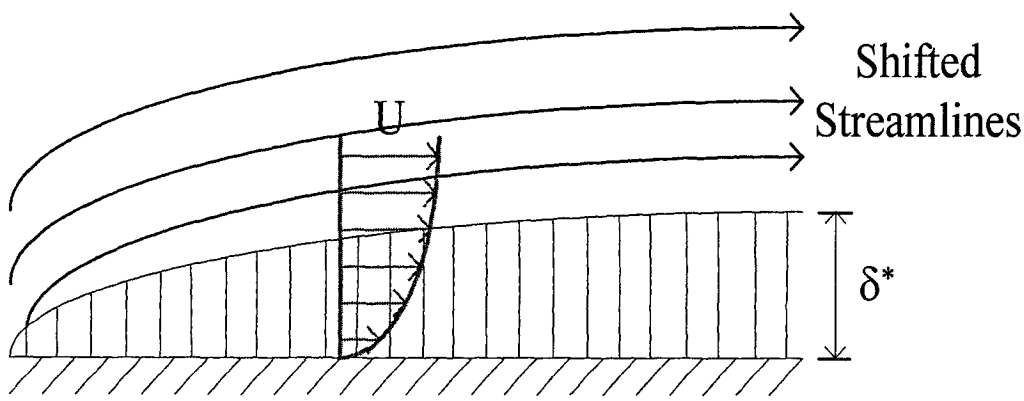

Figure 3-12: Effect of displacement thickness, δ^* on streamlines

Starting from a mass balance, it is possible to derive the following expression for the displacement thickness:

(3-19) $$\delta^* = \int_0^{\delta} \left(1 - \frac{\rho(r)u(r)}{\rho_a u_a}\right) dr$$

where

- $\rho(r)$ is the radial density profile, which is important since the driving gas is compressible;
- $u(r)$ is the radial velocity profile;
- ρ_a is the density value on the nozzle centre line; and,
- u_a is the velocity value on the nozzle centre line.

Once the displacement thickness is calculated, the real nozzle exit diameter, d_r, can be evaluated, as follows (Figure 3-13):

(3-20) $$d_r = d_e - 2\delta^*$$

where d_e is the exit diameter used for the design process.

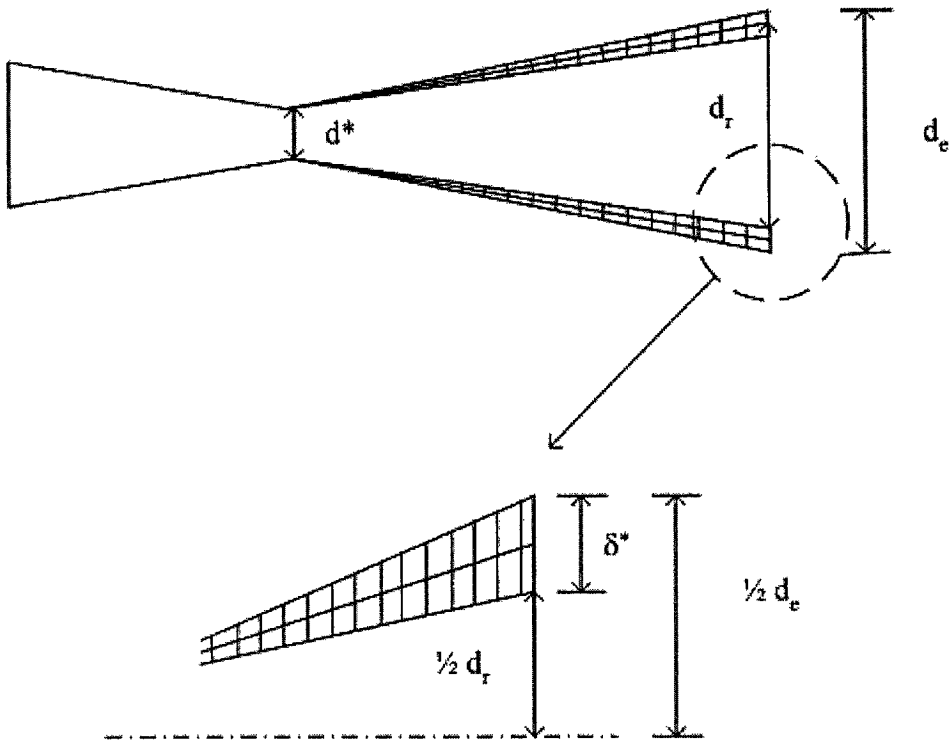

Figure 3-13: Nozzle diameter taking boundary layer into account

As seen from equation (3-20), the difference between the geometric diameter and the displacement thickness value gives the actual diameter with a fully developed flow. With the real diameter value, a new area ratio can be calculated and the actual exit Mach number can be calculated. It is important to note that the boundary layer and the displacement layer do not influence the mass flow of the nozzle since it is assumed that the boundary layer at the throat of the nozzle is of negligible thickness.

3.2 Aluminium Mechanics in the Formation of CGDS Coatings

The type of particle and substrate material influences the coating formation because of their individual mechanical properties. In the following sections, microstructure-, mechanical property-, and deformability- related concepts will be discussed as they relate to CGDS coating technology. General engineering materials concepts will be provided; however, the emphasis will be placed on conventional and nanocrystalline aluminium alloys.

3.2.1 Metallic Microstructure

The materials used in the CGDS process performed in this work are all metallic materials. The following section will discuss the crystalline structure of metallic materials, dislocations and their role in material deformability, and the difference between the conventional and the nanocrystalline materials used in this study.

3.2.1.1 Crystalline Structure

The material properties depend not only on the chemical composition of the material but also on its microstructure. Metals are held together by metallic atomic bonds. Metallic bonds are formed of an ion core and a sea of valence electrons which are not bound to any particular atom. The valence electrons can travel in a relatively free manner in the metal which results in the metallic bond being non-directional. Figure 3-14 illustrates the sea of valence electrons and the ion core found in a metallic bond.

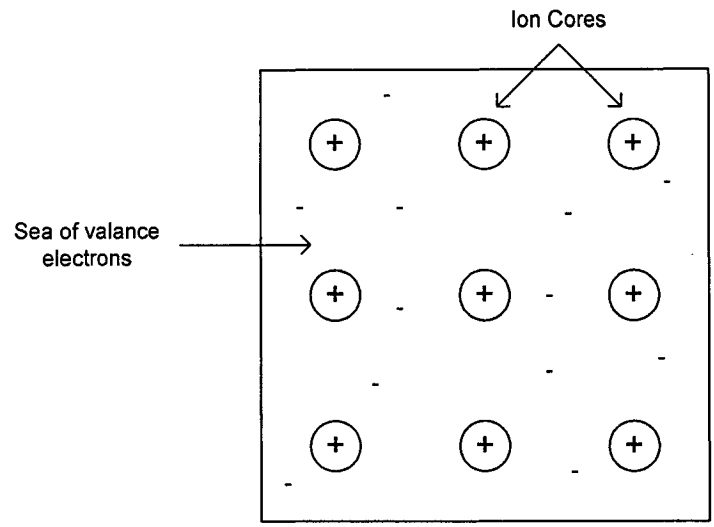

Figure 3-14: Metallic bond

There are different types of microstructure; the focus of the following discussion will be on crystalline materials, which possess a repeating orderly structure. The three main metallic crystalline structures are face-centered-cubic (fcc), body-centered-cubic (bcc) and hexagonal-close-packed (hcp). The present work focuses on the fcc aluminium structure illustrated in Figure 3-15. In an fcc crystalline structure, there are 4 atoms in total in the unit cell. The aluminium unit cell has a lattice length of 0.4049 nm and each atom has a volume of 0.1377 nm^3 [53].

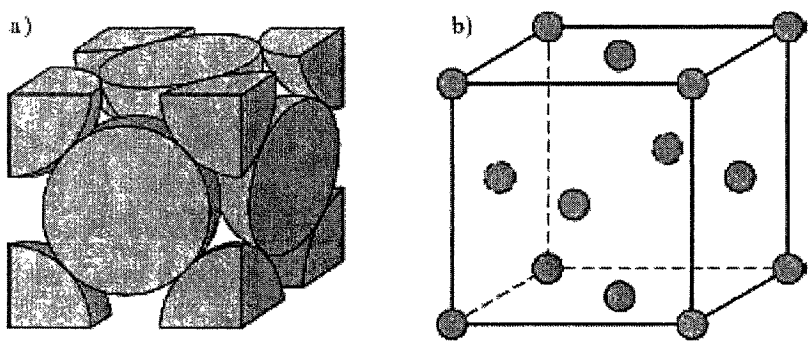

Figure 3-15: Face-centered crystalline structure [26]

There are a number of other important concepts which will be useful when discussing the deformation of materials that can be illustrated using the crystalline structure. The atomic packing factor (APF) represents the number of atoms in a primitive unit cell, as is illustrated in Figure 3-15. The APF is equal to the ratio between the total volume of all the atoms found in the primitive cell over volume of the primitive cell cube. A lower APF result in more voids, hence more areas where the atoms can lodge, making it more difficult for them to move. The crystallographic direction and plane are two other important parameters derived from the crystalline structure. The direction, as shown in Figure 3-16 is a vector between two points. The slip direction corresponds to the direction with the largest atom density. For the FCC structure, the slip directions are the <110> family while the slip planes are the {111} family since these are the directions and planes with the highest atom concentrations [26].

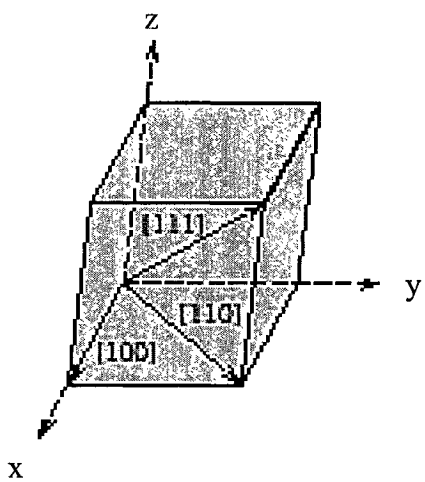

Figure 3-16: Slip direction, (110) is the slip direction for the FCC structure [26].

Similarly, the crystallographic plane, illustrated in Figure 3-17 will determine the direction of slip and deformation.

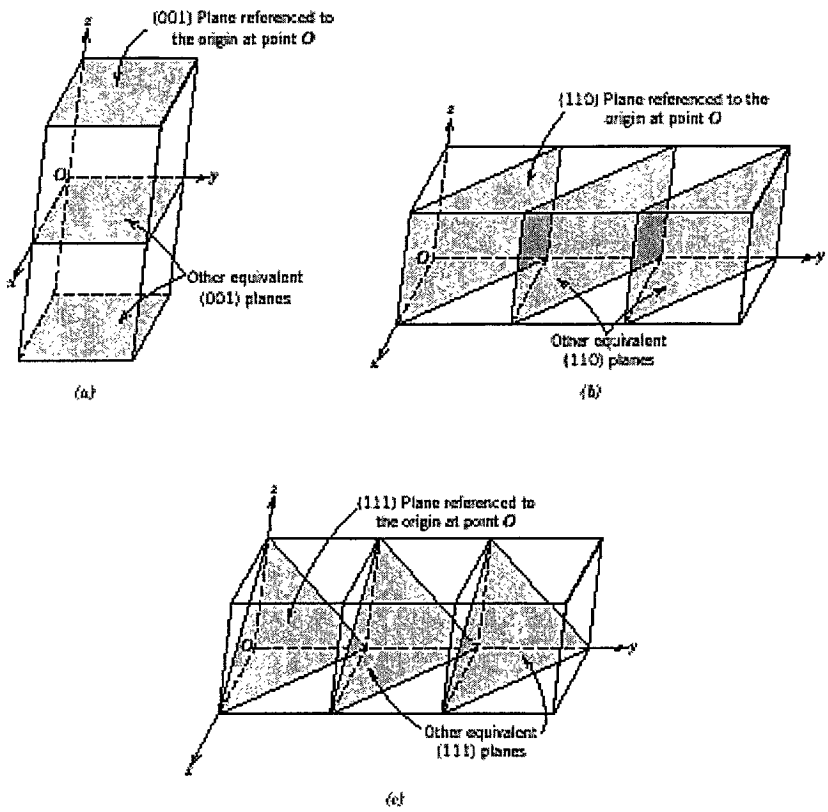

Figure 3-17: Crystallographic plane, (111) being the slip plane for the FCC structure [26].

The combination of the slip direction and the slip plane form the slip system, which depends on the crystalline structure of the material.

3.2.1.2 Dislocations

Deformation due to plastic strains in materials occurs because of the presence of dislocations. A dislocation represents an irregularity in the crystalline structure. There are three possible types of dislocations: a line dislocation, a screw dislocation and a mixed dislocation, all three are illustrated in Figure 3-18. The motion of dislocations, which will be discussed subsequently, will be concentrated in the slip system because it will result in

the least amount of atomic distortion. The most common way of defining a dislocation is the use of the burgers' circuit [54] which represents any atom to atom path taken in a metal where a dislocation can be found. With the dislocation, the circuit will not form a closed loop and the burgers vector represents the vector needed to close the loop. In a line dislocation, the burgers vector will be normal to the line of dislocation while, in a screw dislocation, it will be parallel to the line of dislocation.

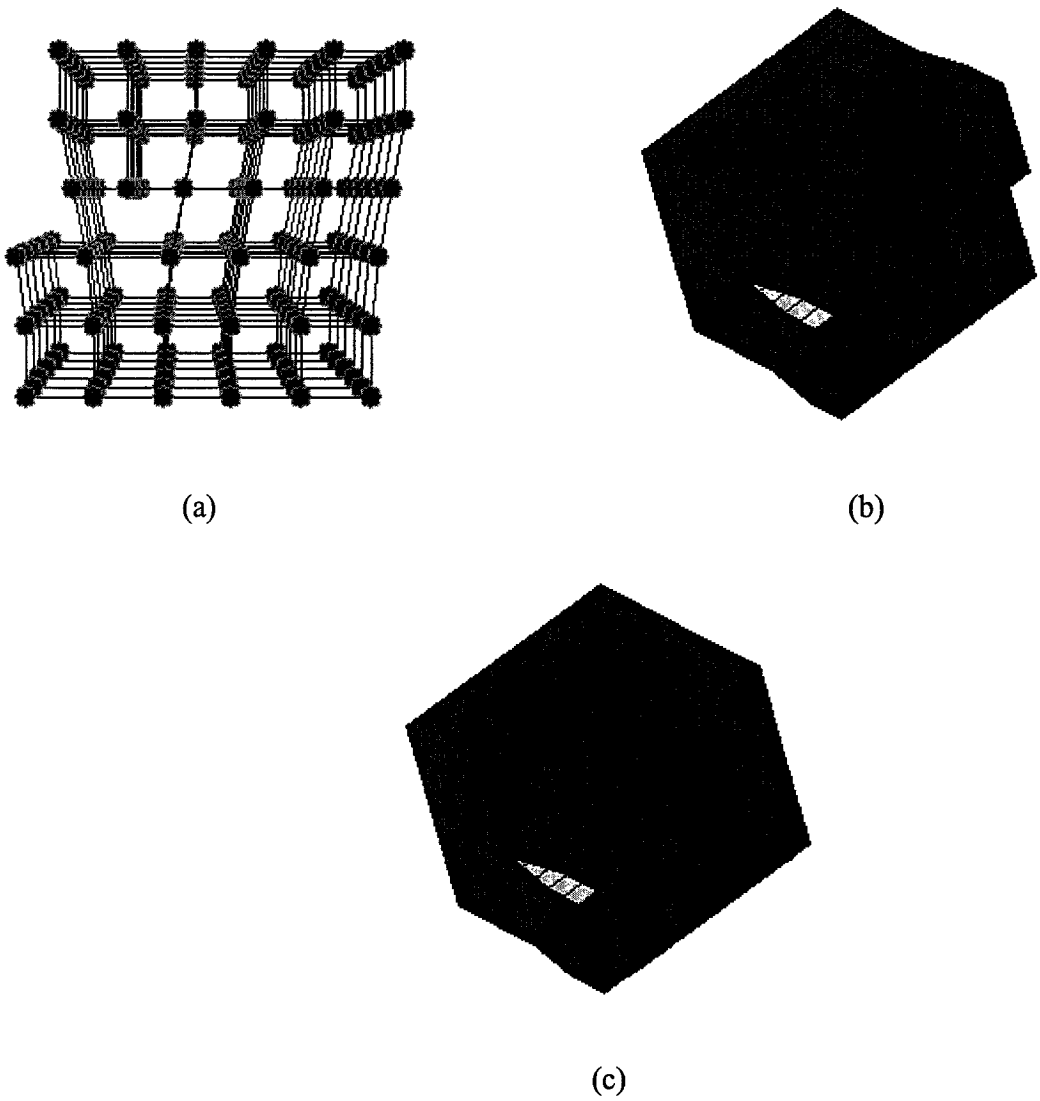

Figure 3-18: Possible types of dislocation (a) line; (b) screw, (c) mixed [26]

The motion of these dislocations causes the deformation of the material. In an fcc-structures material, the dislocations are found on the most closely packed atomic planes. The dislocations in FCC metals will usually be the result of an extra atomic plane in the (110) direction [54]. The dislocation movement in the aluminium will influence the material properties, which will be discussed in a future section.

3.2.1.3 Conventional and nanocrystalline material

Conventionally structured crystalline materials as well as nanocrystalline crystalline materials are used in this work. Conventionally structured materials have a repeating crystal lattice with a grain size in the order of microns while nanocrystalline materials have a grain size in the order of nanometres. The principal difference in the material properties between the two results from the difference in the grain size. A smaller grain size will produce a greater amount of grain boundaries which are known to impede the movement of dislocations. These dislocations are responsible for the plastic deformation of a crystalline material. Hence, the smaller grain size will result in a harder material since there are more grain boundaries to impede dislocation movement. The mechanical properties of aluminium affected by the presence of grain boundaries are reviewed in more detail in the following sections.

3.2.2 Mechanical Properties

The important mechanical properties to consider in the material selection for CGDS spraying, namely the elastic modulus, E, yield strength, σ_y, ductility, hardness, are discussed in the following section. These mechanical properties are important in CGDS for the following reasons. The elastic modulus and the yield strength indicate the energy required for plastic deformation to occur. The ductility shows how much plastic deformation a material can undergo before failure occurs. Finally, the hardness is a good indicator of the ease of deformation.

3.2.2.1 Stress-Strain Behaviour of Aluminium

The stress strain behaviour of typical aluminium is illustrated in Figure 3-19. Two distinct regions are visible in the figure; the first is linear and provides the limits of elastic deformation of the material; the second is the plastic deformation region. The yield point is the physical elastic limit of the material and is the transition point between both regions. The yield point is the maximum possible strain before permanent or plastic deformation. The concept of deformability, critical to the CGDS process for proper coating, will be discussed in greater detail in Section 3.2.2.2.

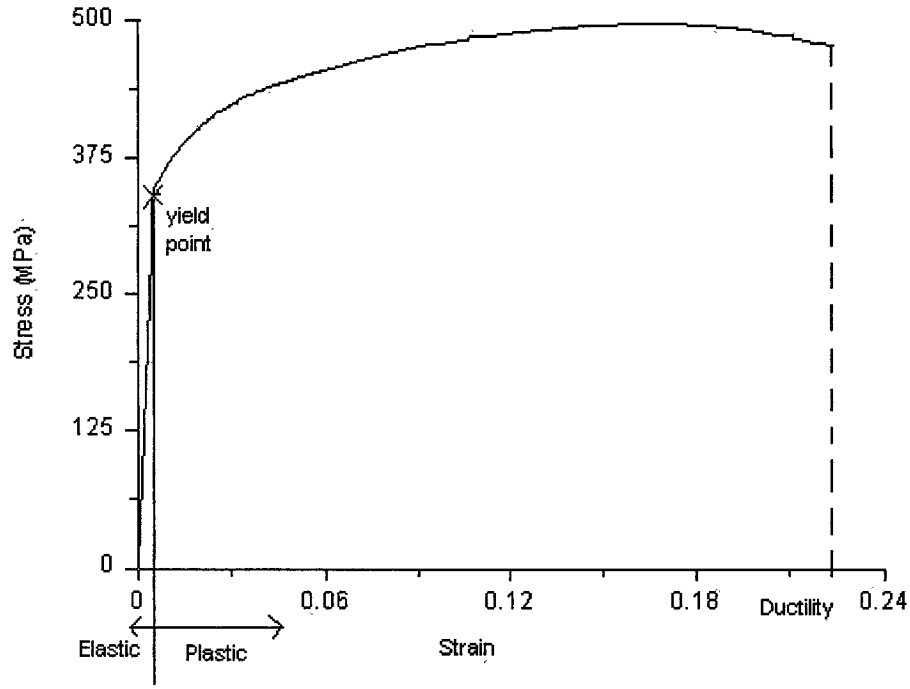

Figure 3-19: Stress-strain curve for 2024-T351 aluminium alloy [26]

The elastic modulus of a material is defined as the magnitude of the elastic deformation as a function of the applied strain, as per equation (3-21). Experimentally, it is the slope of the linear region of the stress-strain diagram. For any given strain located in the elastic region, the stress is evaluated by Hooke's Law:

(3-21) $$\sigma = E\varepsilon$$

where σ represents the stress, E the elastic modulus and ε the strain. It is important to note that the mechanical properties of a material are affected by temperature. The tensile and yield strength will tend to decrease with a temperature increase while the opposite will occur for the ductility, or % elongation, as illustrated in Figure 3-20.

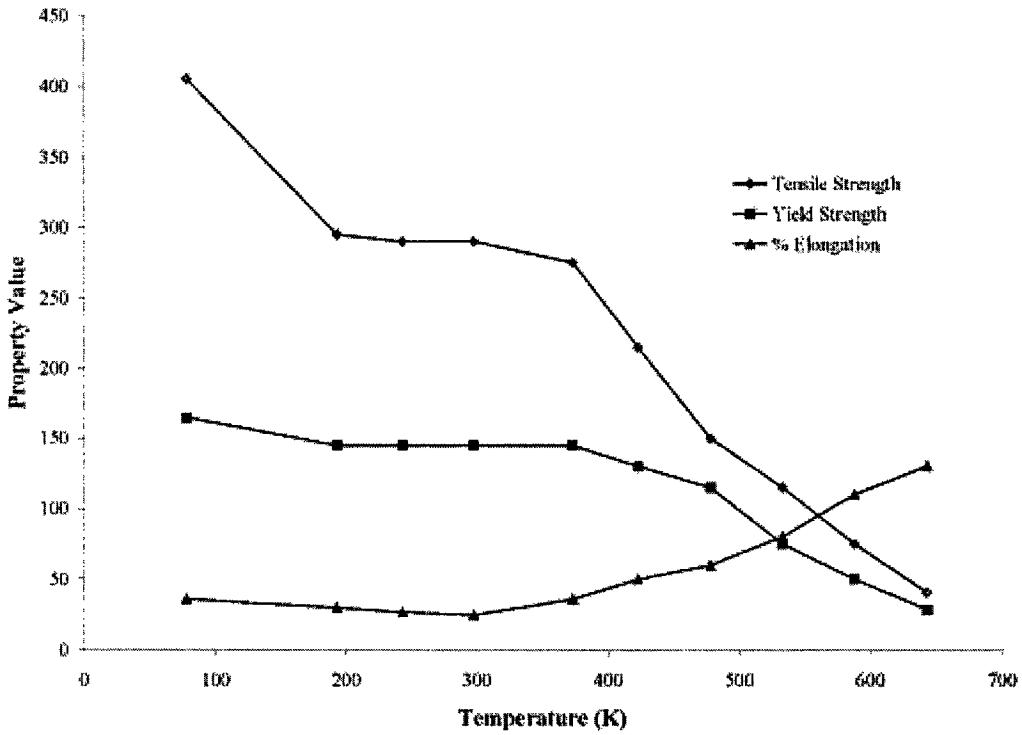

Figure 3-20: Material properties as a function of temperature for aluminium [55]

Ductility of a material is also an important mechanical property. Ductility is the amount of total strain that a material can sustain before failure occurs. A very ductile material will be able to sustain significant plastic deformation before it ruptures while a brittle material will sustain very little plastic deformation before rupturing, as illustrated by Figure 3-21, C and C' represent the ductility of a brittle and a ductile material, respectively. This is very important in CGDS since a number of studies have presented evidence [33, 34, 36] that the adhesion process rests mostly on the elevated plastic deformation undergone by the particle.

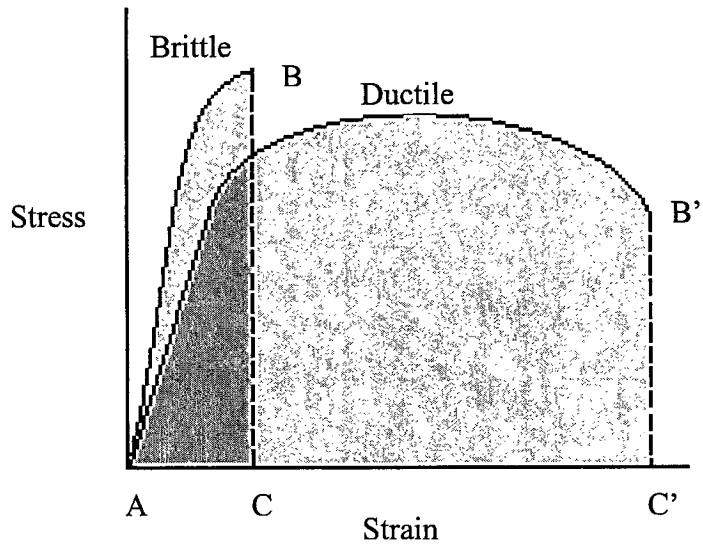

Figure 3-21: Schematic representation of the stress-strain behaviour of brittle and ductile materials [26]

3.2.2.2 Deformation of Aluminium

Plastic deformation of both the aluminium particles and the substrate is thought to be the principal bonding mechanism in CGDS [33, 34, 36]. An example of a stress-strain curve for an aluminium alloy was presented in Figure 3-19. Deformation of a solid material will occur when a sufficient stress is applied to surpass the material yield strength. In CGDS, the stress applied to the substrate and the particles is very high due to the high impact velocity. Therefore, the deformation is plastic and can be observed in both the substrate and the impacting particle as shown by Figure 2-15.

3.2.2.3 Hardness

Hardness is representative of the strength of a material when it is subjected to a localized plastic deformation. The localized plastic deformations can be the result of performing a small indentation on a test specimen. The indentation of a softer material will result in a deeper crevasse. The hardness will be a function of the depth of that crevasse. Hardness tests are often used because they have a relatively low cost, can be done on very small samples without much preparation, and are non-destructive. There are a number of hardness tests: Rockwell, Vickers, Brinell and Knoop. It is important to note that each hardness test uses a different scale and/or testing mechanism. It is possible to relate the different hardness scales. Each test has its advantages and is used for certain types of materials. When dealing with fragile coatings, the Vickers hardness test is the most widely used approach because of the low level of stress applied by the indenter.

The Vickers hardness test uses a diamond square-pyramid shaped indenter. The indenter is forced under a known load and the diagonal of the resulting indentation is measured [56]. The loads used vary between 1 and 1000 g [26] and the Vickers hardness is determined using the following expression:

$$V = P/\left(0.5393d^2\right) \tag{3-22}$$

where V is the Vickers hardness number, P is the imposed load in kg and d is the diagonal of the indentation in millimetres.

The gas dynamics and materials engineering theory covered in this chapter are used to design the CGDS set-up and analyse the coatings produced using it. The design will be done using a computational fluid dynamics model based on the gas dynamics theory outlined in this chapter. The modeling steps and major results obtained are discussed in Chapter 4. The materials engineering theory detailed in this chapter will be used in Chapter 6 to evaluate the coatings produced using CGDS.

4. ANALYTICAL MODEL AND SIMULATIONS

In order to design the CGDS set-up, a model was developed and simulations were performed to determine the appropriate nozzle geometry. In this chapter, the emphasis will be placed on the computational fluid dynamics used to simulate the CGDS process and the initial conditions for modeling, as well as the desired results of the simulation. The available materials for the process will also be discussed as will the final design and modeling results. Finally, the secondary design iteration and modeling will be discussed.

4.1 Computational Fluid Dynamics

Computational fluid dynamics (CFD) is a powerful tool which uses the general governing equations (3-1) to (3-4) in their differential form and manipulates them to obtain algebraic equations that can be solved to characterize the fluid flow.

4.1.1 Overview of CFD Model

The software used for the CFD modeling in the current work was Fluent©, which simultaneously solves the energy equation, the linear momentum equation and the continuity equation. All of the above equations express the conservation of a state variable. Since the quantities are conserved, they can be expressed in a differential form as a function of the other influencing factors to form a balance. Each equation represents the conservation of a state variable; for example, in the linear momentum equation, the dependent variable is the momentum. The energy equation expresses the energy balance for the system while the continuity expresses the conservation of mass. Fluent© uses a control volume method which defines a number of non-overlapping control volumes

throughout the domain in such a way that each grid point is surrounded by a control volume. For each control volume, the governing equations are integrated. Discretized equations are derived and then solved iteratively.

The governing equations can be derived from a general differential equation that has the following form [57]:

$$\frac{\partial}{\partial t}(\rho\phi) + div(\rho u \phi) = div(\Gamma\, grad\phi) + S \tag{4-1}$$

where ρ is the density, u is the velocity, ϕ is the dependent variable, Γ is the diffusion coefficient and S is the source term. The diffusion coefficient and the source terms are function of the chosen dependent variable (i.e. $S(\phi)$, $\Gamma(\phi)$). Discretized forms of the governing equations are derived from equation (4-1).

Since a control volume formulation is used, the grid can be defined as seen in Figure 4-1, where P is the grid point where the value is calculated, N, S, E, and W are the northern, southern, eastern and western neighbouring points, respectively. The same under case letters (n, s, e, and w) represent the faces of the control volume while the Δ_i are the distance between the faces and the δ_i are the distances between each grid point.

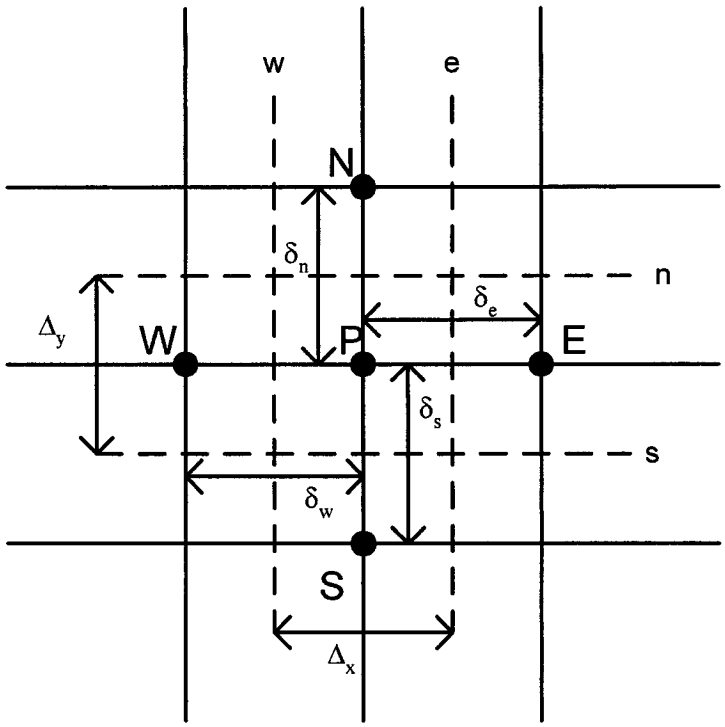

Figure 4-1 : Two-Dimensional Discretization Scheme (assuming unit depth).

The value of the dependent variable at each node is expressed as a function of its neighbours. For the two-dimensional situation represented in Figure 4-1, the dependent variable at point P can be expressed as follows:

$$
\begin{aligned}
& a_P\phi_P = a_E\phi_E + a_W\phi_W + a_N\phi_N + a_S\phi_S + b \\
& b = S_C\Delta x\Delta y + a_P^0 T_P^0 \\
& a_P^0 = \frac{\rho S_c \Delta x\Delta y}{\Delta t} \\
& a_P = a_E + a_W + a_N + a_S + a_P^0 - S_P\Delta x\Delta y
\end{aligned}
\qquad \textbf{(4-2)}
$$

where the a_i are the equation specific coefficients of the variables after the discretization, a_P^0 is the coefficient due to the unsteady nature of the problem, T_p^0 is the temperature at time t-Δt if the system is unstable, S_C and S_P are the source term coefficients and $\Delta x\Delta y$ is the volume of each control volume, if assuming a unit depth.

The computational scheme used in Fluent© is an upwind technique in which the dependent variable value at the control volume interface is assumed to be equal to its value at the next grid point located upwind of the interface. The upwind scheme is used because it follows the proper flow of information throughout the flow field by following the flow direction [58]. A first order upwind technique uses an average value of the variables for the center value. This average value is valid for the entire cell. A second order upwind technique is more accurate when calculating the value of the variable across the faces of the volume. The second order upwind technique uses a Taylor series expansion of the solution at the center of the volume. This reduces the error of the scheme by one order and makes the solution more precise but harder to converge.

4.1.2 CFD Model Presets and Boundary Conditions

In setting up the CFD problem for the CGDS, a number of computational settings had to be determined. An implicit coupled solver, which solves the governing equations simultaneously, was used since it is recommended for high velocity flows [59]. Other scalar equations involved in the problem, such as the turbulence equation are solved subsequently. The unknown value in the problem is computed using both known and unknown values from the neighbouring cells, which results in the possibility that there can be more than one unknown value in each equation.

As part of the computational model, the chosen turbulence model was the k-ε turbulent model since it is the simpler model that takes flow turbulence into account and

is widely used for modeling purposes [59]. In the k-ε turbulent model, two equations are solved independently: one for the turbulent kinetic energy, k, and one for the turbulent kinetic energy dissipation, ε. The turbulent kinetic energy is the energy due to the turbulence-induced motion of the fluid. The dissipation rate is the rate at which the turbulent kinetic energy is absorbed due to the viscosity of the fluid. The equations are as follows:

$$\rho\frac{Dk}{Dt}=\frac{\partial}{\partial x_i}\left[\left(\mu+\frac{\mu_t}{\sigma_k}\right)\frac{\partial k}{\partial x_i}\right]+G_k+G_b-\rho e-Y_M$$

$$\rho\frac{D\varepsilon}{Dt}=\frac{\partial}{\partial x_i}\left[\left(\mu+\frac{\mu_t}{\sigma_k}\right)\frac{\partial \varepsilon}{\partial x_i}\right]+C_{1\varepsilon}\frac{\varepsilon}{k}\left(G_k+C_{3\varepsilon}G_b\right)-C_{2\varepsilon}\rho\frac{\varepsilon^2}{k} \quad \text{(4-3)}$$

where G_k is the generation of turbulent kinetic energy due to the mean velocity gradients, G_b is the generation of turbulent kinetic energy due to buoyancy, Y_M represents the contribution of the fluctuating dilatation in compressible turbulence to the overall dissipation rate, $C_{1\varepsilon}$, $C_{2\varepsilon}$, $C_{3\varepsilon}$ are empirical constants and σ_k and σ_ε are the turbulent Prandlt numbers for the turbulent kinetic energy and its dissipation rate respectively [59].

The boundary conditions used for the model are shown on the CFD meshes in Appendix 1. The inlet of the nozzle was set up as a pressure inlet while the outlet was set as a pressure outlet. A wall boundary condition was used to represent the wall of the nozzle while an axis boundary condition was used where the centreline of the nozzle is located.

4.2 CGDS Design Considerations

The goal of the modeling process and of the thesis was to obtain a converging-diverging nozzle geometry in which injected aluminium particles with a 20 μm diameter would reach an exit velocity greater than 900 m/s before they impacted on an aluminium substrate located downstream of the nozzle exit. The first step in the design was to use the one-dimensional nozzle analysis outlined in Section 3.1.4. In order to design an optimal CGDS set-up, a number of initial and boundary conditions were specified. Physical and equipment constraints influenced the nozzle design as did the available materials for driving gas, powder and substrate. The desired particle exit velocity was determined using the deposition efficiency values available in literature [17, 20]. The inlet pressure for the converging-diverging nozzle used baseline values provided in the literature [17, 19, 24] as a guideline.

4.2.1 Physical and Equipment Restraints

A number of constraints restrained the design of the cold spray nozzle. First and foremost, the available powder feeder which was used to inject the particles into the driving gas flow had a maximum operating pressure of 700 kPa. This limited the pressure at the injection site to 700 kPa which is low when compared to other injection pressures used in the literature [17]. Due to this physical restraint, two design options were possible: to either place an axial injection site of 700 kPa at the inlet of the converging-diverging nozzle; or, a radial injection could be placed downstream from the nozzle inlet at the position in the nozzle where the pressure would have decreased to 700 kPa. The

radial injection does present some challenges and has previously been deemed less efficient than axial injection [44] although it has never been reported to be successful in spraying particles using CGDS.

Another constraint added to the design was due to concerns with the mass flow rate. As cited by previous works [17], helium is often used in CGDS to obtain high driving gas and particle velocities due to its lower molecular weight and higher specific ratio than air. The lower molecular weight and higher specific ratio result in a higher velocity for the same Mach number. The major disadvantage of using helium is the high cost involved when compared to air; however the higher possible velocities for the same Mach number is an advantage that outweighs the cost disadvantage. Therefore, the mass flow rate had to be kept to a minimum in order to reduce the costs. This was achieved by reducing the throat diameter and by maintaining the diverging angle, α, as defined in Figure 4-2, at 0.32° using the following equation:

$$\alpha = tg^{-1}\left(\frac{\frac{d_e - d_t}{2}}{L_{div}}\right) \tag{4-4}$$

For all design cases, the diverging angle was kept constant while the diverging length was increased, which had been previously reported to increase particle velocity [19].

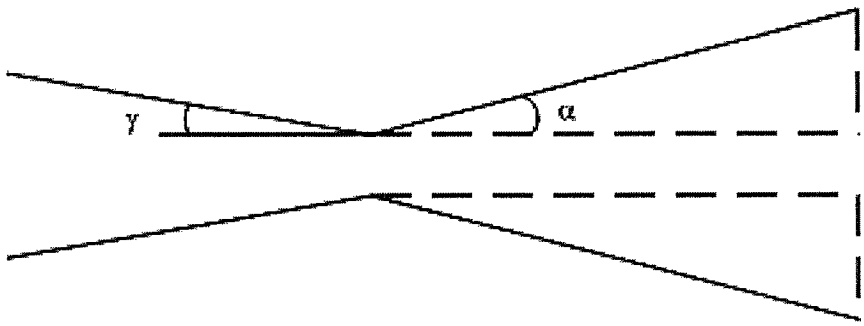

Figure 4-2 : Converging-diverging nozzle converging and diverging angle

Finally, a third constraint is associated to using electrical-discharge machining (EDM) to manufacture the relatively small diameter conical internal shape of the nozzle. Any amount of improper offset could irreversibly damage the nozzle; therefore, a maximum converging angle, γ. (Figure 4-2) was set to provide realistic production tolerances. This was possible since the inlet to throat area ratio has little influence on the exit velocity.

4.2.2 Available Materials (driving gas, substrate and particles)

The critical materials in the CGDS process are the driving gas, the substrate, and feedstock powders. Prior to the CGDS design phase, each of these materials had been selected. As aforementioned, the chosen driving gas was helium since it produces a higher velocity for the same Mach number. The substrate was aluminium in order to reproduce the industrial situation where it is often used as corrosion protection (see Section 2.1.1). Finally, there are two types of available powders: conventional and nanocrystalline aluminium 5083 powders. This aluminium alloy is often used in marine environments since it has a high corrosion resistance as well as high yield strength. In Al

5083, magnesium is the principal alloying element. This type of alloy is also useful in low temperatures environments but its properties will decrease rapidly when heated to temperatures above 100°C [60].

The aluminium particles were manufactured with two different processes. The conventional particles are manufactured using atomization. In the atomization process [61], the particles are formed from a plasma jet of metal. The stream is broken up by jets of water which create the particles. The SEM of the conventional particles is included in Figure 4-3. The SEM shows the spherical form of the conventionally structured particles as well as their average size which is below the 20 μm used in the initial modeling. The average diameter size as taken from this SEM is approximately 10 μm and the surface of the particles seems smooth.

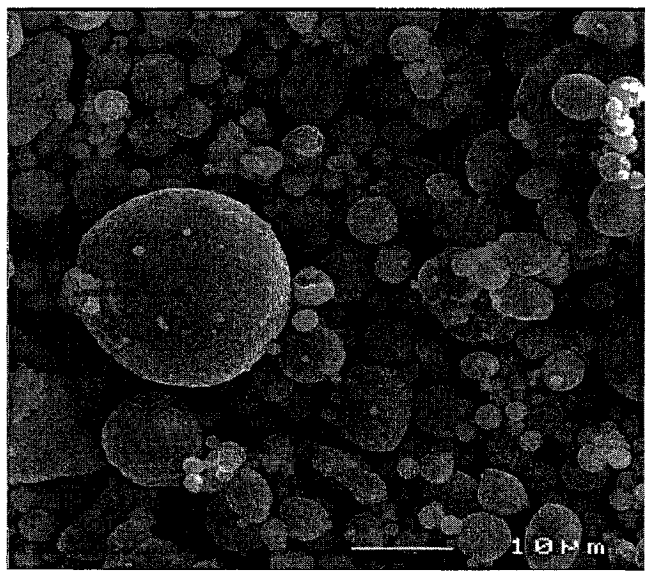

Figure 4-3: SEM of conventional aluminium 5083

Nanocrystalline aluminium powders were formed using cryomilling, a top-down method which entails that a larger grain size is reduced considerably; in this case to a nanoscale as opposed to the usual microscale. The process used to form the non-equilibrium nanocrystalline particles is a solid-state technique were the particles are welded, fractured and re-welded by a high-energy ball mill [62]. Nanostructured particles develop more easily at lower temperature [62]. During the cryomilling process, milling is performed using a liquid nitrogen medium [63]. The formation of the nanoscale microstructure is due the high deformation rate which creates shear bands where the dislocations accumulate. When a critical level of dislocation density is reached, the material becomes heavily strained and the crystal disintegrates into nanoscale subgrains [62]. Cryomilling will produce non-spherical particles, as seen in Figure 4-4. In the case of nanocrystalline particles, the grain boundaries or interfaces can form up to 50% of the volume [64]. The nanocrystalline powders, manufactured at the University of California at Davis, have an agglomerated form and an average diameter between 20 and 40 μm. Their shape is non-spherical and their surface is rough. The particles also have a wider array of sizes when compared to the conventionally structured ones.

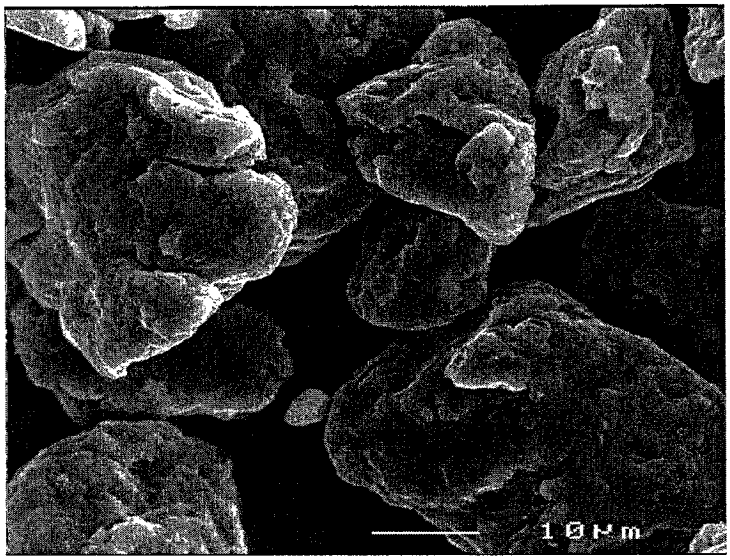

Figure 4-4: SEM of nanocrystalline aluminium 5083 particles

4.2.3 Driving Gas Mass Flow Rate

The final parameter considered to optimize the design is the driving gas mass flow rate. As stated previously, the driving gas flow rate must be minimal in order to minimize the costs. Two approaches can be taken. The first is to change the stagnation (or inlet) pressure and the second is to decrease the throat diameter. The reduction of stagnation pressure requires less helium but might affect the exit particle velocity. The decrease in throat diameter limits the amount of gas that can travel through the nozzle when the flow is choked. The investigation performed to determine the nozzle geometry is discussed in the following section.

4.3 Modeling-Based Design Process

As stated previously, the initial modeling was done to obtain a nozzle geometry that would produce particle exit velocity above 900 m/s. A converging section length of 30 mm was arbitrarily selected prior to the design process. The main geometric and

physical parameters that were varied are the diverging length, exit diameter, throat diameter and stagnation (inlet) pressure. Subsequently, the nozzle geometry, initially optimized for 20 μm diameter particles, was modeled using other particle diameters. The preliminary design was concerned with the length of the diverging portion of the nozzle, since it is important in the acceleration of the particles.

4.3.1 Preliminary Design: Diverging Length Selection

The first parameter that was varied during the preliminary design was the diverging length of the nozzle. Some of the parameters, such as the inlet pressure to outlet pressure ratio and the throat to exit area ratio were pre-determined using a one-dimensional gas dynamics analysis (Appendix 2). These were calculated based on the desired exit Mach number of approximately 3 since it has been reported that Mach 3 is the upper boundary for the Mach number interval in CGDS [24]. The throat diameter was initially set to 3 mm using published results as a guideline [17]. The outlet pressure was assumed to be equal to the atmospheric pressure since the nozzle was to exit into the spray chamber where there was no pressure modifying device. Six different diverging lengths were modeled, from 180 mm to 270 mm, to obtain a satisfactory particle velocity at the nozzle exit. The exit diameter was initially set to 6 mm to obtain a throat to exit cross-sectional area ratio of 4 which is associated with an exit Mach number of approximately 3.45. Using that Mach number, and the pressure ratio equation, the required stagnation pressure to obtain an atmospheric pressure at the exit was approximately 5900 kPa, which would require an excessive amount of helium and would not be cost efficient. Thus, for modeling purposes, the stagnation pressure was lowered in

hopes that it would not have an adverse effect on the driving gas velocity. To determine if the variation in inlet pressure had an effect on the particle exit velocity, the inlet pressure was varied from 900 kPa to 2MPa. CFD generated pressure profiles produced for various test conditions, as shown by Figure 4-5, were used to determine the best injection position configuration. The axial position where the pressure had decreased to 700 kPa was located and the injection simulations were performed at that site.

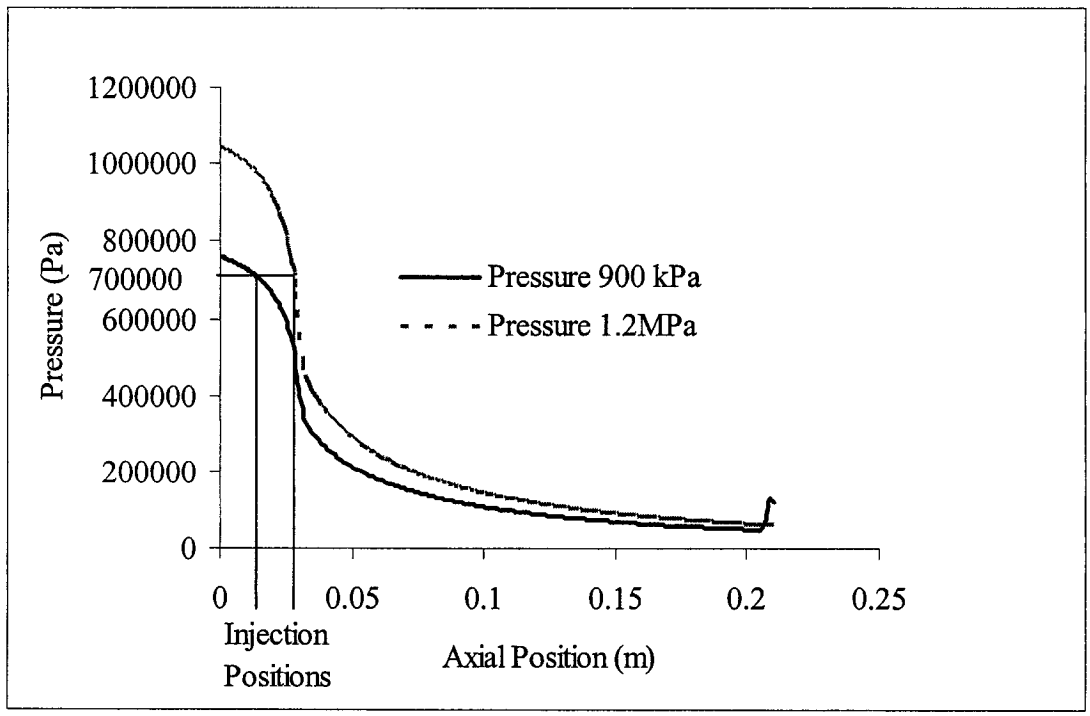

Figure 4-5: CFD-generated pressure profile used to determine injection location

The exit velocities for the 20 μm aluminium particles predicted using a nozzle exit diameter of 6 mm were insufficient, as seen in Table 4-1, to produce an adequate deposition efficiency. The increase in length was not as effective in producing higher particle velocity; therefore, a 25% increase in the exit diameter was chosen as a means of

increasing the exit particle velocity. With this increase, it was hoped that the effect of the boundary layer and displacement thickness might be less important and that the throat to exit area ratio would be closer to the one-dimensional value.

Table 4-1: Particle velocity at nozzle exit for a throat diameter of 3 mm

Divergent Nozzle Length (mm)	Outlet Diameter (mm)	Inlet Pressure (kPa)	Particle Velocity at the exit (m/s)
180	6.0	700	841
180	6.0	900	861
180	6.0	1600	865
180	6.0	2000	869
200	6.0	700	788
200	6.0	1200	843
200	6.0	1600	843
230	6.0	700	800
230	6.0	1200	856
230	6.0	1600	859
230	7.3	1600	880
250	7.3	1600	893
260	7.3	1600	898
270	7.3	1600	912

Following these trials (Table 4-1), the diverging length was set at 270 mm which produced a total nozzle length of 300 mm. This diverging length was chosen because the simulated particle exit velocity was above the initial requirement and the particle injection was not done at the throat itself but slightly downstream from it. The mass flow rate restriction, outlined in Section 4.2.1, forced a change in geometry, namely the throat diameter, which was one of the solutions initially envisioned as a way to reduce mass flow rate in the nozzle.

4.3.2 Preliminary Design: Throat Diameter and Stagnation Pressure Selection

As discussed in Section 4.2.1, the throat diameter is the main variable which controls the mass flow rate. In order to reduce the mass flow rate, the throat diameter was decreased. This was done while the diverging angle (Figure 4-2) was kept constant. The throat diameter was reduced from 3 mm to 2.6, 2.2 and 2 mm. The diverging length was kept constant since it is critical to provide the particles sufficient time to reach the driving gas velocity. The exit diameter was concurrently altered to keep the diverging angle constant. Table 4-2 contains the particle velocity and mass flow rate findings at different throat diameters.

Table 4-2: Particle velocity and mass flow rate for different throat diameters for a diverging length of 270 mm

Throat Diameter (mm)	Exit Diameter (mm)	Inlet Pressure (MPa)	Injection Position (mm)	Particle Velocity (m/s)	Mass Flow (kg/s)
2.6	6.9	1.6	31	913	0.00724
2.2	6.5	1.6	31	905	0.00520
2	6.3	1.6	31	896	0.00530
2	6.3	1.7	32	904	0.00459
2	6.3	1.7	35	895	0.00459
2	**6.3**	**2.0**	**35**	**918**	**0.00546**
2	**6.3**	**2.0**	**40**	**904**	**0.00546**

A nozzle with a throat area of 2 mm was selected. The bolded rows in Table 4-2 indicate the selected exit diameter and inlet pressure for two different injection positions. The inlet pressure, or the stagnation pressure, was also varied to determine the effect on exit particle velocity; the stagnation pressure producing the highest velocity will be selected. Figure 4-6 contains the pressure distribution for different stagnation pressures.

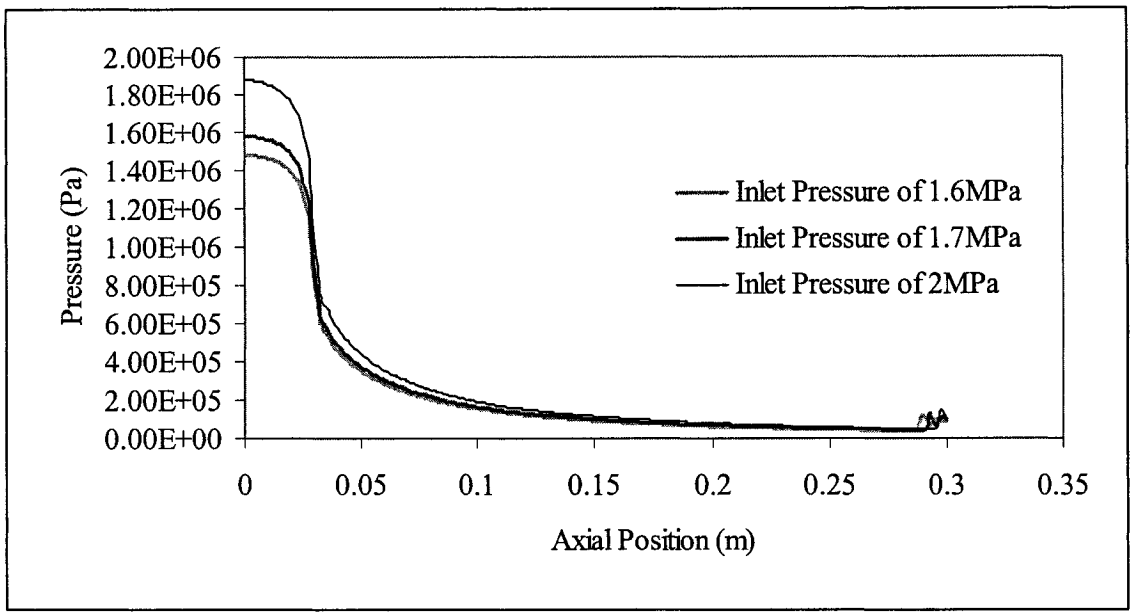

Figure 4-6: Pressure distribution inside converging-diverging nozzle for a throat diameter of 2 mm

There is a shock wave present with all three cases modeled. The position of the shock in the diverging portion occurs further downstream as the stagnation pressure is increased (i.e. the shock is closest to the nozzle exit for the highest stagnation pressure). The effect of the shock wave on the particles was not enough to decrease their velocity below the desired minimum therefore the design was acceptable even if one was present.

The effect of the boundary layer was also considered during these preliminary modeling trials by studying the velocity profile across a vertical cross-section at the exit of the nozzle, as seen in

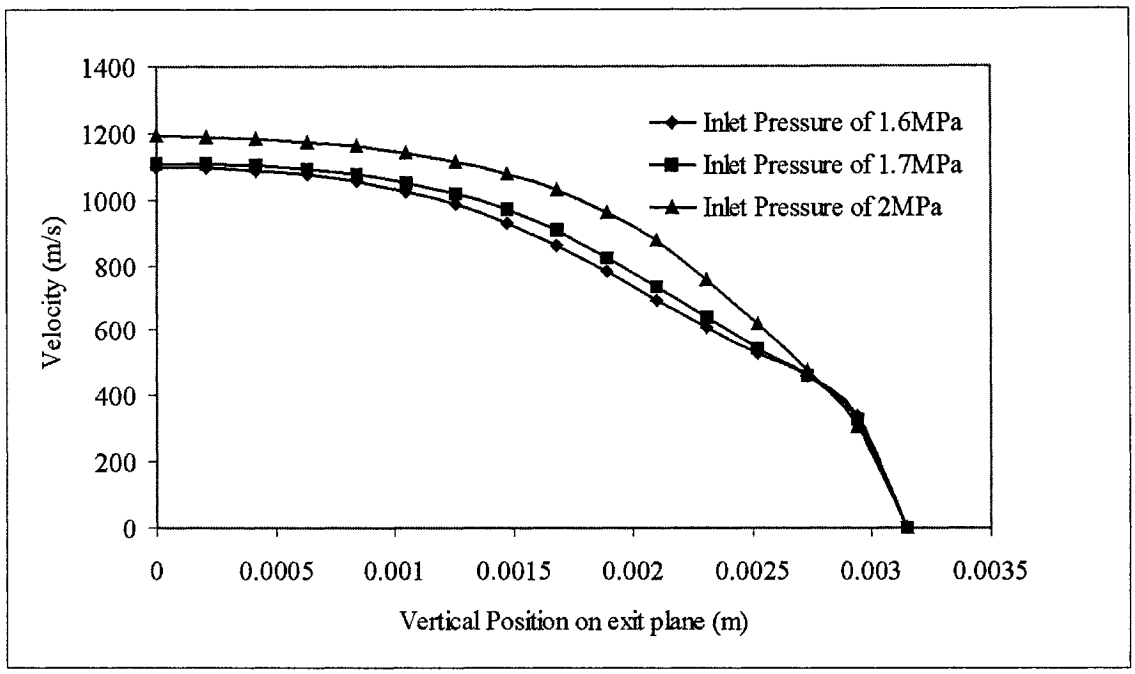

Figure 4-7. The exit velocity profile shows that a significant portion of the flow has an exit velocity above 900 m/s, which was the lower threshold set for acceptable velocity at the beginning of the preliminary design phase.

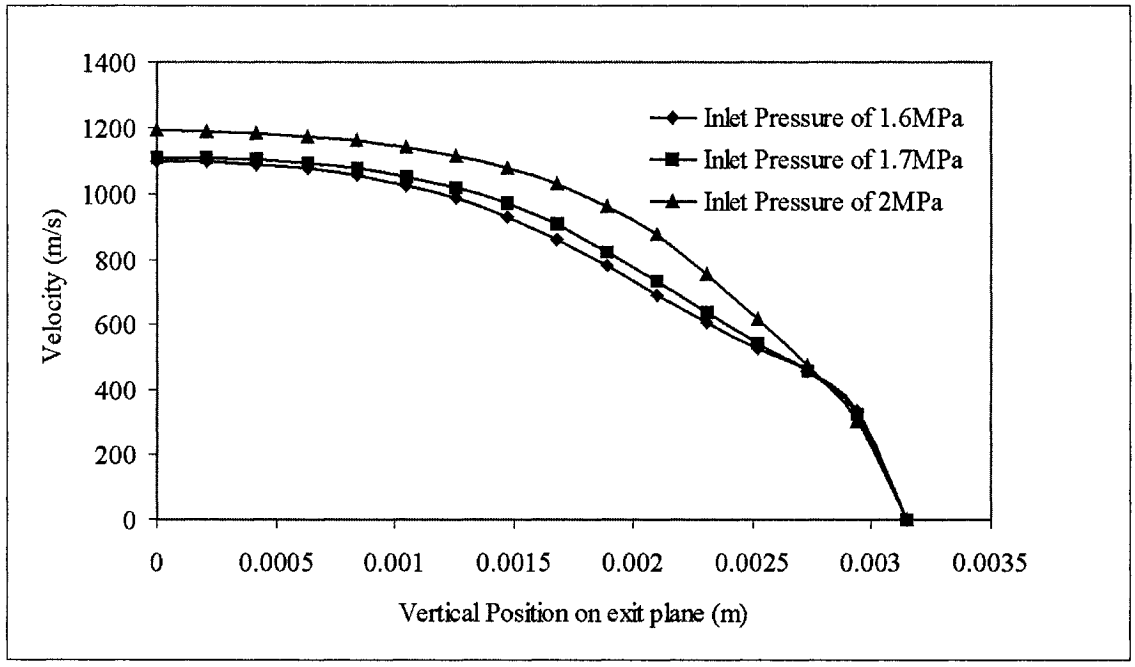

Figure 4-7: Velocity profile at nozzle exit

The preliminary modeling trials provided the necessary information about the geometry that would lead to adequate particle exit velocity and mass flow rate. The results were the basis for the preliminary design specifications listed and discussed in the next section.

4.3.3 Preliminary Design Specifications

Using the meshing and boundary conditions shown in Appendix 1, the preliminary design process yielded nozzle geometry as well as inlet conditions for a desired particle exit velocity, which are outlined in Table 4-3.

Table 4-3: Final geometry and operating parameter for CGDS nozzle

Parameter	Value
Inlet Diameter	4.5 mm
Throat Diameter	2 mm
Exit Diameter	6.3 mm
Stagnation Pressure	2 MPa
Exit Pressure	101 kPa
Converging Length	30 mm
Diverging Length	270 mm
Particle Diameter	20 μm
Particle Exit Velocity	918 m/s

In order to monitor the flow throughout the nozzle, four pressure taps were distributed at different locations inside the nozzle to provide sufficient information to determine the pressure development. Using the pressure profiles generated during the modeling trials, the pressure tap positions and the expected pressure values at each one

are listed in Table 4-4. It is important to note that the nozzle was under-expanded which explains why the pressure at the fourth pressure tap is actually lower than the atmospheric pressure at the exit used in the simulations.

Table 4-4: Pressure tap location and expected pressure readings

Pressure Tap Number	Axial Position (mm)	Pressure (kPa)
1	15	1400
2	38	585.0
3	42	483.6
4	285	41.17

4.3.4 Particle Velocity Modeling

Following the preliminary nozzle design and geometric characterization of the actual aluminium powders, additional particle flow modeling was performed to better represent the broad range of particle diameters in the powder feedstock revealed by the powder SEM (see Figure 4-3). Table 4-5 summarizes the findings.

Table 4-5: Particle velocity modeling for preliminary CGDS nozzle design with injection sites at 35 mm and 40 mm from the nozzle inlet.

Particle Diameter (μm)	Particle Velocity (m/s)	
	35 mm	40 mm
1	812	738
5	1054	1039
10	1052	1036
15	980	965
20	918	904
40	748	739

50	694	686

The results show that smaller particles had a lower exit velocity, which may be due to the difficulties encountered by radially entering the driving gas flow at the injection position. The lower inertia of the smaller particles will require more momentum to perpendicularly traverse the flow at the injection site before it can enter the flow and be accelerated along with it. It can also be due to a decrease in velocity encountered when passing through the shock wave present in the nozzle. Following the modeling process, preliminary experiments were conducted to determine if the material could be sprayed and adhere to a substrate. The goal of the experiments was two-fold: to determine if there was a need for further particle modeling and to prove that the design of the nozzle was done properly.

4.4 Secondary Design Modeling Iteration

Preliminary measurements determined that the nozzle was not manufactured according to specifications. While spraying, it was discovered that it was impossible to obtain the appropriate pressures at the first three pressure taps. From these observations, the diameters of the nozzle were measured to determine if the specified geometry had been followed during the manufacturing process. It was discovered the nozzle had the geometry illustrated in Figure 4-8. The actual nozzle was divided into three distinct regions: a converging portion followed by a straight tube and a diverging portion. The initial diameter reduction occurs in the first 5 mm. This region was added to the converging portion of the nozzle in order to include a collar to hold the nozzle. The 30 mm converging portion of the preliminary design is straight (between 5 and 35 mm in

Figure 4-8) while the diverging portion was to preliminary design specifications. Since the diverging portion of the nozzle was manufactured as specified, the changes in the geometry of the converging portion did not render the nozzle useless.

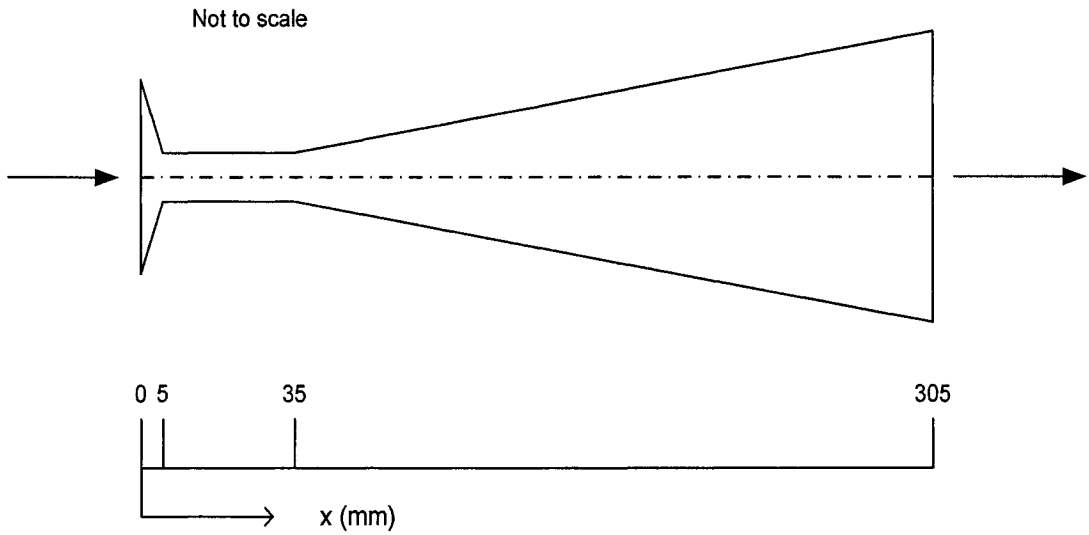

Figure 4-8: Actual CGDS nozzle geometry (mm)

Due to the actual nozzle geometry, the preliminary modeling trials used to select the design parameters were no longer valid. Therefore, the inlet pressure of the actual geometry had to be re-evaluated. This was done using the predicted pressure values at the second and third pressure tapes. During the experiments, the pressure was monitored using those pressure taps. The goal of the second design iteration modeling was to determine the inlet pressure associated with the pressure values at the second and third pressure taps. This was done by modifying the inlet pressure until the appropriate pressure values at specific locations in the nozzle were predicted.

The inlet pressure that produced pressures of 584.7 kPa and 490.7 kPa at the second and third monitoring points, was 1.75 MPa. These pressures compared favourably with the values from the preliminary modeling, which were 583 kPa and 486 kPa, respectively. The geometric model and boundary conditions used in the second design iteration modeling are illustrated in Appendix 1. An additional area was added to model at the inlet of the nozzle to simulate the change in diameter when the flow travels through the stainless tube which feeds the helium into the nozzle.

The predicted pressure distribution inside the actual nozzle is illustrated in Figure 4-9. Again, there is a shock wave prior to the exit of the nozzle. The velocity profile illustrated in Figure 4-10 shows that the driving gas velocity decreases below 1000 m/s. This decrease in velocity is of concern because of the impact it might have on the particle velocity as a result of the shock particle interaction.

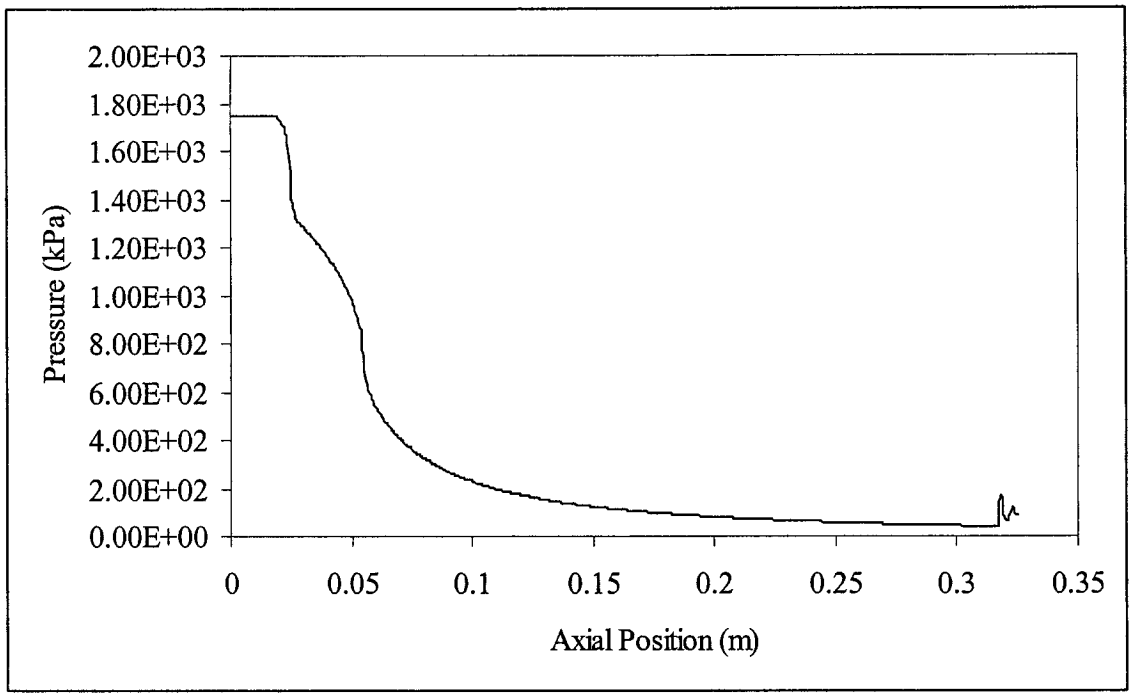

Figure 4-9: Predicted pressure distribution inside actual CGDS nozzle

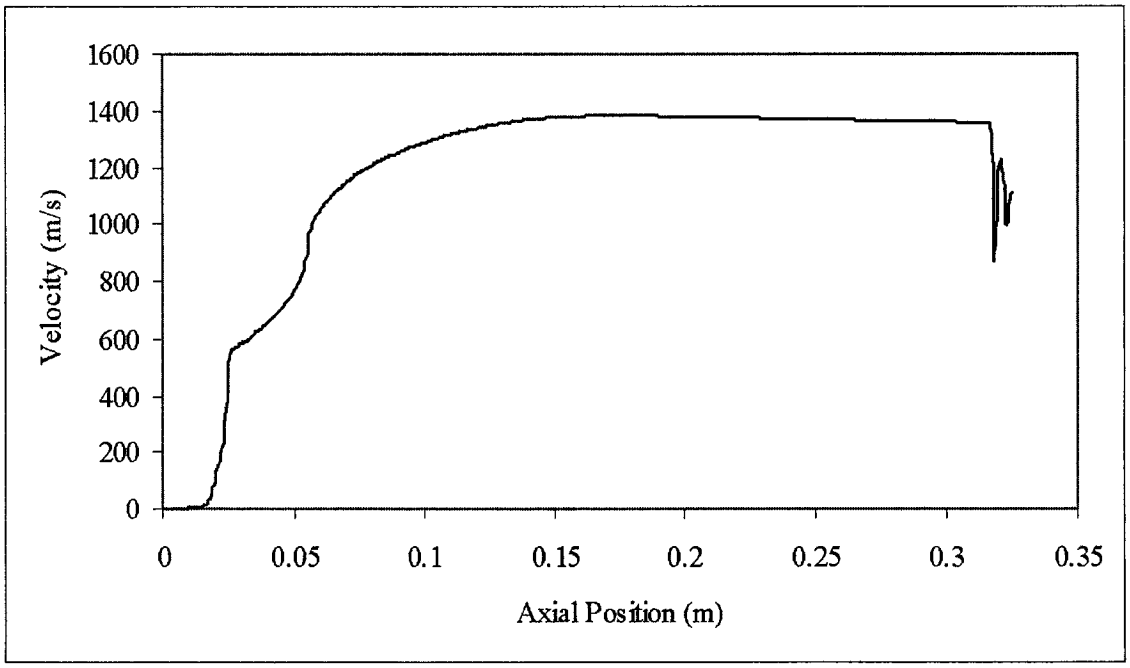

Figure 4-10: Predicted velocity profile inside actual CGDS nozzle

In order to observe the behaviour of the different sized particles in the actual nozzle geometry, the same modeling process performed in Section 4.3.4 was repeated for a number of diameters. The particle sizes were selected based on the powder SEM micrographs of Figure 4-3 and Figure 4-4. The resulting predictions are listed in Table 4-6. One important modification occurred for the post-fabrication modeling of the particle exit velocity. Instead of injecting the powders radially at 700 kPa, the injection was done axially at the inlet. This modification was possible because manipulations with the powder feeder established that it was possible to increase its operating pressure to avalue above 700 kPa without any adverse consequences to the equipment.

Table 4-6: Particle velocity modeling for actual CGDS nozzle for an inlet diameter of 4.5 mm and an outlet diameter of 6.3 mm

Particle Diameter (μm)	Exit Velocity (m/s)
5	1290
10	1158
15	1057
20	990
30	897

The information provided by the post-fabrication modeling showed that the modified geometry would result in a particle exit velocity that was above the documented critical velocities. Therefore, further experimental work was possible using the same monitoring points and values. The experimental set-up used for the experimental work will be described in Chapter 5.

5. EXPERIMENTAL SET-UP

The preliminary modeling results were used as guidelines to develop the experimental set-up. The set-up can be separated into a number of sub-systems, namely, the converging-diverging nozzle system, the powder feeding and injection system, the driving gas supply and control system as well as the substrate support and motion system. In the following chapter, each of these sub-systems will be described.

5.1 Converging-Diverging Nozzle System

The converging-diverging nozzle system is comprised of two parts, the nozzle and the injector. Both of these were designed in-house and manufactured out of stainless steel. The converging-diverging nozzle was manufactured using electrical discharge machining in two separate sections before being soldered together. On the nozzle, four radial injection ports were drilled in order to be able to attach 1/8" NPT fittings anchored at the end of 1/8" stainless steel tubes. Figure 5-1 illustrates the nozzle with its radial powder injection ports.

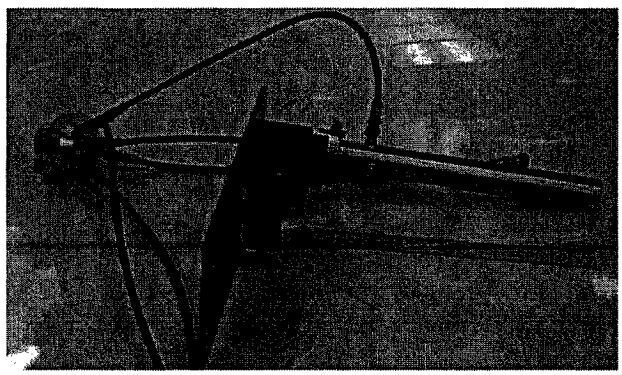

Figure 5-1: Converging-diverging nozzle with stainless steel hose connected to radial injection port.

The second component of this sub-system is the injector. This component is used to inject powders axially at the nozzle inlet and to hold the nozzle on the frame of the spraying chamber. The powders are injected at an angle into the flow in order to facilitate their entry in it.

5.2 Powder Feeding and Injection Units

The main component of the powder feeding unit is the Praxair #1264 Powder Feeder. The powder feeder includes the powder hopper and a #1284 Powder Gas Control Unit. The powder is fed through the hopper using a Roto Feed Powder Hopper which is illustrated in Figure 5-2. The hopper [65] operates on a volumetric feed principle and was designed for use in plasma spray and HVOF systems. The rotating speed of the disk located at the bottom of the hopper controls the amount of powders that is injected into the carrier gas flow.

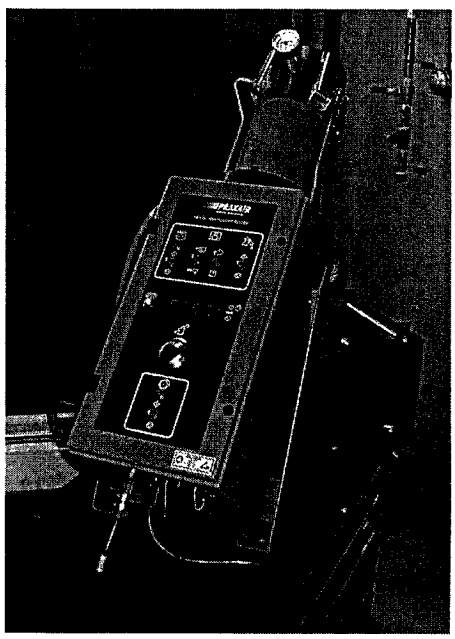

Figure 5-2: Powder hopper

The second component is the powder gas control unit. This component controls the carrier gas pressure. The main control components are the critical orifice flow controllers, which are very insensitive to back pressure changes and can therefore provide a stable and constant flow, regardless of the flow change in the supply line. It is important to note that this unit was used only in the preliminary testing phase. It was by-passed for the parameter testing since it could not provide the necessary carrier gas pressure.

5.3 Driving Gas Supply and Control

The driving gas supply and control system is formed by a bank of compressed helium tanks that are linked to the main line using an in-house designed manifold shown in Figure 5-3. The manifold has a semi-circular shape to keep the total travel distance in a pipe the same for each tank. By keeping the travel distance the same, the losses due to pipe travel were also kept constant which will empty the helium tanks at the same rate.

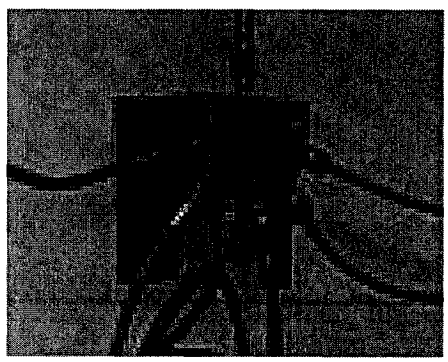

Figure 5-3: Driving gas manifold

The pressure is controlled by a number of one- and two-staged gauges. The two stage gauge (Praxair Model # 4025331-346M) is used on the gas bank to ensure the gas flow is kept constant, no matter the amount of gas left in the tanks.

The pressure inside the converging-diverging nozzle is measured using pressure taps. The four pressure taps are located at 10, 35, 38 and 285mm from the inlet of the nozzle. The pressure taps were designed according to the theory reported by Benedict [66] (Figure 5-4). The larger diameter was set by the available stainless steel tubing which had an outside diameter 0.9144 mm. From that, the minimal depth and the diameter of the tap were determined.

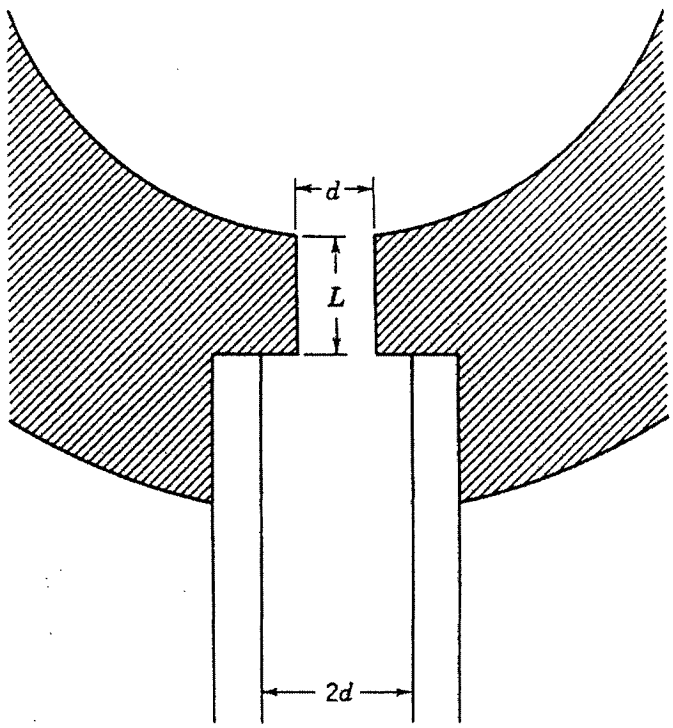

Figure 5-4: Pressure tap design [66]

5.4 Substrate Support and Motion

The transverse motion of the substrate support structure with respect to the stationary nozzle is controlled by a geared motor (12 rpm) along with a bevel gear system and a power screw.

The motor is slotted into the gear that has the vertical rotating axis while the power screw is slotted into the gear that has the horizontal rotating axis. The transverse velocity is approximately 30 mm/min. The substrate is fixed into a slot behind which a resistance is installed for eventual substrate heating.

The main components of the experimental set-up have been outline in this chapter. In the next chapter, the experimental confirmation of the capability of the preliminary CGDS design to produce aluminium coatings is discussed.

6. EXPERIMENTAL RESULTS

This chapter contains the results of the experiments performed to support the work undertaken. The results are divided in two groups: the preliminary experiments performed with radial injection and without heating of the feedstock powders; and, the final testing that was done with axial injection and heating of the powders. Both sets of experiments were carried out using the same powders and the same nozzle. The most important changes between the testing procedures were the injection position, the carrier gas as well as the powder injection rate. Furthermore, the preliminary experiments used both nanocrystalline and conventional powders while the final testing was done uniquely with the conventional powders. The preliminary experiments were performed to determine the deposition capabilities of the setup while the subsequent set of experiments was performed as a preliminary evaluation of the influence of certain spraying parameters. The results from the second testing, along with further studies, will be used to identify the optimal spraying parameters.

6.1 Preliminary Results

The preliminary experiments were performed to determine if the designed nozzle and set-up would be able to deposit aluminium powders onto an aluminium substrate. The experimental set-up used a radial injection system that has not been previously studied. Both conventional and nanocrystalline powders were sprayed. The first set of deposition results was encouraging and demonstrated that the CGDS set-up could reach

the required critical velocity and adequately coat aluminium substrates with both conventional and nanocrystalline aluminium powders.

Particle injection was done radially at the first injection port located 40 mm downstream from the nozzle inlet. The driving gas used was helium while the carrier gas was air. The speed of the powder feeder hopper was kept constant at approximately 2.5 rpm. The nozzle was moved using the stepper motor described in Section 5.4. The analysis performed on the coatings included SEM micrographs, elemental mapping and hardness results. The characterization of the samples was performed at the Materials Science Department at the University of California at Davis.

Figure 6-1 shows a coating sample after it has been prepared for characterization; all samples were prepared as such before hardness tests and SEM observations. Some samples were damaged during this preparation process, and thus impossible to characterize. The damaged specimens cleaved from the substrate during the characterisation preparation phase.

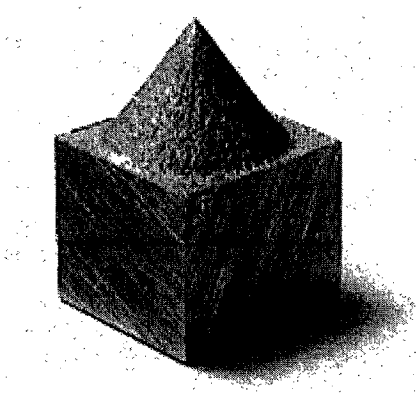

Figure 6-1: Aluminium deposit using conventionally structured powders

It was possible to obtain a micrograph for the conventionally structured coatings, as shown by Figure 6-2. The interface between the deposit and the substrate is visible as a white region which shows that the bonding was not complete. Darker holes in the micrograph are porosity in the coating. It is also interesting to note that there appears to be three particles on the right of the coating. The deformation from the initial spherical shape is clearly visible, as are the voids between the particles. The voids are larger between the particles since they appear to be the last ones that adhered to the substrate. Thus these particles were not subjected to the subsequent particle impacts required to fill the voids. Therefore, it was possible to spray conventional aluminium and obtain a coating, although the quality of the coating was questionable due to the defects outlined previously.

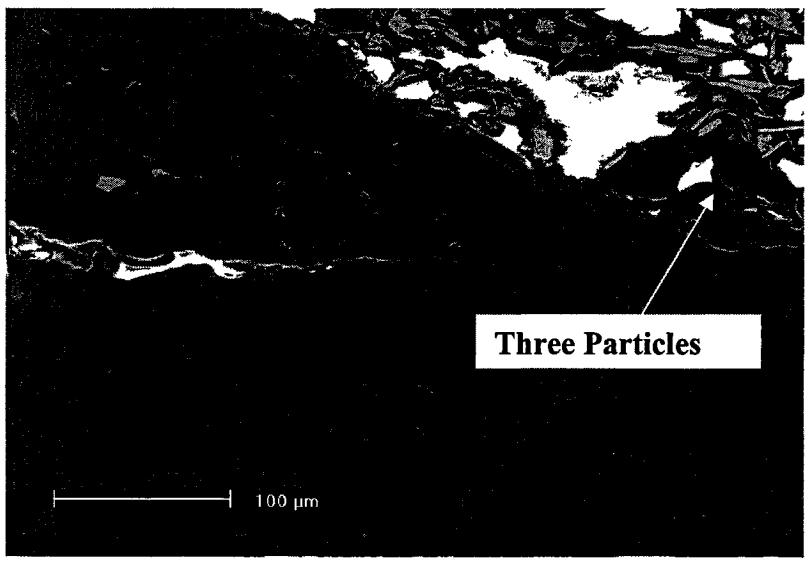

Figure 6-2: SEM of conventional aluminium deposit at the extremity of the deposition interface.

Nanocrystalline powders were also sprayed successfully, as shown in Figure 6-3. Contrary to the conventionally structure aluminium deposit, the voids in the coating are much smaller, even at greater SEM magnification. The interface between the deposit and the substrate is also difficult to perceive. Using a greater level of magnification, (Figure 6-3 (b)), it is possible to see the individual particles that form the coating and the significant deformation they have undergone. Nanocrystalline particles are bigger than their conventionally structure counterparts (as seen in Figure 4-3 and Figure 4-4), as such the voids between them are of a different shape. In the case of nanocrystalline particle, the voids are less circular, which can be attributed to the initial non-spherical shape of the particles. Figure 6-3 (b) shows the particle layering during the deposition process. It can also be observed that the particles undergo significant compressive deformation; the particles are flattened to widths much greater than their initial diameter.

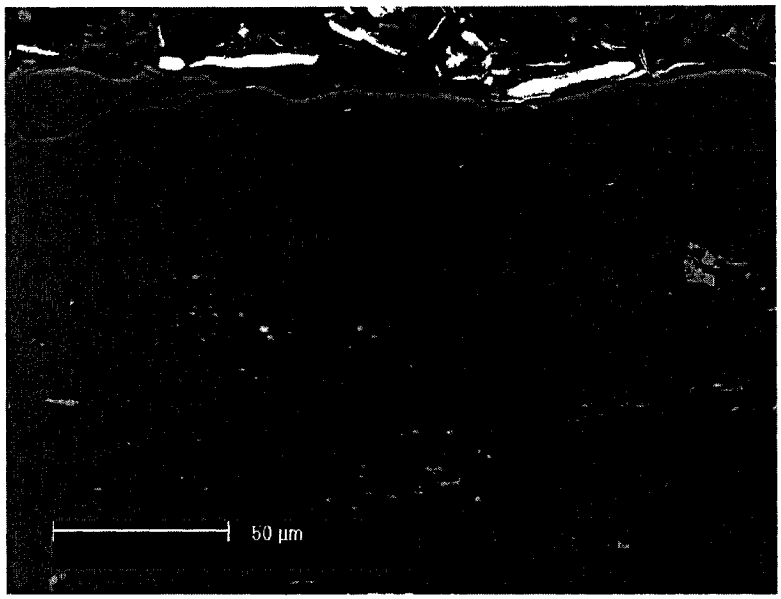

(a)

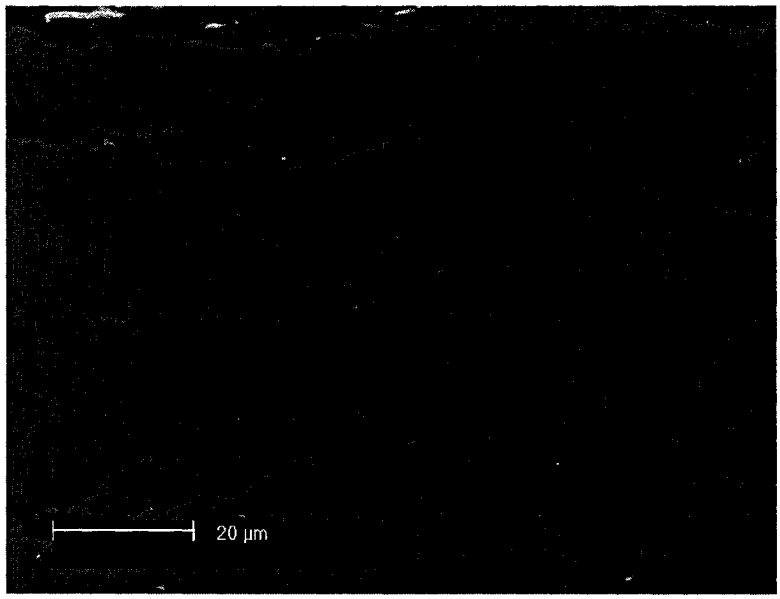

(b)

Figure 6-3: SEM of preliminary spraying results with nanocrystalline powder (a) 50 microns; (b) 20 microns

An additional characterization approach was used in the case of the nanocrystalline coatings since the interface between the particles and the substrate was nearly unperceivable. Using the back-scattering electrons, as in Figure 6-4(a), the interface was again not visible. Since the particles contained more magnesium than the substrate, the specimen was scanned for aluminium and magnesium, as seen in Figure 6-4 (b) and (c). Only once a magnesium microscopy was performed was the interface between the particles and the substrate visible. The bonding between the two was more uniform than in the case of the conventionally structured coatings. The non-spherical and rough-surfaced nanocrystalline particles and the rough-surfaced substrate are ideal for bonding through mechanical kinking. In Figure 6-4 (b), there is a visible void at the right extremity, which was not visible in the other micrographs. This technique was valuable to illustrate some of the coating characteristics that were invisible using SEM micrographs.

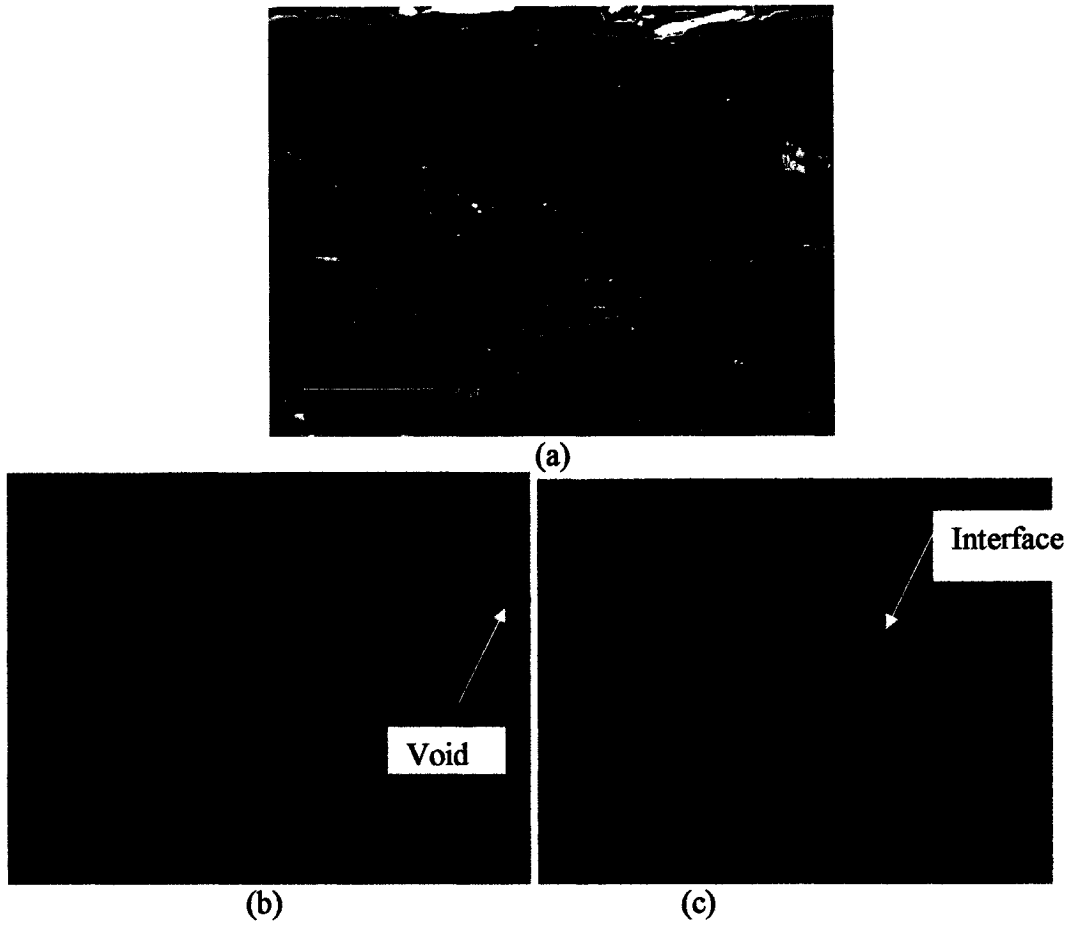

Figure 6-4: Coating interface between nanocrystalline powder and aluminium substrate (a) back-scattering imaging; (b) Al mapping; and, (c) Mg mapping.

Since the difference in magnesium content was found to be a satisfactory method to determine where the substrate/deposit interface was located, a magnesium mapping was performed to determine the thickness of the coating. Figure 6-5 (a) shows the line on which the magnesium mapping was done to determine the local coating thickness. It is important to notice that the mapping was terminated before the last layer of particles, since these would probably not remain on the coating due to the important voids under them. Figure 6-5 (b) indicates the variation in the magnesium content (in weight percent) with respect to the distance from the coating surface. Since the sprayed particles possess

a greater magnesium content, it is possible to deduce the thickness of the coating. In this example, the coating thickness is approximately 17 microns.

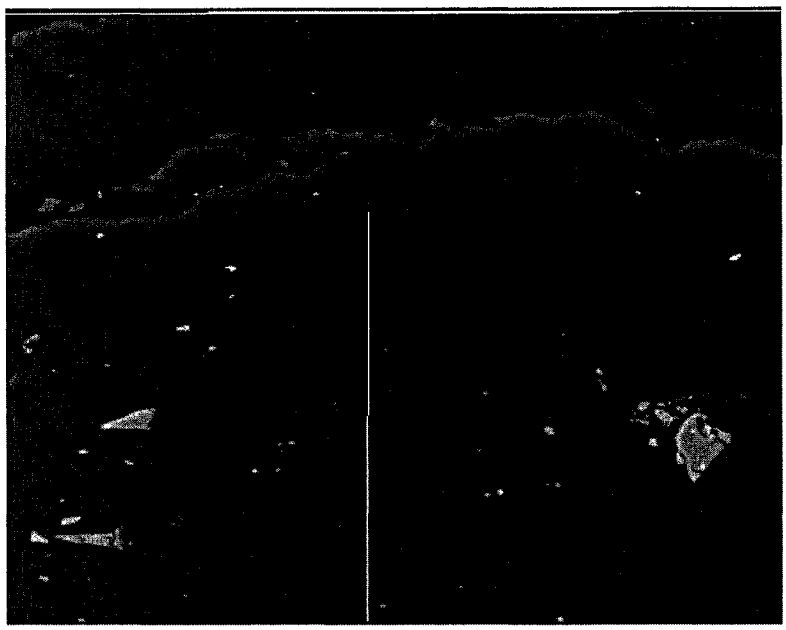

(a)

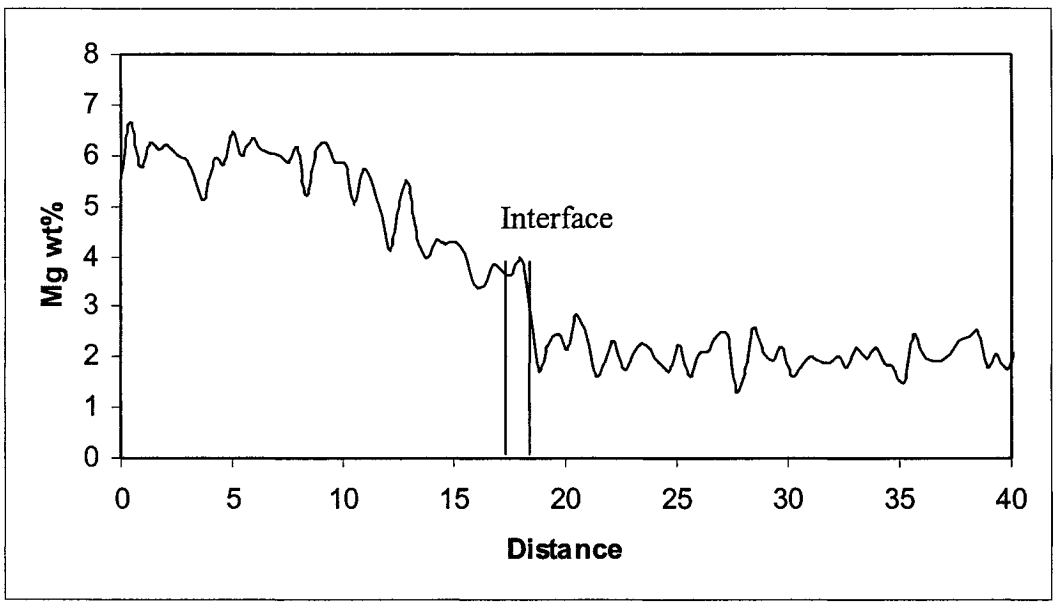

(b)

Figure 6-5: Magnesium mapping (a) mapping line; (b) magnesium content with respect to position on mapping line

In addition to the previous characterization steps, a Vickers hardness test was performed on the samples when possible. The results from these tests are outlined in Table 6-1. Using a 300 g indenter, the hardnesses for both conventional and nanocrystalline coatings were performed. There was, as expected, a significant difference between the two sets of results; the deposit formed with conventional powders presented a much lower Vickers microhardness than the deposits formed using the nanocrystalline powders. There are a number of factors that could contribute to the higher hardness of the nanocrystalline deposits in addition to the inherent difference due to the powder hardness. The particle shape seemed to have a large influence on the coating density. According to Van Steenkiste [16], in the second stage of coating formation, the particles deform and fill out the voids. Since the nanocrystalline particles are non-spherical, less deformation is required to fill the voids, since the mechanical kinking between non-spherical shapes will occur more readily than between spherical particles. Therefore, the non-spherical shape of the nanocrystalline particles might be a significant advantage when trying to form a deposit using CGDS process. There was also a significant range in particle size, as shown by the powder SEMs. While simulating the particle injection, it was shown that smaller particles travel faster but must be greater than 1 μm in order to have sufficient inertia to radially enter the driving gas flow, as was the case for the set-up used for this work. It is possible that the actual minimum size required for flow penetration is slightly greater than predicted. This would explain why smaller conventional particles were not as successful in forming deposits.

Table 6-1: Vickers microhardness results for preliminary testing

Sample	Conventional Powder Vickers microhardness (300 g)	Nanocrystalline Powder Vickers microhardness (300g)
1	N/A	239.3 ± 17.0
2	138.0 ± 16.8	245.0 ± 5.2
3	122.9 ± 16.9	261.4 ± 8.3
4	127.8 ± 1.3	N/A

The preliminary results were encouraging since they showed that the nanocrystalline powder coating had a higher hardness than the conventional powder coatings. They also showed that the particle-substrate interface was more uniform for the nanocrystalline coatings than for the conventional coatings. They also showed that a radial injection could be successful in CGDS. The following step was to study the effect of the spraying parameters on coating formation.

6.2 Parameter Testing

The following tests were done to optimize the CGDS process using the available set-up. Prior to conducting these experiments, a number of modifications were made to improve the CGDS set-up, namely, the addition of an axial injection port at the inlet of the nozzle; the injection pressure was increased to exceed the pressure at the inlet of the nozzle; helium was used instead of air as the carrier gas; the powder feed rate was reduced from approximately 2.5 rpm to between 0.7 and 0.75; and finally, powders were heated to low temperature values, while avoiding melting, prior to spraying, to remove the humidity found in the feedstock powder. The injection could be done at the inlet of the nozzle since the flow actually had a non-negligible velocity and the pressure at that point was not equal to the stagnation pressure but rather closer to 1 MPa. In order to

monitor the influence of selected spraying parameters, a k-factorial testing scheme was used to provide a blueprint for the testing.

6.2.1 K-Factorial Testing Scheme Set-Up

The objective of the following experiments was to determine the influence of a number of selected spraying parameters on coating formation. Three spraying parameters were chosen, namely, the pressure difference between the carrier gas stream and the driving gas stream (i.e. the pressure difference at the injection site), the spraying time, and the stand-off distance. These parameters were selected since they could be easily monitored and varied. The tests were performed to determine which combination of parameters produced, and which individual parameter was the most influential in producing, the best coatings. To determine if the deposition was successful or not, a response variable had to be selected. Hardness was chosen since it is a relatively simple and low cost testing method. In addition to the hardness tests, micrographs of the coatings were performed for visual examination. The experiments were set up using a k-factorial testing scheme [67] in which a minimum and a maximum value were chosen for each of the parameters. All possible combinations are listed in Table 6-2.

Table 6-2: Spraying Parameters

Condition	Pressure Difference (kPa)	Spraying Time (s)	Stand-Off Distance (mm)	Randomly Selected Trial Order
A	50	15	5	1
B	80	45	5	7
C	50	45	10	8
D	80	45	10	4
E	50	45	5	2
F	80	15	5	6
G	50	15	10	3
H	80	15	10	5

Each possible combination was assigned a letter, as shown in Table 6-2. The order of the combinations to be tested was randomly selected; the final testing order randomly generated is included in the table.

6.2.2 Testing Methodology and Observations during Testing

The preliminary round of testing was done to determine if the set-up would successfully produce aluminium coatings onto aluminium substrates. Therefore, the methodology consisted of finding the parameters, through trial and error, that would cause the particles to adhere to the substrate. Once the deposition was successful, it was possible to monitor the spraying parameters. The methodology followed for the second set of experiments, parameter testing, is as follows:

1- Prepare the substrates with an acetone wipe-down after sandblasting all 6 faces of the substrate.

2- Position the substrate in front of the nozzle using the stepper motor and close the spraying chamber.

3- Open the helium tanks used for the driving gas flow.

4- Open the helium tank used for the particle carrier gas.

5- Open the regulator for the driving gas flow and set the inlet pressure to 1020 kPa.

6- Once the appropriate pressure at the inlet has been set, verify that the pressures at pressure taps 2 and 3 are adequate.

7- Open the regulator for the particle carrier gas and adjust if necessary.

8- Turn powder feeder on, and start timing, while continuously monitoring, and adjusting if necessary by opening regulators, the pressure at the nozzle inlet and at the powder feeder.

9- Once spraying time has been reached, simultaneously close regulators for driving gas and particle carrier gas and turn off powder feeder. As the powder feeder stops, open the exhaust valve located on the outside of the powder hopper to release the pressure inside the hopper and evacuate any left-over powder.

These steps were repeated three times for each of the spraying conditions on a single substrate, as illustrated by Figure 6-6.

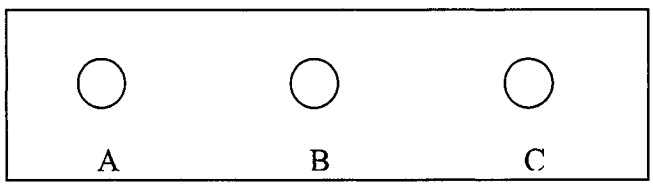

Figure 6-6: Schematic of substrate for parameter testing with three spraying areas

This arrangement did present some problems during the testing. During some of the trials, samples broke off during the following spraying. This could be attributed to many factors. The fracture surface was representative of a brittle failure which could be due to the rate of force generated by the impacting helium jet. The brittle fracture might also be a result of significant levels of cold-working from the fourth stage of coating formation as described by Van Steenkiste [16]. It could also be due to the propagation of the shock wave through the substrate material. Shock wave propagation through the solid can be reflected when it reaches the opposite side of the substrate and travel back to the

spraying surface, affecting the deposit. Finally, some of the deposits showed cracks at the interface, which suggests that they might fracture during sample preparation.

Based on visual inspection, one parameter combination seemed to provide better adhesion. These trials provided thicker samples with no visible crack at the interface. The seventh trial (pressure difference: 80 kPa, stand-off distance: 5 mm and spraying time: 45 sec) provided thick deposits with a marked peak and did not reveal any signs of cracking at the deposit-substrate interface. The results discussed in the following section will determine if the visual inspection results are in agreement with hardness and SEM micrograph results.

6.2.3 Parameter Testing Results

As stated previously, two types of results were provided, namely, the hardness, which is related to the k-factorial scheme and the SEM micrographs, which illustrate the adhesion of the coating as well as the coating-surface interface.

6.2.3.1 Hardness Results

The Vickers micro-hardness results for the thicker samples are listed in Table 6-3. Using the k-factorial scheme, it is possible to determine which of the spraying parameter has the most important influence on the hardness of the sample.

Table 6-3: Vickers microhardness results

Trial Number	a	Standard Deviation	b	Standard Deviation	c	Standard Deviation	Average Hardness
2	n/a	n/a	127.15	7.92	129.34	8.49	128.25
7	128.04	7.93	120.07	11.21	128.55	7.10	125.55
8	n/a	n/a	120.30	2.79	116.04	9.10	118.17

The hardness results show that the second trial produced the harder specimen than the seventh and eighth trials. This is contrary to what the conclusion drawn from the visual inspection, which favoured the seventh trial. The eighth trial resulted in the lower microhardness of all three samples tested. Based on the spraying conditions outlined in Table 6-2, the spraying parameter common to the second and seventh trial and absent in the eighth trial is the stand-off distance, which is 5 mm for the second and seventh trials and 10 mm for the eighth trial. From these results, an early hypothesis that can be drawn is that the stand-off distance is the most important spraying parameter when trying to produce a coating with a higher hardness. It is important to note that the hardness values are all relatively close to one another; when the standard deviations are taken into account, the values overlap. The second trial produced a slightly higher hardness than the seventh one. Again, one spraying parameter was different between the two of them; the pressure difference at the injection site. Interestingly, the second trial has a lower pressure difference yet it does not seem to influence the coating performance. The difference between both spraying conditions is rather small as compared to the overall pressures used. The pressure difference used was either 50 kPa or 80 kPa which does not represent a large percentage of the overall operating pressure which is approximately 1000 kPa. It could be hypothesized that once a certain pressure difference is achieved at the injection site the performance of the process will not be improved if the difference is further increased.

The hardness results are one way of evaluating the performance of the coating but they do not convey a complete picture as a hard sample could also be very thin whereas a thicker sample could have a lower hardness. In order to have a more complete view of the performance of the coating, scanning electron microscopy was performed on the samples. The most important results are shown in the following section.

6.2.3.2 SEM Results

In addition to the hardness results, each sample was examined under a scanning electron microscope (SEM). Some of the specimens were broken during the processing and could not be analyzed. The following section contains the SEM micrographs which display interesting characteristics.

In the first trial no SEM was done since the coatings separated from the substrate during preparation. The second trial, where parameters were set at 50 kPa pressure difference, 45 seconds spraying time and 5 mm stand off distance, a single sample provided SEM micrographs (trial 2B). In the 394x magnification SEM, seen in Figure 6-7, porosity resulting from the voids between the impacting particles is visible. The interface is not shown in this particular SEM.

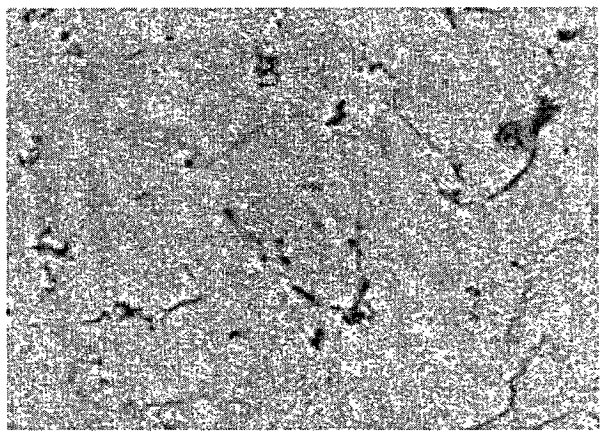

Figure 6-7: SEM for trial 2B, 394x magnification

Figure 6-8 was taken at the extremity of the coating, where the coating is decreasing in thickness. It is possible to see how the last impacted particle has deformed in order to adhere to the substrate. Porosity is again present. The interface is not shown on this particular SEM.

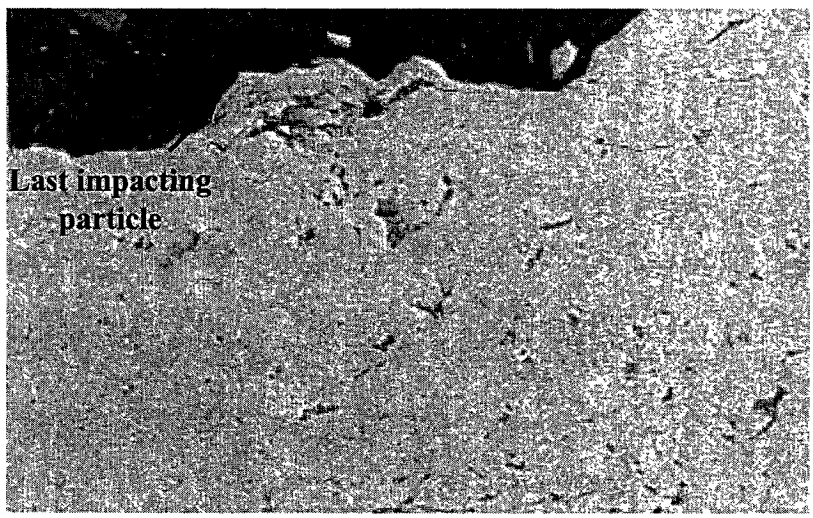

Figure 6-8: SEM for trial 2B, extremity of the coating, 197x magnification

In the case of the third trial (parameters: 50 kPa pressure difference, 15 seconds spraying time and 10 mm stand-off distance), no samples were damaged during preparation, therefore, micrographs are available for all 3 trials. The more interesting ones will be discussed. In Figure 6-9, the interface between the particles and the substrate is noticeable, mainly because of the difference in porosity between the two materials and the presence of impurities in the substrate (white spots). These impurities can be due to dirt that was not removed during the substrate preparation or to different alloying materials used in the substrate. Since the interface is visible, an approximate coating thickness can be estimated using the scale from the SEM. This coating has an approximate thickness of 222 μm. There is also significantly more, and unevenly distributed, porosity than in the previous sample. The lower portion of the coating does present more porosity than the mid portion. The pores also change in form in the coating. The voids, in the lower portion of the coating, appear smaller and more circular. Furthermore, the particle layers are more noticeable at the top of the coating; this likely due to lower levels of peening and thus the particles have had less opportunity to fill the voids.

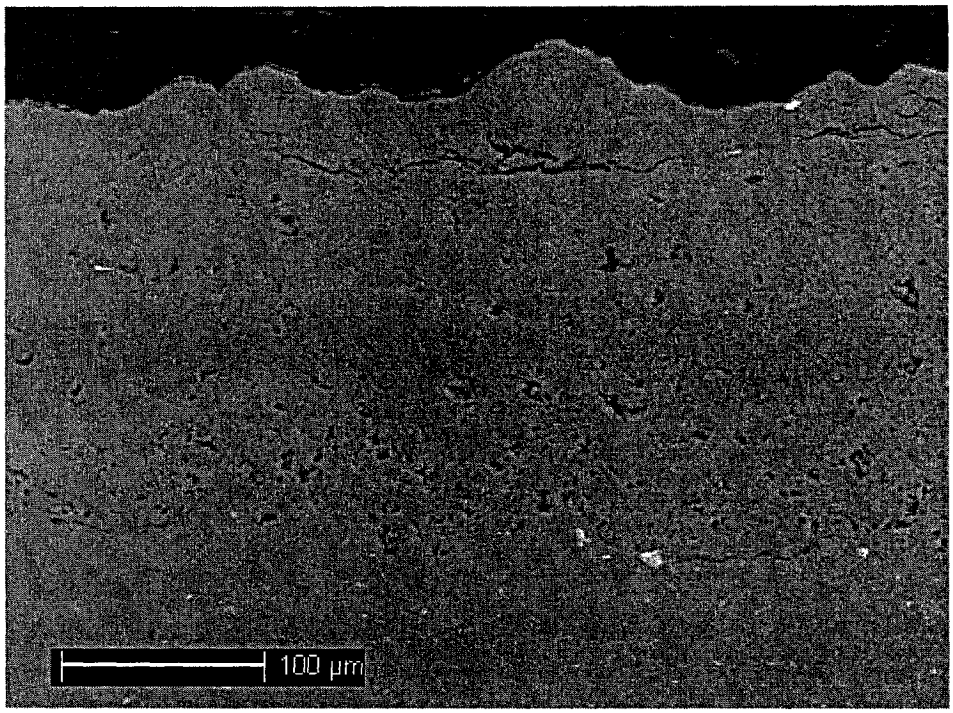

Figure 6-9: SEM of trial 3A, magnification 197x

The SEM seen in Figure 6-10 was again taken at the extremity of the coating and at a greater magnification. The layer at the surface of the coating represents the oxides that developed on aluminium when it is exposed to the oxygen in the air. Also, the shape of a single particle, which has been changed from the sphere-like form the particles possessed before spraying to a tear-like form, can be seen. This is representative of the plastic deformation inherent to CGDS. The manner in which each particle has deformed is clearly visible under this high magnification since the edge of each particle is visible.

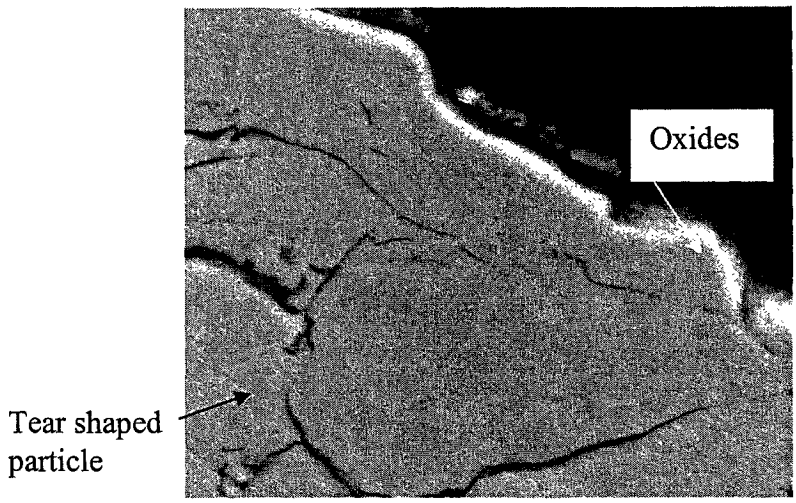

Figure 6-10: SEM of trial 3A, magnification 1100x

Figure 6-11 shows two interesting phenomena. First and foremost, there are clearly visible circular voids, which are undesirable in the coating since they can act as stress concentrations and may become failure initiating sites. Also, a particle that has not been deformed is visible in the top left-hand corner of the SEM. This is unusual; however, the adhesion could be a result of the non-independent bonding that Alkhimov et al [17] described in their early work.

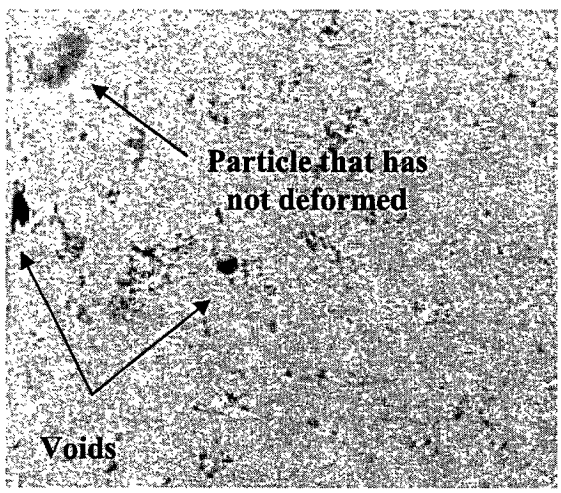

Figure 6-11: SEM of trial 3A, magnification 197x

Figure 6-12 illustrates how the thickness of the coatings can be approximated. Using the scale provided, the measurement is made and the conversion is subsequently done. For example, the thickness of sample 3C seems to be in the order of 100 μm. Again, the oxide layer at the surface of the aluminium is clearly visible as are the voids in the coating.

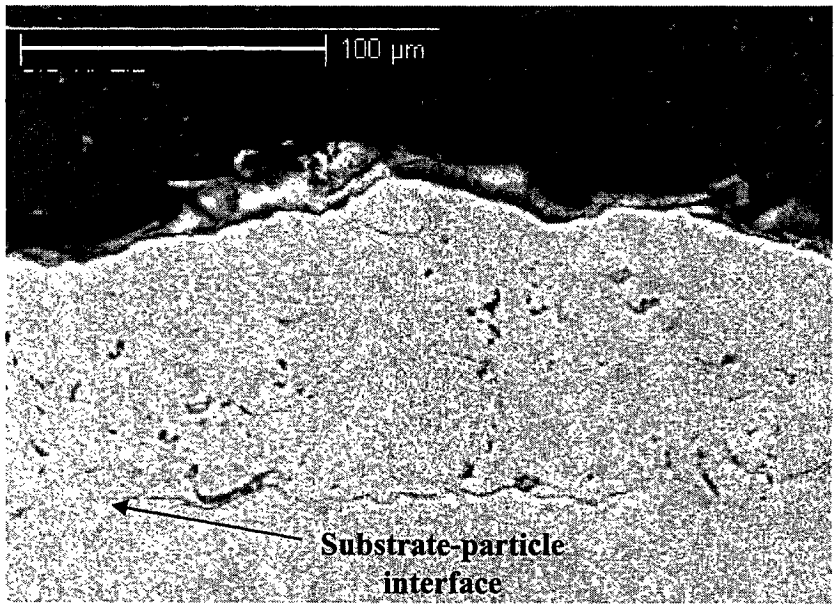

Figure 6-12: SEM for trial 3C, magnification 295x

The SEM seen in Figure 6-13 is a good example of the peening effect of the particles as the voids near the surface are much bigger than the ones near the substrate-particle interface. It is also possible to see that some oxides are still in the coating. This might have an effect on the hardness of the coating as the oxides are very hard compared to the aluminium.

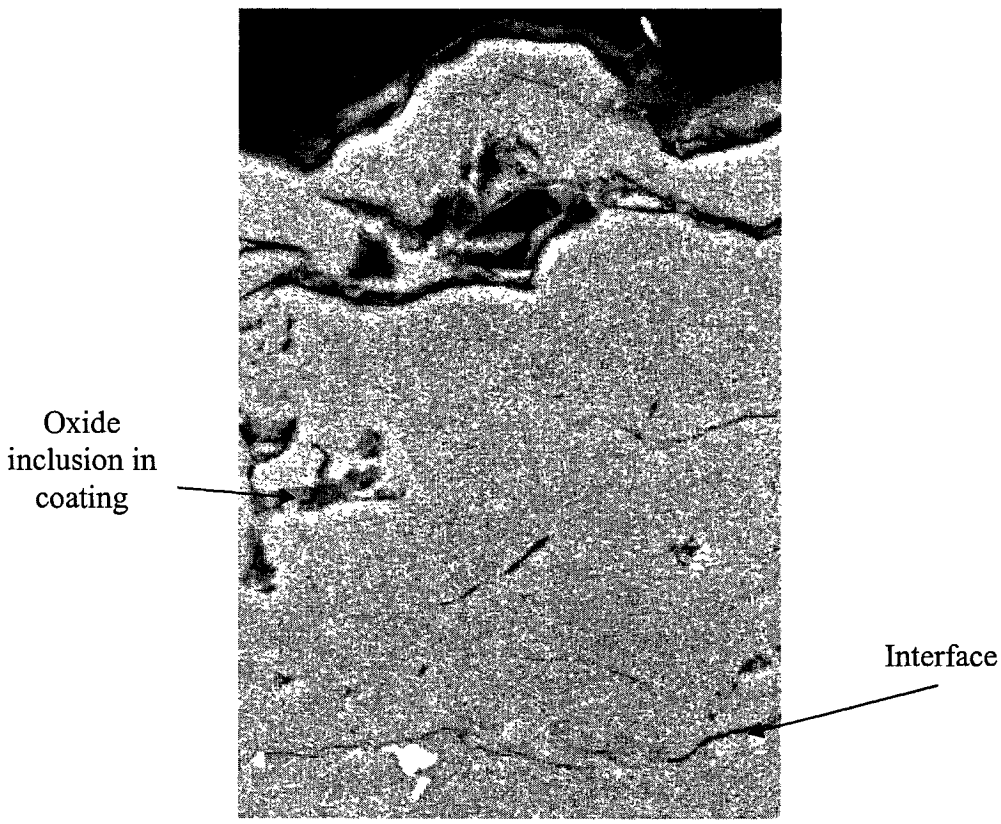

Figure 6-13: SEM of trial 3C, magnification 591x

Figure 6-14 provides an indication that the spraying conditions affect the coating porosity as well as the coating thickness. In the fifth trial, the pressure difference between the driving gas and the powder carrier gas was 80 kPa, the spraying time was 15 seconds and the stand-off distance was 10 mm. The approximate thickness is 200 μm and the porosity seems to be more evenly distributed and smaller than the porosity observed for trial 3, which was performed with a smaller pressure difference. The elongated porosity observed at the last particle layer is smaller than the one observed in Figure 6-9.

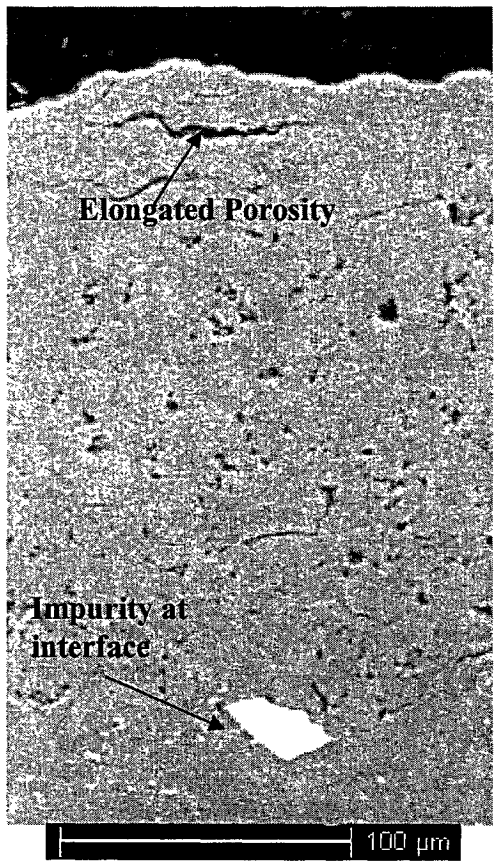

Figure 6-14: SEM for trial 5A, magnification 282x

In the seventh trial, the pressure difference was at its highest, as was the spraying time while the spraying distance set at its lowest level. The preliminary hypothesis was that these conditions would produce better, thicker and denser coatings. Figure 6-15 does illustrate that the porosity is less prevalent than in other showcased SEMs such as Figure 6-7.

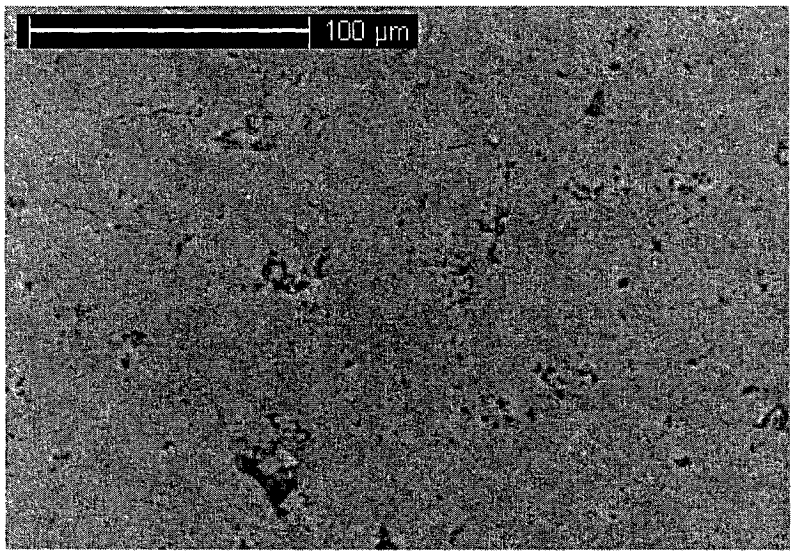

Figure 6-15: SEM of trial 7A, magnification 272x

Even though it was assumed that the seventh trial would produce the better result, Figure 6-16 shows the presence of a rather important crack. The crack might be responsible for the brittle fractures often observed between the deposit and the interface. This might act as a stress concentration and a weak point in the structure from which the fracture can propagate. Similarly, as shown by Figure 6-17, cracks can also form perpendicular to the surface. These are undesirable phenomena as they can also affect further testing.

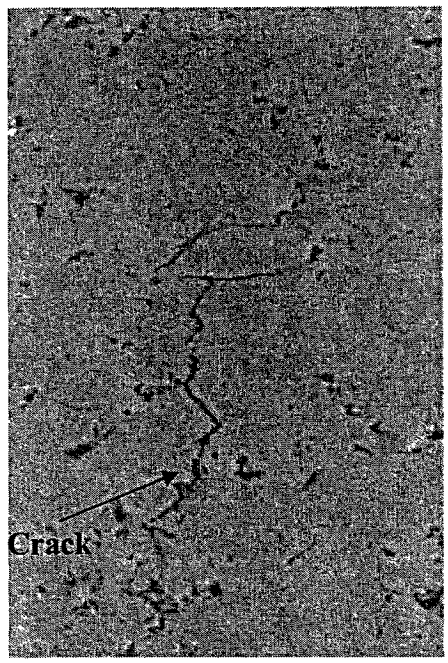

Figure 6-16: Crack observed in SEM for trial 7C, magnification 273x

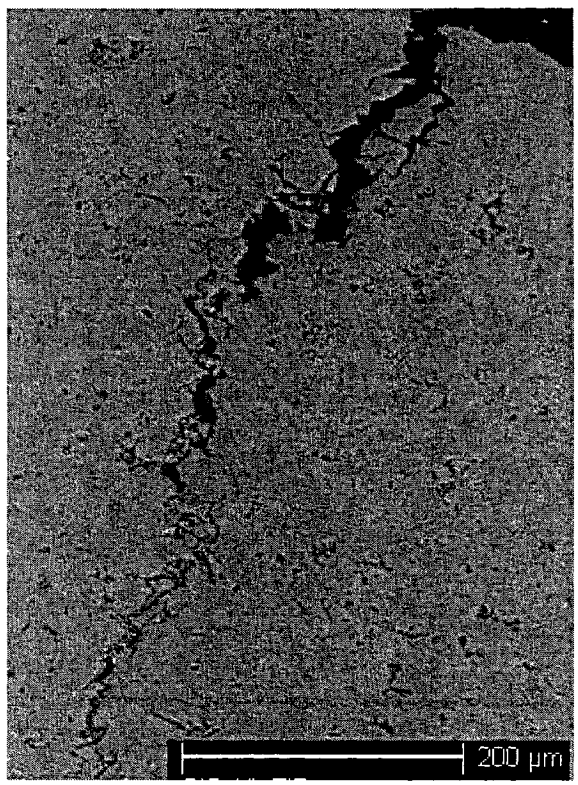

Figure 6-17: Crack at the surface of the deposit for trial 7C, magnification 137x

The SEM micrographs provided insight into the coating structure and confirmed what the hardness results showed in terms of the optimal spraying conditions. They complement the findings of the hardness testing as they can show smaller details that would go unnoticed with only hardness testing.

6.2.4 Comparison between Preliminary Testing and Parameter Study

The preliminary testing showed the better performance of the nanostructured coatings. The conventional coatings sprayed in both testing phases are very similar. The hardness of the samples is slightly higher in the preliminary testing but the density and the thickness of the samples are higher for the parameter study. The stand-off distance for the preliminary testing was between 3 and 5 mm. This also confirms the hypothesis that the stand off distance was the most important parameter in the three selected parameters. The parameter study, even if it showed very similar results to the preliminary work, was useful since it provided a more precise analysis of the spraying parameter and a better understanding of the optimal conditions for the formation of a coating. It provided guidelines that can be used for future experiments.

7. CONCLUSIONS, RECOMMENDATIONS AND POSSIBLE FUTURE WORK

The objective of this work was to develop a cold-gas dynamic spraying system to spray both conventional and nanocrystalline aluminium for corrosion protection purposes and to perform a parameter study for aluminium coatings. The development of the system included the geometrical design of the converging-diverging nozzle using gas dynamics theory as well as computational fluid dynamics. The nozzle design was optimized for the use of aluminium powders and to provide a particle exit velocity above 900 m/s using helium as a driving gas to surpass the reported critical velocity for aluminium. During the design process, modifications were made to minimize the operational costs by minimizing the mass flow rate of driving gas. Subsequent modeling was performed to determine the injection pressure necessary for the actual geometry to provide the appropriate pressures at the monitoring points (pressure taps).

Once the design of the converging-diverging nozzle was completed and the set-up was built, experiments were performed to determine the plausibility of successfully spraying conventional and nanocrystalline aluminium using a radial injection. Preliminary tests indicated that the set-up successfully sprayed both nanocrystalline and conventional aluminium powders using radial particle injection and air as carrier gas and without particle heating. The initial results also showed that the nanocrystalline coatings had a higher hardness than the conventional coatings. The substrate-deposit interface was also more uniform and showed less porosity when using nanocrystalline coatings. The higher hardness can be attributed to the greater presence of grain boundaries in the

nanocrystalline feedstock. The uniform interface and the lower porosity can be attributed to the non-spherical shape of the nanocrystalline particles which must undergo less deformation to mechanically kink with the substrate and the other particles.

After the preliminary tests, a second computational model was derived in order to predict the particle velocity for the actual geometry of the nozzle, which was slightly different than the one submitted following the preliminary design. The subsequent modeling provided the necessary pressure at the nozzle inlet to match original particle exit velocity requirements.

Subsequent testing was performed to determine the optimal spraying conditions. To determine which spraying parameter had the most influence on the performance of the coating while limiting the number of experiments, a k-factorial testing scheme was devised. Three spraying parameters were varied: the spraying time, the stand-off distance and the pressure difference at the injection. The hardness of the coating was chosen as the variable to determine the coating performance as a function of the other parameters. The hardness results can be used to drawn an initial conclusion that the stand off distance was the most important spraying parameter.

Other parameters were altered with respect to the preliminary testing phase, but were held constant for the second set of tests. These modifications were done to improve the performance of the process in hopes that thicker and denser coatings would be

produced. For these tests, only conventional powders were used; the carrier gas used was helium; and, particles were heated and injected axially at the inlet of the nozzle.

Micrographs were taken to visualize the coatings. These show that porosity varies in shape in different regions of coating. Porosity shapes range from spherical near the substrate-deposit interface, elongated near the top layer of particles and are a random mix of both between surface and interface. Notable is the smaller quantity of porosity in the middle of the coatings. Finally, it was discovered that conventional powders are more difficult to spray due to their initial spherical shape. The principal inter-particle and particle/substrate adhesion process is mechanical kinking which appears impeded by the higher energy required to deform spherical particle.

The work undertaken for this research provided important fundamental insight for subsequent studies using the CGDS system designed for this thesis. Single deposits should be done on each substrate since subsequent spraying can fracture off the existing deposit because of the continued pressure applied by the impacting helium jet. Also, a new pressure tap design should be introduced as the fragility of the one used in this work can be detrimental to the success of the experiment.

The completed work answered some questions about CGDS but has generated a number of them which should be studied in future work. The parameter study should be performed using other materials to determine if the same spraying parameters have the same influence on different materials. The parameter testing could be expanded to include other parameters such as feed rate, and gas and particle temperature. The parameter study could also be performed using both radial and axial injection to determine if the axial injection is indeed more successful than the radial injection, The effect of the type of substrate can also be studied. The propagation of the shock wave through the coating and substrate should also be studied. This could provide information regarding the bonding mechanism. Finally, a number of mathematical models can be derived. The boundary layer thickness can be calculated using pressure profiles generated by CFD, as can the compressed layer in front of the substrate and the deformation of the particles and the substrate.

REFERENCES

1. Tullmin Consulting, Corrosion Costs, http://www.corrosion-club.com/costs.htm, 2004.
2. ASM International, Thermal Spraying Glossary, http://www.asm-intl.org/tss/glossary/t.htm, 2004.
3. Bernecki, T., *Surface Science: A Lesson from Thermal Spray Technology*, Materials Engineering Institute, ASM International, p.27, 1994.
4. Harris, D.H., *Selected Applications: A Lesson from Thermal Spray Technology*, Materials Engineering Institute, ASM International, p.13, 1994.
5. Cam Implants, Hydroxy apatite coatings, http://www.camimplants.com/en/, May 2004.
6. Popoola, O., Reatherford, L.V. and McCune, R.C., *Process and Materials Development for Adherently Sprayed Valve Seats on Aluminium Engine Head* , International Congress & Exposition, Detroit, MI, USA , February 1998.
7. McCune, R.C., *Potential applications of cold-spray technology in automotive manufacturing*, Conference Proceedings, ITSC 2003, ASM International, 2003.
8. Intelligent Media Venture, *Matrix Coatings, Inc*, http://www.matrixcoatings.net/page3.html#restorative, May 2004.
9. Standford, M., Oil-Free Turbomachinery Program- High Temperature Coatings, NASA, http://www.grc.nasa.gov/WWW/Oilfree/coatings.htm, May 2004.
10. Patric Engines, *Thermal Sprayed Coatings in Gas Turbines,* http://molpc60.me.tut.fi/euroceram/reg/PDFs/coat/16-Parkki.PDF, May 2004.

11. Fauchais, P., Vardelle, A., Dussoubs, A., *Quo Vadis Thermal Spraying?*, Journal of Thermal Spray Technology, Volume 10 (1), March 2001.

12 Gordon England Independent Metallurgist and Consultant to the Thermal Spray Coating Industry, Plasma Spraying, http://www.gordonengland.co.uk/ps.htm, November 2002.

13. Metallisation Limited, *Introducing the Hypersonic Spray Process*, http://www.metallisation.com/hvof/hyper-fs.htm, May 2004.

14. Legg, K., *HVOF in Repair and Overhaul- Hugher Reliability at Lower Cost?,* Rowan Technology Group, http://www.rowantechnology.com/Documents/hvof/HVOF%20in%20O&R.pdf, 2002.

15. Gordon England Independent Metallurgist and Consultant to the Thermal Spray Coating Industry, Detonation Gun Spraying, http://www.gordonengland.co.uk/ds.htm, November 2002.

16. Van Steenkiste, T.H., *Kinetic Spray: A New Coating Process*, Key Engineering Materials, Vol. 197, p.59-86, 2001.

17. Alkhimov, A.P., Kosarev, V.F. and Papyrin, A.N., *A Method of "Cold" Gas-Dynamics Deposition*, Sov. Phys. Dokl. 35(12) p.1047-1049, December 1990,.

18. Alkhimov, A.P., Papyrin, A.N., Kosarev, V.F., Nerterovich, N.I., Shushpanov, M.M., US Patent 5,302,414,12, April 1994.

19. Dykhuizen, R.C, Smith, M.F., *Gas Dynamics Principles of Cold Spray*, Journal of Thermal Spray Technology, Vol. 7 (2), p.205-212, 1998.

20. Gilomore, D.L., Dykhuizen, R.C., Neiser, R.A., Roemer, T.J. and Smith, M.F., *Particle Velocity and Deposition Efficiency in the Cold Spray Process*, Journal of Thermal Spray Technology, Volume 8 (4), p.576-582, December 1999.

21. Alkhimov, A.P., Kosarev, V.F., Klinkov, S.V., *The Features of old Spray Nozzle Design*, Journal of Thermal Spray Technology, Volume 10 (2), , p.375-381 June 2001.

22. Papyrin, A.N., Alkhimov, A.P., Kosarev, V.F., Klinkov, S.V., *Experimental Study of Interaction of Supersonic Gas Jet with Substrate Under Cold Spray Process*, Thermal Spray 2001: New Surfaces for a New Millenium, Conference Proceedings, ASM International, USA, p.423-431, 2001.

23. Kosarev, V.F., Klinkov, S.V., Alkhimov, A.P., Papyrin, A.N., *On Some Aspects of Gas Dynamics of the Cold Spray Process*, Journal of Thermal Spray Technology, Volume 12 (2), p.265-281, June 2003.

24. Jodoin, B., *Cold Spray Nozzle Mach Number Limitation*, Journal of Thermal Spray Technology, Volume 11 (4), December 2002.

25. Vlcek, J., Huber, H., Voggenreiter, H., Fischer, A., Lugscheider, E., Hallén, H., Pache, G., *Kinetic Powder Compaction Applying the Cold Spray Process: A study on parameters*, Thermal Spray 2001: New Surfaces for a new millennium, ASM International, USA, 2001.

26. Callister, W.D., *Materials Science and engineering: an introduction*, John Wiley and Sons, 5th Edition, New York, 2000.

27. Zhang, D., Shipway, P.H., McCartney, D.G., *Particle-Substrate Interactions in Cold Gas Dynamic Spraying*, Thermal Spray 2003: Advancing the science and applying the technology, ASM International, Materials Park, Ohio, USA, p.45-52, 2003.

28. Shukla, V., Elliot, G.S., Kear, B.H., *Nanopowder Deposition by Supersonic Rectangular Jet Impingement*, Journal of Thermal Spray Technology, Vol. 9 (3), p.394-398, September 2000.

29. Lima, R.S., Karthikeyan, J., Kay, C.M., Lindemann, J., Berndt, C.C., *Microstructural characteristics of cold-sprayed nanocrystalline WC-Co coatings*, Thin Solid Films, 416, p.129-135, 2002.

30. Shukla, V., Elliot, G.S., Kear, B.H., McCandlish, L.E., *Hyperkinetic deposition of nanopowders by supersonic rectangular jet impingement*, Scripta Mater, Vol. 44, p.2179-2182, 2001.

31. Bolesta, A.V., Fomin, V.M., Sharafutdinov, M.R., Tolochko, B.P., *Investigation of interface boundary occurring during cold gas-dynamic spraying of metallic particles*, Nuclear Instruments and Methods in Physics Research A, Vol. 470, p.249-252, 2001.

32. Nix, R., *How do Molecules Bond to Surfaces?* , Queen Mary University of London, http://www.chem.qmw.ac.uk/surfaces/scc/scat2_2.htm, 1998.

33. Dykhuizen, R.C., Smith, M.F., Gilmore, D.L., Neiser, R.A., Jiang, X., Sampath, S., *Impact of high velocity cold spray particles,* Journal of Thermal Spray Technology, Volume 8 (4), p.559-564, December 1999.

34. Assadi, H., Gärtner, F., Stoltenhoff, T., Kreye, H., *Bonding mechanism in cold gas spraying*, Acta Materialia, Vol, 51, p.4379-4394, 2003.

35. Wright, T.W., *The Physics and Mathematics of Adiabatic Shear Bands*, Cambridge Australia, http://www.cambridge.org/aus/catalogue/catalogue.asp?isbn=0521631955, August 2002.

36. Papyrin, A.N., Kosarev, V.F., Klinkov, S.V., Alkhimov, A.P., *On the interaction of high speed particles with a substrate under the cold spraying*, Conference Proceedings, ITSC 2002, ASM International, 2002.

37. Van Steenkiste, T.H., Smith, J.R., Teets, , *Aluminium coatings via kinetic spray with relatively large powders particles*, Surface and Coating Technology, Vol. 154, p.237-252, 2002.

38. Van Steenkiste, T.H., Smith, J.R., Teets, R.E., Moleski, J.J., Gorkiewicz, D.W., Tison, R.P., Marantz, D.R., Kowalsky, K.A., Riggs, W.L., Zajchowski, P.H., Pilsner, B., McCune, R.C., Barnett, K.J., *Kinetic Spray coatings*, Surface and Coatings Technology, Volume 111, p.62-71, 1999.

39. Morgan, R., Fox, P., Pattison, J., Sutcliffe, C., O'Neil, W., *Analysis of cold gas dynamically sprayed aluminium deposits*, Materials Letters, Vol. 58, 1317-1320, 2004.

40. Eesley, G.L., Elmoursi, A., Patel, N., *Thermal properties of kinetic spray Al-SiC metal-matrix composite*, Journal of Materials Research, Vol. 18, No.4, p.855-860, April 2003.

41. Borchers, C., Gärtner, F., Stoltenhoff, T., Assadi, H., Kreye, H., *Microstructural and macroscopic properties of cold sprayed copper coatings,* Journal of Applied Physics, Volume 93, No.12, p.10064-10070, June 2003.

42. Van Steenkiste, T., Smith, J.R., *Evaluation of coatings produced via kinetic and cold spray processes*, Conference Proceedings, Thermal Spray 2003: Advancing the Science and Applying the Technology, ASM International, USA, p.53-61, 2003.

43. McCune, R.C., Donlon, W.T., Popoola, O.O., Cartwirght, E.L., *Characterization of copper layers produces by cold-gas dynamics spraying*, Journal of Thermal Spray Technology, Volume 9 (1), p.73-82, March 2002.

44. Dykhuizen, R.C., Neiser, R.A., *Optimizing the cold spray process*, Conference Proceedings, Thermal Spray 2003: Advancing the Science and Applying the Technology, ASM International, USA, 2003, p.19-26.

45. Stoltenhoff, T., Kreye, H., Richter, H.J., *An analysis of the cold spray process and its coatings*, Journal of Thermal Spray Technology, Volume 11 (4), p.542-550, December 2002.

46. Papyrin, A.N., *Cold Spray Technology*, Advanced Materials and Processes, Vol. 159 (9), p.49-51, 2001.

47. KTECH, *Cold Gas Dynamic Spraying,* 1999, www.ktech.com/coldspray.pdf

48. Fox, R.W., McDonald, A.T., *Introduction to fluid mechanics*, 5th Edition, John Wiley and Sons, New York, 1998.

49. Anderson, J.D., *Modern Compressible Flow with Historical Perspectives*, 3rd Edition, McGraw Hill, New York, p.12, 2003.

50. John, J.E.A., *Gas Dynamics*, Prentice Hall, 2nd Edition, 1984.

51. Preston, R., *Aerodynamics Text: Formation of Normal Shock* Wave, http://142.26.194.131/aerodynamics1/High-Speed/Page2c.html, May 2004.

52. Davidhazy,A, *Imaging and Photographic Technology*, Rochester Institute of Technology, www.rit.edu/~andpph/ ipt.html, 2003.

53. Callister, W.D., *Science et génie des matériaux,* Modulo, 1ère Édition, 2001.

54. Hull, D., Bacon, D.J, *Introduction to Dislocations*, Pergamon Press, New York, 257 p. , 1984.

55. ASM Handbooks on-line, Volume 2, Properties and Selection: Nonferrous Alloys and Special-Purpose Materials -> Properties of Wrought Aluminium and Aluminium Alloys -> 5083 (4.4Mg-0.7Mn-0.15Cr), http://80-products.asminternational.org.login.ezproxy.library.ualberta.ca/hbk/index.jsp., February 2004.

56. Riggs, W.L., *Testing and Characterization: A lesson from thermal spray technolocy*, Materials Engineering Institute, ASM International, 1994.

57. Patankar, S.V., *Numerical Heat Transfer and Fluid Flow*, Taylor and Francis, 1st Edition, 1981.

58. Anderson, J.D., *Computational Fluid Dynamics: The basics with applications*, McGraw Hill, 1st Editionp.497, 1995,.

59. Fluent 5.5 Documentation, User's Guide, 2001.

60. Beaulieu, D., *Calcul de charpents d'aluminium*, Presses de l'Aluminium, Chicoutimi, 2003.

61. Kalpakjian, S., Schmid, S.R., *Manufacturing Engineering and Technology*, Prentice Hall, 4th Edition, 2000.

62. Suryanarayana, C., *Mechanical alloying and milling,* Progress in Materials Science, Vol. 46, 2001, p.1-184.

63. Limat 2001, Aluminium Alloys, http://www.arofe.army.mil/Conferences/LiMAT2001/limat2001aluminium_alloys.htm, May 2004.

64. Crawford, P., *What are Nanocrystalline Materials?* , Rensselear Polytechnical Institute, http://www.rpi.edu/dept/materials/COURSES/NANO/crawford/index.html, 1997.

65. Praxair User Guide, #1264 Powder Feeder, December 2002.

66. Benedict, R.P., *Fundamentals of temperature, pressure and flow measurements*, John Wiley and Sons, New York, 2nd Edition, 517 p., 1997.

APPENDIX 1: Grid, Mesh and Boundary Conditions for CFD Model

(a) Meshing for Preliminary Design, width of control volume: 0.5 mm

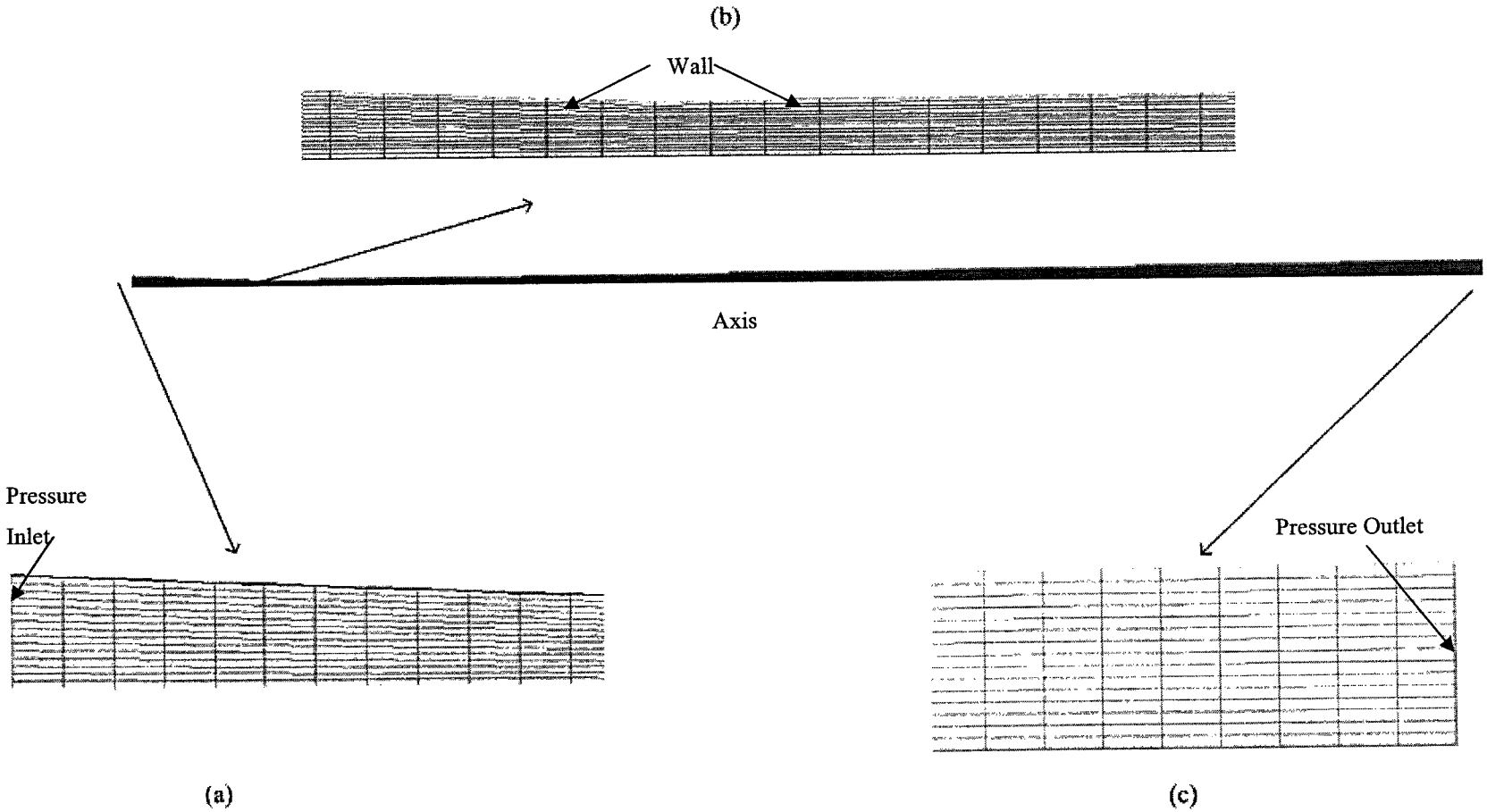

(b) Meshing for Second Design Iteration, width of control volume: 0.5 mm

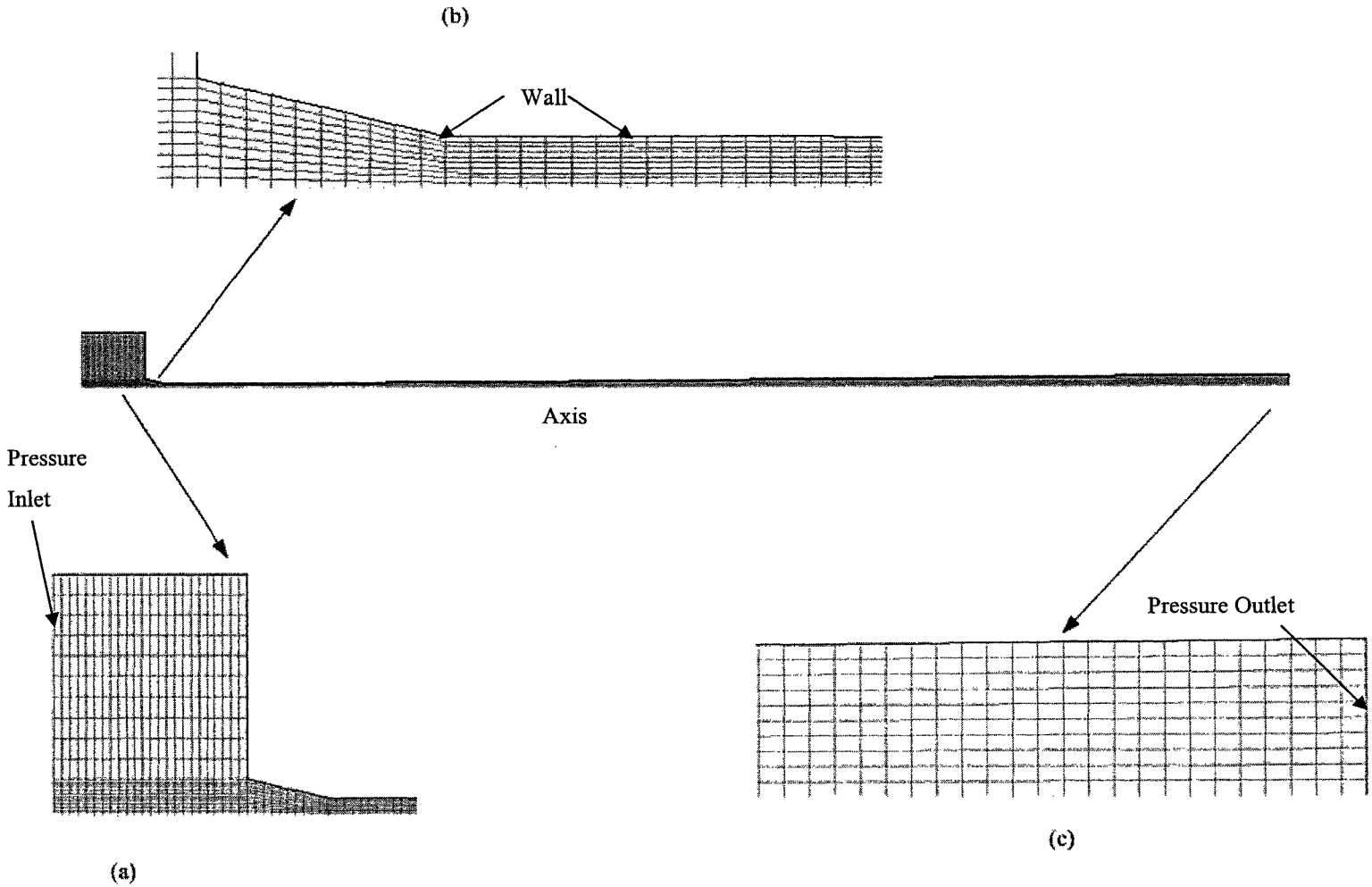

APPENDIX 2: One-dimensional Calculations for Converging-Diverging Nozzle

Known variables:

- Pressure at the exit of the nozzle, P=101 kPa
- Stagnation temperature: 293 K
- Diameter at the throat, ϕ_{throat}= 0.003 m
- Desired exit Mach number, M=3
- Driving gas: helium, k=5/3, ρ= 0.1785 kg/m^3, R=2077 J/kg*K

Using equations (3-12) and (3-12):

$$\frac{P_o}{P} = \left[1 + \frac{(\gamma - 1)}{2} M^2\right]^{\frac{\gamma}{\gamma - 1}}$$

and

$$\frac{A}{A^*} = \frac{1}{M}\left[\left(\frac{2}{\gamma + 1}\right) \cdot \left(1 + \left(\frac{\gamma - 1}{2}\right) M^2\right)\right]^{\frac{\gamma + 1}{2(\gamma - 1)}}$$

For an exit Mach number of 3, the area ratio is equal to: 2.33 which results in an exit diameter of 4.58 mm is required. To take into account the presence of a boundary layer, an exit diameter of 6 mm was chosen as the initial value for the CFD modeling.

Similarly, the stagnation pressure associated with the above pressure ratio is 3.23 MPa. As stated previously, lower values between 900 kPa and 2 MPa were chosen for the CFD modeling.

Using equation (3-15) and the helium constants,

$$\dot{m} = A^* \sqrt{\frac{\gamma}{R}\left(\frac{2}{\gamma - 1}\right)^{\frac{\gamma+1}{\gamma-1}}} \cdot \frac{P_o}{\sqrt{T_o}}$$

the mass flow rate of helium was also calculated and is approximately 0.000362 kg/s.